December 2019

Inflammation and Corrosion in Total Hip Prostheses: The Generation and Interaction of Reactive Oxygen Species with CoCrMo Metallic Biomaterial Surfaces

Michael John Wiegand
Clemson University, mjwiegan@gmail.com

INFLAMMATION AND CORROSION IN TOTAL HIP PROSTHESES: THE GENERATION AND INTERACTION OF REACTIVE OXYGEN SPECIES WITH CoCrMo METALLIC BIOMATERIAL SURFACES

A Dissertation
Presented to
the Graduate School of
Clemson University

In Partial Fulfillment
of the Requirements for the Degree
Doctor of Philosophy
Bioengineering

---

by
Michael John Wiegand
December 2019

Accepted by:
Dr. Jeremy L. Gilbert, Committee Chair
Dr. Melinda K. Harman
Dr. Martine LaBerge
Dr. Jeremy J. Mercuri

(This page is blank)

Abstract

There are many molecules, species and mechanisms that contribute to the overall wear and degradation of biometallic alloys like cobalt-chromium-molybdenum (CoCrMo). Following implantation, orthopaedic alloys are subject to an encompassing inflammatory response that will either lead to foreign body giant cell formation and attachment to the surface or the fibrous tissue encapsulation, forming an inflamed periprosthetic joint. In addition to the inflammatory response, tribocorrosion-based processes of alloy-on-alloy or alloy-on-polymer couples release polymeric wear debris, oxides, hydroxides, and metal ions in response to excessive wear, loading and corrosion. It is hypothesized that these processes, biological and triboelectrochemical, are linked together in a feedback-loop, and there is reason to believe that there exists a common catalyst, reactive oxygen species (ROS), that accelerates the cycle. This dissertation explains how ROS are generated in physiological conditions and how they affect electrochemical properties, under what circumstances ROS are consumed intracellularly, how different cell types respond to ROS-rich conditions, and how ROS interact with solution components native to synovial fluid, with a decisive effort and focus on defining their presence and role in the inflamed joint space.

By fluorescently labeling individual ROS like hydroxyl radicals ($OH\cdot$) and hydrogen peroxide (H_2O_2), we were able to correlate ROS concentrations against time of applied voltage (-1V vs. Ref) as well as against applied voltage for 2 hours. It was found that there exist thresholds for both the production and consumption of ROS, and there is a voltage range for which ROS are produced in measurable quantities. Under similar electrochemical conditions, different cell types (pre-osteoblast-like MC3T3-E1, monocyte macrophage-like U937) were cultured and exposed to an influx of ROS through cathodic excursions. It was found that cells possess a unique

‘electrochemical zone of viability’ per phenotype with reduced glutathione (GSH) activity, a ROS scavenger molecule produced within inflammatory cells, hypothesized to be the oxidative stress suppressor in the U937 cells. This hypothesis was later confirmed when exposing macrophages (RAW 264.7) to simulated synovial fluid, where it was found that ROS (H_2O_2) had a significant ($p < 0.05$) effect on intracellular GSH activity (fluorescent intensity). In addition to influencing cell behavior and response, ROS production and exposure was found to alter electrochemical properties of CoCrMo surfaces. Using nearfield electrochemical impedance spectroscopy (NEIS), CoCrMo retrievals and CoCrMo surfaces damaged by electrocautery and ROS-rich solutions were shown to have significantly ($p < 0.05$) decreased corrosion resistance (R_P) with increased constant phase element capacitance (CPE Q) and open circuit potentials (OCPs), indicating that ROS are major contributors in corrosion susceptibility.

By interpreting these observations and results, we were able to demonstrate that ROS are influential in several aspects of the inflammatory reaction to metallic biomaterials. The development of new diagnostics and predictive models centered around ROS can lead to safer practices involving orthopaedic alloys and further support our understanding of an inflamed joint space.

Dedication

I set out to obtain this degree because I wanted to continue my pursuit of knowledge in the broad scope of science, with a focus on orthopaedics. During this process, I became sick with testicular cancer, twice. The first time was a routine surgery with an extended recovery period, but the second time involved 12 weeks of chemotherapy with numerous hospitalizations, complications, and a recovery process that I'm still feeling and will feel long after I defend this thesis. It would have been easy for me to give up and move home to solely focus on my health. That being said, this thesis is for everyone that was there for me and wouldn't let me give up.

This thesis is for God and more than anyone, for my family. My parents, Kevin and Caroline, and my sister, Allison, were so supportive and I honestly wouldn't be here without their efforts. They continue to be my inspiration and motivation. My grandparents, uncles and aunts, cousins, and extended family have always supported me and have been eager for me to finish. They were there for me during my treatments and in the case of my grandfather, Richard Oden, have provided direct inspiration for studying the inflamed joint space. He received a double knee replacement when I was younger and became the underlying motivation for me to pursue this career. He will be so proud of the work I've accomplished.

This thesis is for my friends, roommates, especially Kiel, Pat, and Luke, and colleagues that encouraged me to be the best version of myself throughout the process. My friends visited me in Syracuse, New Hartford, and here in Charleston in sickness and health. I've had some that are genuinely interested in my research and even listened to presentations before (Max, Jon and Gwen), some that are invested in my technical reports (Mark and Marisa), and the rest that only want the bullet-points. I'd also like to thank Adam and Ghena who took it upon themselves to start a collection for me during my treatment. I couldn't imagine finishing this degree with the

added pressure of a mountain of hospital bills. I'm proud of the network I have built over the years and I hope they are proud of the work presented here. This thesis is also for my girlfriend Kim who has made the end of this process as enjoyable as possible. I'm so happy that I was able to finish this chapter of my life and begin a new one with her.

Finally, this thesis is for my care team, Dr. Theodore Gourdin, MD, and Dr. Elan Salzhauer, MD, and their respective staff. I can legitimately say that I wouldn't be here today without their efforts. From the beginning of my experience with cancer in upstate NY in Dr. Salzhauer's office to hopefully the end of it here in Charleston at the Hollings Cancer Center under Dr. Gourdin's care, this thesis is for all your hard work, research and efforts in restoring my quality of life. I owe these physicians my life and can never thank them enough for what they did, so I hope this thesis will suffice for now.

All of the people listed and countless others are forever part of me and my journey, and they have defined me over the years. This thesis is for them, my Besties for Testes.

Acknowledgments

This degree is a long-time coming, so I have a lot of people to thank and acknowledge. The first and foremost person I would like to acknowledge is my advisor, Dr. Jeremy L. Gilbert. I initially came to him for an independent study to complete my required credits, which turned into a peer-reviewed manuscript, which turned into me full-on joining his lab and moving from Syracuse, NY to Charleston, SC. He has spent an incredible amount of time mentoring me in my research, writing and presentation skills, and he is the foundation behind my expertise in the fields of bioengineering, corrosion and materials science. I can attribute my knowledge in these areas going forward to what I learned in his lab. I would also like to acknowledge his incredible handling of last summer where he didn't have any expectations for my research, he just wanted me to be healthy. He helped make this process as stress-free as possible.

The other two research mentors I would like to acknowledge are my former advisor whom I completed my Master's under, Dr. Julie M. Hasenwinkel, and my supervisor at Bristol-Myers Squibb, Dr. Terrance W. Carone, II. I began my research at Syracuse University under Julie, and she taught me probably the most important lesson that I will always remember, "If we knew exactly what we were doing, it wouldn't be called research." She taught me how to conduct research in an academic setting, as well as gave me the opportunity to teach students as part of my teaching assistantship. Terrance (TW) hired me for a summer internship at BMS in Syracuse, NY, which was my first real lab experience. This internship opened up so many doors for me but most importantly, I hadn't considered pursuing a graduate degree until we discussed my future. TW advised that I advance my learning past my undergraduate degree if I wanted to be even more successful in industry or academia, and for that, I thank him because I wouldn't be in this position today without him. Interestingly enough, I didn't realize the complicated web of

research lineage I would embark on by working for Dr. Hasenwinkel (TW's PhD advisor) and eventually Dr. Gilbert (Julie's PhD advisor, TW's lab-technician supervisor).

From Clemson University and the Medical University of South Carolina, I would like to thank my committee members Dr. Martine LaBerge, Dr. Jeremy J. Mercuri and Dr. Melinda K. Harman. Their comments and advice during my candidacy exam helped shape the completion of my dissertation, and I believe that I have a much stronger understanding of the degree process as well as the scope of my research. I would also like to thank Dr. Ann Foley, Tommy Gallien, Cameron Hay, Maria Torres, and Leigh Humphries. Dr. Foley has been very helpful with advising my cell-culture work in addition to odds and ends navigating the Clemson-MUSC bridge. Cameron has been a phenomenal addition to the Bioengineering Department and has made the end of the graduate process run as smoothly as possible for me. The faculty and staff members at Clemson and MUSC were integral in the degree process, reserving rooms, submission of orders and making sure that I completed all necessary forms. Also, Leigh, Maria and Tommy went above and beyond last summer by being there for me during my treatments and making sure I didn't skip a beat. I would also like to acknowledge Thomas Benton for assisting me in the synthesis of one of my fluorescent dosimeters, and for providing input into a publication he became a part of.

From Syracuse University, I would like to thank Lynore de la Rosa and my undergraduate mentees, Kennedy Faraci and Brittany Reed. Lynore helped me with so much and was always there to talk me through and assist in the graduate process. Mentoring Kennedy and Brittany really helped me understand how to translate my research in an effective way, and it's added bonuses that they became some of my closest friends at Syracuse, were so much fun to work with, and have a published manuscript with Dr. Hasenwinkel and myself. I would also like

to thank my colleagues, Dr. Patricia Wardwell, Dr. Allen Osaheni, and Srihari Prasad. Tricia was there with me from the very beginning of my Syracuse days and was instrumental in helping me navigate the graduate life as well as teaching me how to culture cells. Allen and Sri were my roommates for over three years and made the degree process a little easier because they were going through the same things in their respective programs.

From the Gilbert Lab Group, I would like to acknowledge and thank Dr. David Pierre, Dr. Greg Kubacki, Dr. Piyush Khullar, Dr. Eric Ouellette, Aarti Shenoy, and Dongkai Zhu. Not only do I consider all of these people my friends, but all have helped me through my research by assisting or training me in some various aspect relating to bioengineering, corrosion and materials science. David was there for me in and outside the lab, and I owe much of my formal training to Greg and am thankful for all the time all of us shared together at Syracuse and Clemson. I would also like to acknowledge the help and support of my Clemson research undergraduate student from last summer, Sara Littlejohn. I wish I got to interact with her more because she proved to be a very helpful asset to me during a very tough time.

Finally, I would like to acknowledge the funding sources that have supported me over my graduate degree process including the Syracuse University Graduate Research Fellowship, Syracuse University Teaching Assistantship, Clemson University Graduate Assistantship, DePuy Synthes and Bausch and Lomb.

Table of Contents

List of Tables

List of Figures

List of Abbreviations

2-hydroxyterephthalate	HTA
316L stainless steel	316LSS
Adverse local tissue reaction	ALTR
Albumin	A
Alternating current	AC
Analysis of Variance	ANOVA
Bovine serum albumin	BSA
Breakdown potential	E_{BREAK}
Chlorided-silver reference	Ag/AgCl
Chromium(III),(VI)	$Cr^{3+,6+}$
Cobalt(II)	Co^{2+}
Cobalt-chromium-molybdenum	CoCrMo
Constant phase element capacitance	Q
Constant phase element exponent	α
Corrosion current	i_{CORR}
Corrosion potential	E_{CORR}
Corrosion resistance	R_P
Current	i
Deionized water	DI
Design of experiment	DoE
Direct current	DC
Electrochemical impedance spectroscopy	EIS
Emission wavelength	λ_{em}
Ethanol	EtOH
Excitation wavelength	λ_{ex}
Fetal bovine serum	FBS
Final fluorescent intensity	I
Foreign body giant cell	FBGC
Global surface	GS
Globulin	G
Hyaluronic acid	HA
Hydrochloric acid	HCL
Hydrogen peroxide	H_2O_2
Hydroxyl radical	$OH\cdot$
Impact range	Δ
Impedance magnitude	|Z|
Inflammatory cell induced corrosion	ICIC
Initial fluorescent intensity	I_O
Iron(II),(III)	$Fe^{2+,3+}$
Lecithin	PL
Mechanically assisted crevice corrosion	MACC
Metal-on-metal	MoM
Metal-on-polymer	MoP
Metal-organic framework	MOF

Monocyte macrophage-like cells	U937
Mouse macrophage cells	RAW 264.7
NADPH oxidase	NOX
Nearfield electrochemical impedance spectroscopy	NEIS
Nicotinamide adenine dinucleotide phosphate	NADPH
Nitric oxide	NO
Open circuit potential	OCP
Oxidized glutathione	GSSG
Passivating current	i_{PASS}
Pentafluorobenzenesulfonyl-fluorescein	PFF
Phase angle	θ
Phorbol 12-myristate 13-acetate	PMA
Phosphate buffered saline	PBS
Potential	E
Pre-osteoblast-like cells	MC3T3-E1
Reactive chemical species	RCS
Reactive nitrogen species	RNS
Reactive oxygen intermediates	ROI
Reactive oxygen species	ROS
Reduced glutathione	GSH
Relative Goldberg	Rel. GB
Scanning electron microscopy	SEM
Signal-to-noise	S/N
Sodium chloride	NaCl
Solution resistance	R_S
Standard deviation	SD
Superoxide anion	$O_2^{-\cdot}$
Terephthalic acid	TA
Titanium, 6-aluminum, 4-vanadium	Ti6Al4V
Total hip arthroplasty	THA
Total joint replacement	TJR
Total knee arthroplasty	TKA

1. Background

1.1. Purpose

Orthopaedic alloys were implemented in the 19th century[1] for the sole purpose of restoring the quality of life in a patient suffering from pain due to the degradation of the joint. These alloys were initially designed for permanent load-bearing applications such as total hip and knee arthroplasties (THA, TKA), however since their initial design and development, they have been tailored for a variety of temporary purposes such as bone plates, cardiovascular stents, dental procedures, pedicle screws and rods[1] with corrosion-resistant superalloys as the standard[2]. The continued use of these long-ago developed alloys would lead us to believe that there are no serious adverse reactions or side-effects to having a foreign material in the human body, yet the failure and degradation of the alloys[3] are becoming more and more prevalent with the increasing average age of the population[4], as well as patients outliving the life-cycle of the product. The clinical success of an implant is directly related to the associated biological response, ranging from inert to rejected (failure)[5]. One of the most common orthopaedic failure modes, infection (2% of all primary TKAs as of 2012)[6], is not completely the fault of the alloy performance with healthy patients subject to airborne pathogens or operating room human error (27.4% of 781 revisions)[7]. By contrast, the most common forms of revision are attributed to the performance of the alloy: aseptic loosening (39.9% of 781 revisions), instability (7.5%...) and periprosthetic fracture (4.7%...)[7]. The main contributors behind the failure of orthopaedic alloys in an inflamed joint space are electrochemical dissolution phenomena, wear and/or the surrounding dynamic synovial environment[8].

The purpose of this research is to determine the synergistic role between this inflamed joint space and one of its most relevant and harmful constituents, reactive oxygen species (ROS).

1.2. Inflammation

Inflammation is a natural physiological occurrence designed to initiate, maintain and heal afflicted tissue[9]. In response to tissue injury, disruption of the blood vessels and extravasation of blood constituents[10], the body responds by using a systematic approach to restore homeostasis where the surrounding environment undergoes acute inflammation/recruitment to tissues, followed by proliferation/differentiation and activation *in situ*, conversion of suppressive cells and then remodeling/homeostasis restoration[11]. When a medical device is implanted invasively like that of total arthroplasties, the site will often transition from acute to chronic inflammation over a period of weeks through the assistance of mast cells, lymphocytes and cytokines[12]. The body will continue to attack the implant by recruiting phagocytic cells like monocytes and infiltrating neutrophils that eventually mature into macrophages and form into foreign body giant cells (FBGCs), which will attack the surface, engulf wear particles and metal ions, leading to cytotoxic, genotoxic, and osteolytic effects within the periprosthetic joint[12]. Inflammation of the joint space surrounding metallic total joint implants remains a significant cause for revision and replacement with the inflammatory response often attributed to further damage of both tissue and implant, however inflammation can be initiated from multiple sources.

1.3. Lymphocytic Response vs. Wear-Induced Inflammation

There exists much debate within the orthopaedic community surrounding the true root of chronic inflammation surrounding a metallic biomaterial device. Is the prolonged inflammatory response due to the host recognizing a foreign material and naturally progressing into a lymphocyte-lead defense OR is there a wear particle- and/or debris-induced reaction triggering this long-term effect? On one side of the argument is the foreign body reaction, composed of macrophages and other inflammatory molecules in response to biomaterials[12]. The host site

undergoes a methodical approach to the invasive device: “injury, blood-material interactions, provisional matrix formation, acute inflammation, chronic inflammation, granulation tissue development, foreign body reaction, and fibrosis/fibrous capsule development”[12]. Fibrous pseudocapsule formation around a hip implant has been theorized to release inflammatory mediators, with ROS as causative factors in tissue fibrosis, osteolysis and bone resorption[13]. The morphological progression of FBGCs to fibrous pseudocapsule formation is hypothesized to lead to stress-concentrated zones, eventually leading to failure of the device through continuous degradation and reduction of mechanical properties[12]. Inflammatory cell-induced (ICI) corrosion of the surface[14, 15] initiates the generation and consequent release of ROS and lymphocytic cytokines (interleukin (IL)-1β)[16], promoting osteoclast differentiation and the formation of a fibrous membrane around the implant[13, 17]. Once bio-corrosion of the alloy surface is initiated[3], topography of the surface is altered where particles are released and osteoclast-derived surface pits develop[18], introducing surface roughness as another factor relating to cell response (cytokine release) and attack (metal ion dissolution). Macrophages cultured on microrough surfaces have been shown to increase the secretion of anti-inflammatory cytokine (IL-10) and pro-inflammatory cytokines (TNF-α, IL-6 and IP-10) when compared to smooth surfaces[19]. The surrounding biology becomes increasingly concentrated with organic and inorganic material, leading to drastic changes in solution chemistry. It has been reported that CoCrMo alloy surfaces exposed to electrolytic simulated biological solutions (NaCl, KH_2PO_4, $CaCl_2$, KCl, $MgCl_2$, $NaHCO_3$, Na_2SO_4) release Co from the surface due to oxidizing conditions leading to transpassive dissolution, similar to the effects seen during activation repassivation cycles from cyclic potential variation[20]. This eventually promotes agitation of the inflammatory cells, which begins the process over again (*feedback-loop hypothesis*).

The other side of the argument is that the response is dominated and controlled by the presence of the metal alloy, specifically metal alloy that is released from continuous use and wear. The main hypothesis is that the prolonged inflammatory response is activated as a result of micron-sized metallic/polymeric particles released from articulating surfaces[21]. Particles are then engulfed (phagocytized) by inflammatory-cells[22] which increases inflammatory and osteolytic stress response-factors like high mobility group protein-B1 (HMGB1), cyclooxygenase-2 (COX2), inducible nitric oxide synthase (iNOS), 4-hydroxynonenal (4-HNE) and nitrotyrosine (NT), supporting oxidative stress-induced bone resorption and aseptic loosening of total hip replacements[23, 24]. Metal ion (M^X) exposure within the joint space has been extensively characterized with focus on cellular uptake and resulting chromosome aberrations and aneugenicity[25], and other genotoxicity related events due to interactions and formation of ROS including hydroxyl radical (OH·) and hydrogen peroxide (H_2O_2) (Eqn. 1-3)[24, 26, 27].

$$M(X) + O_2^{\bullet -} \rightarrow M(X-1) + O_2 \quad [1]$$

$$2O_2^{\bullet -} + 2H^+ \rightarrow H_2O_2 + O_2 \quad [2]$$

$$M(X-1) + H_2O_2 \rightarrow M(X) + OH^{\bullet} + OH^- \quad [3]$$

Transition metal ions, notably chromium (Cr^{3+}, Cr^{6+}) and cobalt (Co^{2+}), have been shown to knock-down or induce antioxidant enzyme transcription and translation factors, affecting the overall mitigation of ROS[28] while subsequently oxidizing cytoplasm proteins[29]. Tantalum (Ta, regarded as inert) and commercially pure titanium (CpTi) in addition to cobalt and chromium ions have also been shown to have a direct dose-dependent response with concentrations correlated to amounts of oxidative tissue damage[24, 26]. In contrast, it has been reported that metal ions have a limited capacity to activate macrophages compared to polyethylene (PE) particles,

even though metal ions are produced ~13,500 times (count, not volume) more than PE particles[30]. With regards to formation of metal-organic frameworks (MOFs), these ions will directly bind to metallo- and non-metalloproteins which leads to a loss of biological function, tissue damage, necrosis and inflammation[24, 26].

Furthermore, there even appears to be size-dependent differences in cell morphology and damage mechanism after exposure to either nano- or micron-sized particles. Nanoparticles as a result of hard articulating surfaces were found to cluster within vacuoles in the cell cytoplasm whereas microparticles (primarily from wear of the softer surfaces) were found to surround the nucleus in fibroblasts[21]. The nanoparticles caused more mitochondrial and DNA damage in the short-term than the microparticles due to their fast dissolving rate within the vacuoles, however the extended release of metal into the nucleus and cytoplasm from the larger microparticles resulted in a more complex and longer-lasting damage mode[21]. These results would suggest that there are two wear-induced damage mechanisms with short-term inflammation triggered by metal-on-metal (MoM) micromotion and long-term inflammation sustained from the larger particulate debris from metal-on-polymer (MoP) coupled interfaces. This duel mechanism further supports the sustained wear-induced reactions that trigger a complementary inflammatory response (*feedback-loop hypothesis*) (Figure 1).

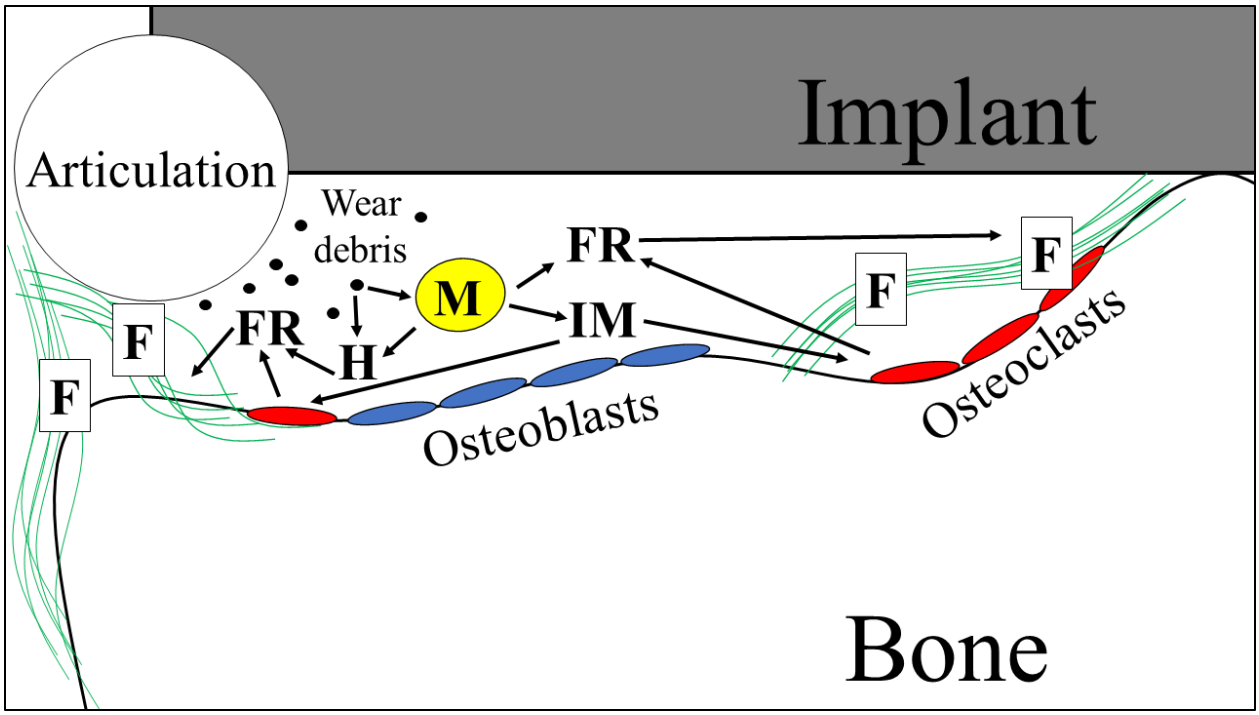

Figure 1: Schematic illustrating ROS and free radical (FR) generation, leading to inflammatory markers (IM), macrophage (M), osteoclast (OC) and histiocyte (H) activation and stimulation, with the eventual progress of osteolysis and periprosthetic fibrosis (F) [Adapted from Kinov. et al.][13]

Comparing both sides of the argument, there is no long-term solution to avoid these interactions within the host. Natural polymers, engineered cytokines and smart materials are being developed to manipulate macrophage phenotype (M1, M2) as well as pro- and anti-inflammatory responses[31], however there are certain applications like load-bearing devices that will for the time being, require a hard metal component. And while it appears that metal ions and debris are at the center of periprosthetic inflammation, there is a class of molecules that are more biologically relevant, destructive and present in the absence of metal.

1.4. Reactive Oxygen Species (ROS)

Reactive oxygen species (ROS), major players in inflammation, are a source of oxidative stress that can harm key cellular components and functions. ROS are a class of oxygen-centered reactive molecules that are continuously generated and consumed within all aerobic organisms,

predominantly as a result of normal/healthy metabolic activity via the dysregulation of the mitochondrial membrane[32, 33]. ROS is also central to the respiratory burst process associated with mononuclear phagocytic derived cells, where NOX catalysts in the cell membrane and phagosomes use NADP/NADPH oxidation to convert oxygen into ROS as the main mechanism to fight infection and foreign bodies[34-39]. ROS can also be formed electrochemically as byproducts of reduction reactions involving water and oxygen molecules[40]. There has been a significant push in recent years to determine the role of ROS in the inflammatory response within the human body[36, 37] leading to tissue degradation, aseptic loosening, and ultimately rejection of metallic implants[23, 41].

To briefly describe the generation of ROS through mechanical and electrochemical processes (Appendix A.1), the passive oxide film formed on metallic implant surfaces is abraded during mechanically assisted crevice corrosion (MACC), leading to a potential drop up to -1000 mV vs. SCE in phosphate buffered saline (PBS)[42] and up to -1500 mV vs. SCE in buffered solutions containing fetal calf serum[43]. This MACC-induced cathodic surface effect increases the surface electron density and has a resulting lethal effect on adhered cells[44-46]. The excess surface electrons are free to take part in reduction reactions at the surface where water and oxygen molecules are reduced as such[47]:

$$O_2 + H_2O + e^- \rightarrow HO_2^{\cdot} + OH^- \quad [4]$$

$$HO_2^{\cdot} + H_2O + e^- \rightarrow H_2O_2 + OH^{\cdot} \quad [5]$$

$$OH^{\cdot} + e^- \rightarrow OH^- \quad [6]$$

$$H_2O_2 + e^- \rightarrow OH^{\cdot} + OH^- \quad [7]$$

$$OH^{\cdot} + e^- \rightarrow OH^- \quad [8]$$

ROS produced at the surface then contribute to measurable adverse effects on material properties. Hydrogen peroxide (H_2O_2) has been shown to increase charge transfer and oxide film thickness while decreasing oxide resistance on commercially pure titanium (CpTi) and titanium, 6-aluminum, 4-vanadium (Ti6Al4V) surfaces[48]. 316L stainless steel (316LSS) submersed in H_2O_2-rich solutions displayed a significantly altered corrosion process, with aggressive localized corrosion by ways of increased metal ion release and decreased polarization resistance (R_P)[49]. Simulated inflammatory (SI) conditions containing H_2O_2 and ferrous ions (Fe^{3+}) have been shown to raise both the oxidizing power and open circuit potential (OCP) of CoCrMo alloy with smaller fretting current densities, indicating a less protective oxide film[50]. H_2O_2 increases titanium (Ti) release from the surface of Ti6Al4V in cell culture growth media than media alone[51], and the presence of physiologically-relevant levels of macrophage secreted H_2O_2, oxide ion (O_2^-) and nitric oxide (NO) has been shown to enhance film properties by increasing total metal oxides through oxidation and nitration reactions[52, 53]:

$$O_2 + NO \rightarrow NO_3^- \quad [9]$$

$$M + NO_3^- \rightarrow MO + NO_2^- \quad [10]$$

In addition to altering surface and material properties, high intracellular concentrations of reactive oxygen intermediates (ROIs) and ROS lead to potent levels of oxidative stress[54]. When intracellular oxidative stress surpasses the cell's natural antioxidant enzymatic capacity, key cellular components like the membrane structural integrity are damaged or oxidized (lipids, proteins, nucleic acids, etc.)[55], leading to a cascade of cell death[56]. Kalbacova et al. found that cathodic polarization of Ti6Al4V increases intracellular (monocyte/macrophages, osteoblasts) ROS levels and decreases metabolic activity, in agreement with a cellular response study to simulated extracellular solution H_2O_2[47]. While increasing ROS concentrations are concerning

enough to the surrounding tissue, the other side of the molar balance, being decreasing oxygen concentration, is equally problematic. The surrounding environment deaerates and becomes hypoxic which has been shown to affect cell spreading[40] in addition to collagen synthesis and alkaline phosphatase (AP) activity, both of which are associated with the bone remodeling process[57].

Efforts have been made to combat toxic intracellular ROS build-up using scavengers and reducing agents[54]. Yet similar to the decrease in oxygen paradigm, there usually exists a negative reaction. Naturally occurring molecules like melanin prevent the degradation of relatively low-toxic ROS molecules (H_2O_2) into the highly-toxic radicals (hydroxyl radical), yet when melanin reduces solution ferric ions into ferrous ions, a different set of reactions (Fenton Reactions, Eqn. 12-13) ultimately creates more radicals and more ferric ions[27, 58, 59].

$$Fe(III) + O_2^{\bullet -} \rightarrow Fe(II) + O_2 \quad [11]$$

$$Fe(II) + H_2O_2 \rightarrow Fe(III) + OH^{\bullet} + OH^{-} \quad [12]$$

While novel ROS scavenging molecules provide a therapeutic effect to the local tissue, the cell contains a native ROS scavenging molecule that is produced as both a combatant to oxidative stress, and functions as a cell-signaling molecule in redox propagation.

1.5. Reduced Glutathione (GSH)

Reduced glutathione (GSH) is an endogenous antioxidant that suppresses redox reactions and maintains cellular homeostasis[60]. GSH protects cells from lipid peroxidation and DNA/RNA fragmentation[61]. Cellular glutathione redox homeostasis is achieved through oxidation of GSH or GSH transport during the apoptotic cascade[62], where GSH activity is often correlated to oxidative stress. When glutathione thiol production is suppressed or inhibited and intracellular

ROS concentrations increase, the mode of death switches from apoptosis to necrosis[63]. Researchers have used GSH detection in cases of revision where low ratios of reduced glutathione (GSH) to oxidized glutathione (GSSG) and high levels of malondialdehyde (MDA) indicate high concentrations of oxidative stress[13]. Alternatively, hypoxic apoptotic cells (U937 HX) have been shown to retain GSH rather than extrude (apoptotic U937) the metabolite following programmed cell death[64], indicating that mode of cell death contributes to solution chemistry and that retrieved solution GSH content isn't a definitive measure of oxidative stress.

Clinically relevant metal ions, such as 1 μM of Cr^{6+}, can decrease macrophage glutathione levels and viability via oxidation to its dimer GSSG, leading to the production of ROS and signal transduction of the apoptotic pathway and extracellular transport of redox- and GSH-catabolites[20, 65, 66]. GSH is vital to the mitigation of ROS build-up, however it cannot be relied upon solely to suppress ROS both intracellularly and extracellularly.

1.6. Motivation

From this chapter, we have explained how ROS can be produced from cellular metabolic and anaerobic activity, respiratory burst mechanisms, as well as through electrochemical reduction reactions by the transfer of mobile metal electrode surface electrons, thereby inducing chemical changes to local oxygenated molecules[40]. It's accepted that ROS, ROI, reactive chemical species (RCS) and reactive nitrogen species (RNS) initiate the cascade of cell signaling during oxidative-stress induced inflammation[67], however the acceptance of ROS as inflammatory signaling molecules through quantification is currently difficult due to detection methods, pathway identification, and upregulation[68]. ROS integrated production rates and steady-state concentrations remain mostly a mystery *in situ* due to their creation from multiple sources[69]. Several groups and studies have characterized the cytotoxic, genotoxic, and material degradation

due to ROS, and our study is motivated by assembling all this information into one holistic periprosthetic joint model that can better predict and understand inflammation in the joint environment.

There are many additional sources of motivation to complete this work, but none are more relevant to the field and our research than the growing population that are outliving the lifetimes of implanted devices, in addition to those that will need revision or replacement due to the damaging effects of ROS such as aseptic loosening. Aseptic loosening (absence of infection)[70] is primarily caused by wear debris-initiated chronic inflammation, a pre-cursor to inflammatory-mediated bone resorption[70]. Aseptic loosening of total joint replacement (TJR) implants is one of the leading causes in TJR revision surgeries, where 10-20% of all TJR surgeries need additional procedures. It is estimated[23] that the annual number of TJR surgeries worldwide will exceed 4,000,000 by the year 2030.

In terms of the near future, there is little that can be done to completely halt the inflammatory response and it is feasible to imagine that far into the future, there might be a class of smarter biomaterials that mitigate and eliminate chronic inflammation. In the present however, we possess techniques and capabilities that will help us define the inflammatory response to current biomaterials in terms of molecules produced and consumed, specifically ROS.

2. Hypotheses, Goals and Specific Aims

2.1. Hypotheses

The main theme of this research is located within the proposed positive *feedback-loop* mechanism that our lab has been defining as of recent. One side of the feedback-loop cycle is that the initial inflammatory reaction to a medical device drives corrosion through a chronic inflammatory response that contributes to the degradation and ultimate failure of the implant via metal ion dissolution and wear. The other side of the cycle is the medical device is subjected to harsh chemicals and wear *in situ*, thus releasing debris and particles which sustains the inflammatory response lead by FBGC attack of the surface, tissue encapsulation, pressure build-up, dislocation, etc. The hypothesis of this work isn't focused on which process precedes the other; however, it is fixated on defining what role ROS play within the feedback-loop mechanism. We hypothesize that ROS are produced from both the surrounding biology and electrochemically-based material interactions, both of which contribute to the overall inflammatory response and destruction of the metal surface. Cyclic motion of articulating metal surfaces leads to cathodic voltages and debris generation (+ROS), and stimulation of inflammatory cells using debris yields a reactive response (+ROS). Increased ROS production then compromises the corrosion resistance of CoCrMo alloys, increasing the release of metal ions and degrading the passivating properties of the oxide film on their surfaces. Therefore, our hypothesized feedback between ROS generation and metal degradation processes will allow us to create sophisticated predictive models based on the conditions present at the fluid-cell-metal interface.

2.2. Goals

ROS can be produced both physiologically and chemically in the joint space surrounding a metallic implant, thus the major critical gap in knowledge is what oxidative source (intra- or extracellular) is responsible for cell death, tissue degeneration and/or metallic implant corrosion? Does secreted cellular-ROS lead to an increase in catalytic activity involving H_2O_2 at the surface, thus changing electrochemical behavior OR do reduction reaction byproducts permeate cell membranes and begin the apoptotic signaling pathway, releasing ROS metabolites and further decreasing the corrosion resistance of the implant?

The major goal of this research is to define this feedback mechanism between biochemical species and metallic biomaterials in an electrochemical system. We investigated individual components of the system in order to understand this inflammatory-corrosive interaction. This is significant to the field of orthopaedic implants because it has advanced our understanding of ROS generation in the joint space and may, in the long term, lead to smarter biomedical alloys and dynamic implant coatings that have greater corrosion resistance and a decreased immune response. This would ultimately lead to more predictable implant lifetimes with an increase is efficiency and safety.

A *major obstacle* in our field of biomaterial corrosion and failure is the lack of clear understanding of the inflammatory joint fluid-based environment during corrosion, making it difficult to predict metallic surface response to changing physiological conditions. Another obstacle is accurately detecting and quantifying local ROS concentrations due to their high rates of reactivity and short half-lives. This obstacle, in addition to ROS generated from multiple sources, creates uncertainty in ROS concentrations within the inflamed joint space as well as what source contributes the most to prolonged inflammation. Our *long-term goal* is to understand

the extent of ROS generated in inflamed joints with implants, specific types and amounts of ROS and how they participate in metallic corrosion behavior. To begin this process, we have developed protocols and detection methods for individual ROS and inflammatory molecules in the presence of cobalt-chromium-molybdenum (CoCrMo) alloy with the eventual intended use for retrieved human joint fluid analysis. Characterization of these species with respect to electrochemical behavior of the alloy, cell viability and corrosion mechanisms support our *feedback-loop hypothesis* that ROS in joint fluid enhances corrosion of CoCrMo which boosts ROS generation. Our models and testing have advanced our current understanding of the interplay between ROS, biology and corrosion with respect to attack of metallic surfaces.

2.3. Specific Aims

The specific aims listed below were investigated in order to address the link between ROS and the inflammatory environment surrounding the joint space of total prostheses. Each aim is made up of both novel methodology and experimental conditions to satisfy the research goals.

Aim 1. Develop procedures for detecting ROS near a metallic implant surface.

Fluorescent probes offer an opportunity to tag ROS produced in solution near an implant surface in real-time. We *hypothesized* that we can detect individual ROS produced from reduction reactions at a metal surface using fluorescent tagging methods. Predictive models were developed to correlate ROS concentrations at applied voltages corresponding to corrosive conditions. We also explored how these ROS molecules directly affect the electrochemical behavior of CoCrMo implants. These models and methods will help determine clinically-relevant levels of ROS near an implant surface, which will be further used in cell culture experiments to more accurately represent the inflamed joint space biological response.

Aim 2. Classify cellular responses to simulated corrosive and inflammatory conditions.

Recent reports have shown evidence of inflammatory cell induced (ICI) corrosion on metallic implants. We *hypothesized* that cell behavior, structure and viability on CoCrMo surfaces would be affected by inflammatory-like conditions and oxidation. Different cell types cultured on metallic alloys during corrosion-like conditions will help identify pathways that lead to or contribute to inflammatory responses as well as programmed cell death. We also examined a set of synthetic joint fluid formulations (Aim 4) exposed to polished CoCrMo discs as well as macrophage cultures in order to determine which factors present in the joint capsule contribute most to this inflammatory response.

Aim 3. Use electrochemical impedance spectroscopy to assess localized surface integrity impacted by ROS.

Electrochemical impedance spectroscopy (EIS) can be used to evaluate the state of a metallic surface after wear and corrosion. We *hypothesized* that different ROS-influenced inflammatory and corrosive conditions produce unique EIS responses, influencing both global and local oxide film and surface properties. By correlating corrosion type and failure modes with specific electrochemical spectra, we can increase our understanding of how the implant surface changes electrochemically with environmental factors.

Aim 4. Define solution and material properties in response to multiple native synovial fluid components in a modified factorial array

There exist several constituents within synovial fluid that influence solution-cell-material behavior during normal, inflamed, osteolytic and infectious states of the periprosthetic joint environment. We *hypothesized* that multivariable interactions could be isolated and characterized using a Taguchi orthogonal array. Determining which factors dominate corrosion resistance and

cell viability in a dynamic environment could lead to more advanced and comprehensive *in vitro* models with increased long-term prediction accuracy.

2.4. Significance

A majority of the research dedicated to this subset field of metallic implant-cell interactions has investigated phagocytosis of wear particles, the role of wear debris-initiated activation of ROS within local inflammatory cells, and oxidation of intracellular proteins and lipids by ROS[21, 29, 54]. Recently, there have been reports of ICI corrosion on retrieved CoCrMo implant surfaces believed to be a direct response to inflammatory cell-activated ROS regulation[14, 15, 71], but these results are inconclusive and could be a result of electrocautery methods[72]. Simulated inflammatory solutions containing ROS such as H_2O_2, HCl and ferrous ions ($Fe^{2+,3+}$) significantly affect corrosion susceptibility of CoCrMo[50], Ti6Al4V and SS316 surfaces[49] by decreasing the oxide film passivity and increasing the surface potential and current density. *In vitro* corrosion rates of CoCrMo[14] and Ti6Al4V[48] also increase in the presence of H_2O_2, hydrochloric acid (HCl) and Ca^{2+} ions[51]. These studies suggest that corrosion and implant susceptibility are affected by ROS, however the source of the ROS is not well defined or accepted.

We believe that the research presented here will give new perspectives to the state of biometallic surfaces subjected to physiological conditions, and that there isn't always one cause behind inflammation or corrosion. Accurate ROS identification will not only be able to reveal what has previously happened to the implant, but perhaps also foreshadow what is to come with respect to the inflammatory reaction and degradation of the implant.

3. Research Outline

3.1. Chapter Backgrounds and Citations

This section will briefly describe how each chapter relates to the overarching goal of defining the role of reactive oxygen species within an inflamed joint environment. Rather than organizing by specific aim, the research chapters will briefly describe the motivation, primary goals and hypotheses of each. All of these research chapters have been accepted or submitted for publication, with Chapter 4 and 5 accepted and in-press. All work was completed at the Clemson University-Medical University of South Carolina Joint Program at the Medical University of South Carolina in Charleston, SC or the Syracuse Biomaterials Institute at Syracuse University in Syracuse, NY.

4. A fluorescent approach for detecting and measuring reduction reaction byproducts near cathodically-biased metallic surfaces: Reactive oxygen species production and quantification

There are several different ROS molecules produced at the surface during reduction reactions. Water and oxygen molecules are reduced by excess surface electrons when the surface potential drops, generating ROS and reactive oxygen intermediates (ROI)[40]. Common ROS include singlet oxygen ($^1O_2$), superoxide anion ($O_2^{-}\cdot$), hydrogen peroxide (H_2O_2) and hydroxyl radicals ($OH\cdot$)[73]. The two most commonly used ROS fluorescent dosimeters are 2',7'-dichlorodihydrofluorescein (DCFH)[33] and Amplex Red[59], with wide acceptance of their use in the biomedical community. However, it has recently been reported that these di-hydro compounds are highly photosensitive and autoxidize, generating large background fluorescence. These molecules do not differentiate between ROS molecules, and thus lack selectivity[73].

Terephthalic acid (TA) is an organic aromatic compound that selectively binds to OH· over other ROS, yielding 2-hydroxyterepthalate (HTA), a stable fluorescent compound[74]. Pentafluorobenzenesulfonyl-fluorescein (PFF), a non-fluorescent ROS selective molecule, is cleaved at the sulfonate linkage in the presence of H_2O_2, leaving the highly fluorescent fluorescein molecule[75]. This chapter focuses on the development and methods used to capture individual ROS concentrations at the surface of metallic biomaterials in conditions associated with corrosion and inflammation using the fluorescent dosimeters TA and PFF. Correlating individual ROS production near a cathodically-charged biomedical alloy will help answer how surface chemistry affects ROS conversion. This work was published in the journal Bioelectrochemistry with the following citation:

Wiegand, MJ, Benton, TZ, Gilbert, JL. 2019. A fluorescent approach for detecting and measuring reduction reaction byproducts near cathodically-biased metallic surfaces: Reactive oxygen species production and quantification. *Bioelectrochemistry* 2019: 129: 235-241.

5. *Electrochemical potential zone of viability on CoCrMo surfaces is affected by cell type: Macrophages under cathodic bias are more resistant to killing*

As we've learned from an electrochemically-biased implant surface, several types of ROS are introduced to the local environment with other reaction byproducts including metal ions, debris, oxides, and excess surface electrons known to be present as well[14]. Each of these may play a role in initiating the immune response and subsequent recruitment of inflammatory cells to the adjacent tissue and joint space surrounding a metallic implant. The infiltrating inflammatory cells prompt a series of defense mechanisms that include production and secretion of ROS and ROS-scavenging molecules near and on implant surfaces[17].

Electrochemical stimuli at the cell-metal interface have been shown to influence cell viability and behavior. Abrading the oxide film at the surface can decrease the potential to -1V (vs. Ref) while the addition of inflammatory species like hypochlorous acid and hydrogen peroxide can shift the surface potential upwards of +650 mV (vs. Ref)[49, 50] with potential shifts of this magnitude dramatically reducing cell viability[45]. This chapter focuses on observing cell viability in response to various electrochemical conditions linked to corrosion and inflammation. By determining how different cell types respond to ROS-rich environments, we can better predict and explain what cells are present that could be furthering the onset of corrosion and inflammation, in addition to necrosis and osteolysis. This work was published in the Journal of Biomedical Research Part A with the following citation:

Wiegand, MJ, Kubacki, GW, Gilbert, JL. 2019. Electrochemical potential zone of viability on CoCrMo surfaces is affected by cell type: Macrophages under cathodic bias are more resistant to killing. *Journal of Biomedical Materials Research Part A* 2019: 107A: 526– 534.

6. Sensing localized surface corrosion damage of CoCrMo alloys and modular tapers of total hip retrievals using nearfield electrochemical impedance spectroscopy (NEIS)

As previously described, ROS are a key component to the associated immune response during implantation and are produced as a result of mechanical wear. The ROS-mediated response can lead to an attack on the metal surface, eventually inducing severe corrosion and aseptic loosening of the joint[12, 14]. When metallic implants are damaged physically, electrically or chemically through various corrosive mechanisms, the damaged surface of the metallic implant is altered electrochemically by changing the OCP, impedance and other resistive characteristics[40, 50]. These wear mechanisms contribute to an increase in corrosion susceptibility

of the implant surface and indirectly affect how the surface interacts with the surrounding environment. We implemented a nearfield electrochemical impedance spectroscopy (NEIS) technique to assess the viability of a single implant surface exposed to varying ROS-inspired conditions. NEIS protocols were used to measure different forms of electrocautery and hydrogen peroxide-induced damage, as well as varying relative Goldberg scored locations on a severely corroded retrieved CoCrMo implant surface. This chapter focuses of defining heterogeneous surface electrochemical properties in response to corrosion type and damage event. We believe this work and technique can be used diagnostically when looking at revisions of metallic implants. This work has been submitted to the journal ACS Biomaterials Science & Engineering for publication.

7. Modeling synthetic synovial fluid for comprehensive in vitro testing in simulated periprosthetic joints using the Taguchi array approach

Joint fluid analysis is ordered to help diagnose the root cause of inflammation including infection, bleeding, osteoarthritis and other inflammatory diseases[60]. Simulated inflammatory joint fluid (fetal bovine serum, FBS) has been implemented in wear tests and shown to alter the passive oxide film on metallic biomaterials, thus affecting the implant's corrosion susceptibility[20]. We investigated how different natural synovial fluid constituents (hyaluronic acid, albumin, globulin, lecithin, ROS and metal ions) interact with one another in a range of synthetic formulations using a Taguchi factorial approach and analysis technique. Cellular responses such as viability and reduced glutathione (GSH) production were measured in addition to the comprehensive electrochemical response relating to the corrosion susceptibility and implant performance. This chapter focuses on how CoCrMo electrochemical properties are

affected when exposed to synthetic synovial fluid and what molecules and species significantly affect cell response, solution, and material properties with ROS as a key component. This work has been prepared for publication as is.

3.2. Overall flow and structure

Using the results published and presented in this work, we report that ROS are produced (Chapter 4) during corrosive conditions which directly affect viability (Chapter 5) and material properties (Chapter 6) and by understanding how all components of synovial fluid (Chapter 7) including ROS interact with one another and impact cellular and material properties, we will advance our *in vitro* implant simulations and hopefully *in situ* performance.

4. A fluorescent approach for detecting and measuring reduction reaction byproducts near cathodically-biased metallic surfaces: Reactive oxygen species production and quantification

Wiegand, MJ, Benton, TZ, Gilbert, JL. 2019. A fluorescent approach for detecting and measuring reduction reaction byproducts near cathodically-biased metallic surfaces: Reactive oxygen species production and quantification. *Bioelectrochemistry* 2019: 129: 235-241.

Author names:

Michael J. Wiegand[a,b], Thomas Z. Benton[c], Jeremy L. Gilbert[a,b,*]

Affiliations:

[a]Department of Bioengineering, Clemson University, Clemson, SC

[b]Clemson University-Medical University of South Carolina Program in Bioengineering, Charleston, SC

[c]College of Pharmacy, Medical University of South Carolina, Charleston, SC

4.1. Abstract

During tribocorrosion of biomedical alloys, potentials may shift cathodically across the metal-oxide-electrolyte interface resulting in the increased reduction of local oxygen and water molecules. The products of reduction are thought to include reactive oxygen species (ROS) as well as hydroxide ions. Using fluorescent probes, developed for labeling intracellular ROS-based hydroxyl radicals (OH·) and hydrogen peroxide (H_2O_2), ROS generation due to reduction reactions at cathodically biased CoCrMo alloy surfaces was measured directly. Using terephthalic acid (TA) and pentafluorosulfonylbenzene-fluorescein (PFF) as fluorescent dosimeters, it was found that OH· and H_2O_2 concentrations increased up to 16 hrs and 2 hrs, respectively. Decreases in fluorescence past these time points were attributed to the continuous onset of reduction reactions consuming both the ROS and/or dosimeter. It was also found that voltages below and including -600 mV (vs. Ag/AgCl) produced measurable quantities of H_2O_2 after two hours of polarization, with concentrations increasing with decreasing potentials up to -1000 mV. The detection and quantification of ROS in a clinical setting could help us better understand the role of ROS in the inflammatory response as well as their impact on corrosion behavior of biomedical alloys.

Keywords: Fluorescent probe; CoCrMo; reactive oxygen species; cathodic; hydrogen peroxide

4.2. Introduction

Cobalt-chromium-molybdenum alloy (CoCrMo) is among the most commonly-used alloys in orthopaedic, dental and spinal procedures due to its excellent mechanical and corrosion properties[14]. Most biomedical alloys, CoCrMo included, owe their corrosion resistance properties to a thin oxide film that forms as a protective barrier during passive behavior[12, 20]. Gilbert et al. demonstrated that when these oxide films are mechanically abraded, repassivation currents across the breached sample surface increase orders of magnitude, liberating electrons into the metal and resulting in potentials decreasing up to -1000 mV vs. SCE for titanium alloys and -800 mV for CoCrMo[76]. The rapid increase in currents is caused by the repassivation process taking place within milliseconds of the film's abrasion as well as the complementary ion dissolution processes[43]. Repassivation of the oxide film yields excess surface electrons which are then consumed in reduction reactions with local water and oxygen molecules, ultimately leading to hydroxide ion formation. Charge neutrality is maintained within the system with cathodic (reduction) currents compensating for the abrasion-initiated anodic currents[40]. Intermediates and byproducts of these reduction reactions are referred to as reactive oxygen intermediates (ROI) and reactive oxygen species (ROS). ROS that are formed as a result of these reactions, in addition to respiratory processes generated during immune cell responses stimuli, pose a major question: what sources contribute to the presence of ROS within an inflamed joint space?

Cathodic polarization of Ti6Al4V and CoCrMo alloys with cells cultured directly on the metal surfaces have been shown to induce cell death by an apoptotic process[45, 77]. This cell killing effect has been hypothesized to be a result of ROS generation by reduction reactions at the electrode surface. Cathodic Ti6Al4V surfaces have been shown to increase intracellular ROS levels resulting in a decrease in metabolic activity in osteoblast and monocyte-macrophages[47].

Dhar et al. found that cathodic voltages and currents were effective in hindering microbial and calcareous fouling due to an effective amount of electrochemically generated hydrogen peroxide at low current densities (< 100 μA)[78]. ROS also have damaging effects on the oxide film where it becomes porous[51, 52] with oxide resistance decreasing compared to commercial PBS solutions[48]. The presence of Fenton reactions ($Fe^{3+} + H_2O_2$) near CoCrMo surfaces can lead to an increase in both the oxidizing power of the solution and the open circuit potential (OCP), while also affecting the fretting corrosion response and frictional behavior[50]. As mentioned earlier, ROS can be formed through normal respiratory cell behavior and signaling or may be produced during respiratory burst processes associated with mononuclear phagocytes (e.g., macrophages, neutrophils, etc.) in inflammatory circumstances.

During respiratory ATP synthesis within the mitochondria, electrons are transported along a redox path from NADH and succinate that ends in the reduction of oxygen and water[32]. Water and oxygen molecules undergo reduction reactions using one or two electrons to form hydrogen peroxide (H_2O_2) and superoxide anion ($O_2^{\cdot -}$)[79]. The electron-chain transport production of ROS can also be activated during the apoptotic process as well as during signaling of inflammation and oxidative stress[80]. Apoptosis can be triggered through wear-particle induced inflammation and activation of local and recruited macrophages, where ROS are released alongside pro-inflammatory cytokines, chemokines and reactive nitrogen species (RNS)[81]. Wear-particle activated macrophages generate intracellular ROS and other species that further contribute to macrophage differentiation into osteoclasts, leading to enhanced bone resorption, osteolysis, oxidative stress build-up and ultimately aseptic loosening of implants[17, 23]. Most wear particles are released in the form of metal ions and metal oxides, where metal ions like cobalt (II) and chromium (III, VI) released from the CoCrMo surface during fretting corrosion have also

been shown to induce DNA and protein damage[26] in macrophage-like cells by activating the formation of ROS and altering the expression of antioxidant enzymes[25, 28]. All of these processes can happen concurrently within the joint space, leading to the formation of a pressurized fibrous tissue capsule filled with inflammatory species around the periprosthetic joint space, which can eventually cause greater wear and corrosion, and an increase in intraarticular pressure[13].

There are several ways to detect ROS concentrations both in solution and intracellularly, with the most consistent and accepted way being fluorescent labeling. The fluorescent-initiated probe dichlorodihydrofluorescein (DCFH) has become the accepted fluorescent marker for ROS detection, however it cannot differentiate between individual ROS and it is highly photosensitive, thus creating a large background fluorescence[69, 73]. Given that different ROS play specific roles in both physiological and clinical settings, there has been a recent effort in developing target molecules for quantifying individual ROS. Several fluorescent probes have been either discovered or synthesized to combat the downfalls of DCFH for the use of sensitive ROS detection. Each biomolecule is dependent on a specific mechanism to produce highly fluorescent products. For example, singlet oxygen ($^1O_2$) detection methods rely on chemiluminescent probes[82] as well as fluorescence-induced formation of endoperoxides[83]. Superoxide anion ($O_2^{-}\cdot$) fluorescent probes have been developed based on non-redox mechanisms of large aromatic complexes[84], to list a few.

There have been several probes developed for individual ROS detection and our manuscript focuses on measuring two common ROS individually near a cathodically-biased CoCrMo surface using selective dosimeters: terephthalic acid (TA) for hydroxyl radical ($OH\cdot$) detection and pentafluorosulfonylbenzene-fluorescein (PFF) for hydrogen peroxide (H_2O_2) detection. TA is a non-fluorescent aromatic compound that binds preferentially to hydroxyl

radicals over other reactive oxygen species to produce 2-hydroxyterphthalate, a stable fluorescent molecule (HTA) (Fig. 2)[33, 59]. PFF is a large aromatic complex that is deprotected at the sulfonyl linkage in the presence of H_2O_2, yielding the fluorescent fluorescein product[75]. Measuring individual ROS in a clinically relevant setting can lead to significant advances in predictive and diagnostic models relating to biomedical alloy lifetime and integrity, as well as the progression of the inflammatory response surrounding a metallic implant.

4.3. Materials and Methods

4.3.1. Materials

Terephthalic acid (TA), 2-hydroxyterephthalate (HTA), fluorescein (free acid), pentafluorobenzenesulfonyl chloride, 2, 6-lutidine, dichloromethane (CH_2Cl_2), silica gel, acetone, hydrogen peroxide, 30% (H_2O_2), ferrous chloride tetrahydrate ($FeCl_2 \cdot 4H_2O$), cobalt(II) chloride hexahydrate ($CoCl_2 \cdot 6H_2O$), chromium(III) chloride hexahydrate ($CrCl_3 \cdot 6H_2O$), hydrochloric acid (HCl), ethanol (EtOH), magnesium sulfate ($MgSO_4$), 1X phosphate buffered solution (PBS) and sodium chloride (NaCl) were all used as received (Sigma) without further purification. 96-well plates (Grenier) were used for standard curve calibration with 200 µL working volumes, and 24-well plates (Fisher) with 1 mL working volumes were used in fluorescent spectroscopy protocols.

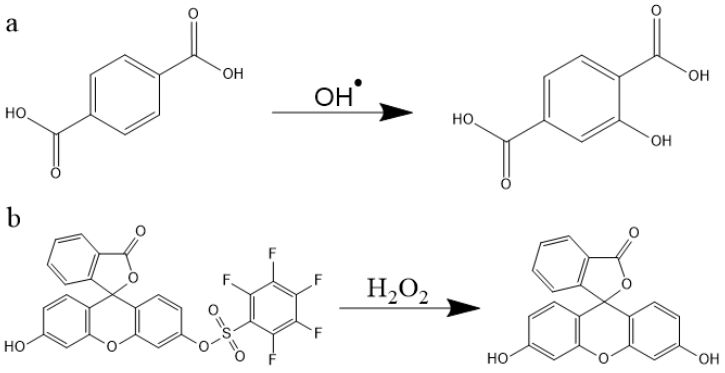

Figure 2: (a) Terephthalic acid in the presence of hydroxyl radicals will from the highly fluorescent 2-hydroxyterephthalate. (b) Pentafluorosulfonylbenzene-fluorescein is deprotected by hydrogen peroxide, leaving fluorescein [Adapted from Soh et al.[73]]

4.3.2. *Fluorescent Probe Synthesis*

TA and HTA were used as received for measurement of hydroxyl radicals (OH·). Pentafluorobenzenesulfonyl fluorescein (PFF) was synthesized (Fig. 3) using a method established by Maeda et al.[75] for measurement of hydrogen peroxide. Briefly (Appendix B.1), fluorescein (3 mM) and pentafluorobenzenesulfonyl chloride (3 mM) were dissolved in 2, 6-lutidine (5 mL)- CH_2Cl_2 (20 mL) and stirred at room temperature overnight. The solution was then diluted to 200 mL with CH_2Cl_2, washed twice with 1M HCl, brine and then dried over $MgSO_4$ crystals. Following solvent evaporation, silica gel chromatography was performed using CH_2Cl_2-acetone (20:1) to yield the final yellow solid PFF product. PFF molecular weight and formula (M_W = 562.4 g/mol, $C_{26}H_{11}F_5O_7S$)[75] were confirmed (Fig. 3) using mass spectroscopy analysis (Impact II, Bruker, MA).

4.3.3. *Fluorescent Probe Standard Curve Calibration*

Serial dilution (Appendix B.2.) of HTA and fluorescein (Fig. 4) was used to correlate final fluorescent intensities with concentrations. Initial concentrations of each fluorescent probe (100 µM) were dissolved in solvents (DI, 0.9% NaCl, 1X PBS) and serially diluted down to 0.01 µM (HTA in DI or 0.9% NaCl) and 50 pM (fluorescein in 1X PBS:EtOH at a 1:1 ratio). Relative standard curves were calculated by dividing the known concentration

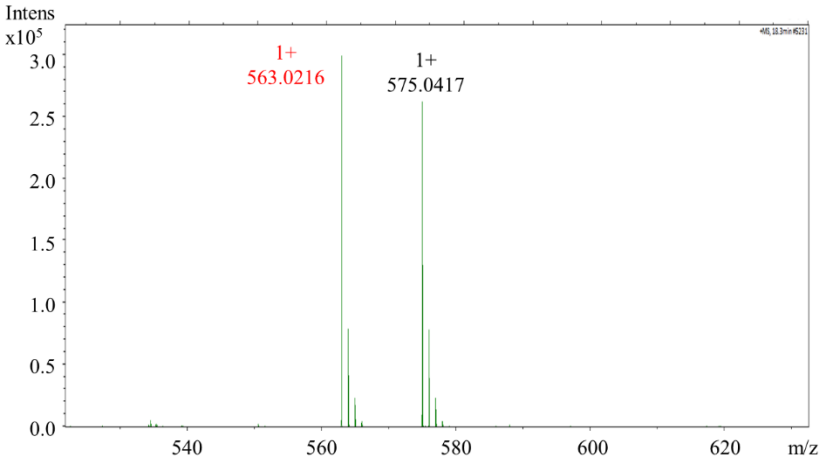

Figure 3: Pentafluorobenzenesulfonyl fluorescein (PFF) mass spectroscopy analysis. PFF molecular formula ($C_{26}H_{12}F_5O_7S$) and mass (563.0216 g/mol) were confirmed

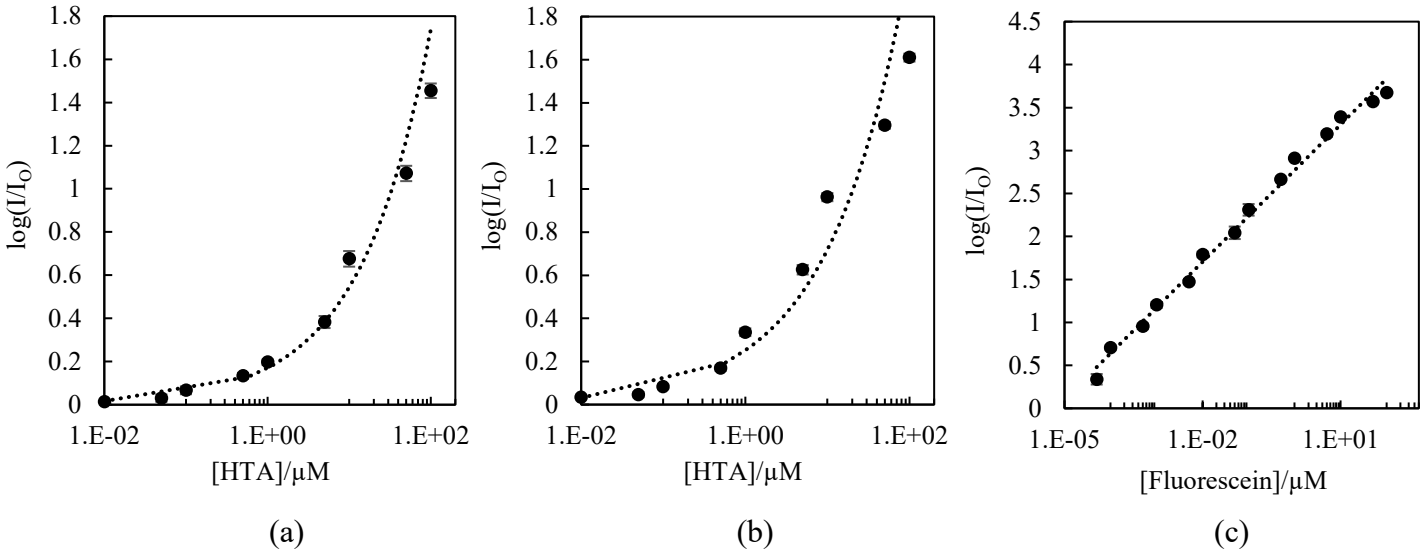

Figure 4: Standard relative fluorescent intensity curves used in electrochemical experiments as a function of known concentrations of (a) HTA (460 nm) dissolved in DI ($y = 0.17x^{0.5051}$, $R^2 = 0.9875$) and (b) 0.9% NaCl ($y = 0.2511x^{0.4569}$, $R^2 = 0.9764$), and (c) fluorescein (528 nm) dissolved in 1X PBS:EtOH, 1:1 ($y = 0.2314\ln(x) + 2.7708$, $R^2 = 0.9927$)

intensity average (I) by the average of the initial zero-intensity control ($I_O = 0$ M). The log of the relative intensity was reported ($\log[I/I_O]$). All standard curve solutions were read on autogain, resulting in different intensity values between solutions, therefore direct comparisons between solution intensities were not possible and all concentrations are relative.

4.3.4. Solution Preparation

Hydroxyl radical measurements were performed using the following solutions: (1) 2 mM TA (0.9% NaCl), (2) 2 mM TA + 1 mM $FeCl_2$ (0.9% NaCl), (3) 0.1 mM HTA (0.9% NaCl), and (4) 2 mM TA + 15 mM H_2O_2 (DI). Solution 1 represents TA dissolved in physiological levels of saline (0.9% NaCl). Solution 2 was prepared with iron(II) chloride ions acting as catalysts for Fenton and Haber-Weiss reactions with H_2O_2 molecules generated during reduction reactions at the implant surface. The Fenton and Haber-Weiss reactions would theoretically reduce the H_2O_2 and form reactive intermediates like hydroxyl radicals. Solution 3 was prepared and tested to determine if there was a consumption reaction of the fluorescent product, HTA, in the

electrochemical test conditions. Solution 4 was prepared with H_2O_2 in the presence of TA in DI. Solution hydrogen peroxide was implemented to test if surface electrons and eluted metal ions reduced H_2O_2, forming hydroxyl radicals and other reactive intermediates. This solution was prepared in deionized water to limit ions within the solution that would compete with TA or hydroxyl radicals. Metal ion salt solutions in the presence of H_2O_2, (5) $CoCl_2$ + H_2O_2 (DI) and (6) $CrCl_3$ + H_2O_2 (DI), were prepared to test an alternate hypothesis that free metal ions drive the conversion of H_2O_2 into hydroxyl radicals and not surface electrons. These solutions were tested without applied voltage (OCP) for 2 hrs. Metal salt concentrations were set at 100 mM $CoCl_2$/$CrCl_3$ and H_2O_2 concentrations ranged from 0.1-100 mM.

Hydrogen peroxide detection using PFF was measured by adding PFF dissolved in ethanol to the tested (7) 1X PBS solution. Briefly, PFF (0.9 mM) was dissolved in EtOH at its solubility limit[75] and any undissolved PFF was filtered through 0.4 μm filters. PFF-EtOH solutions (1 mL) were then added to the potentiostatically tested 1X PBS solutions (1 mL) and allowed to sit for 1 hr. Hydrogen peroxide is a more stable molecule with a significantly longer half-life than hydroxyl radicals, therefore PFF was not added directly to test solutions during potentiostatic tests. This omitted the need to test if the experimental conditions consumed the fluorescent product (fluorescein).

4.3.5. *Electrochemical Experiments*

High-carbon CoCrMo alloy discs (ASTM F-*1537*) with an exposed surface area of 0.641 cm^2 were polished using silica paper up to 600 μm grit, rinsed with deionized water and sonicated with 70% ethanol for 30 mins and dried using nitrogen gas. CoCrMo discs were assembled in glass chambers using a three-electrode system with the metal disc as the working electrode, a platinum wire (Pt) counter electrode and chlorided-silver wire (Ag/AgCl) reference

electrode. CoCrMo electrodes in the various solutions (1 mL total volume) were held potentiostatically at open circuit potential (OCP) for 30 mins before applied potential (-1V vs. Ag/AgCl) for timed trials up to 16 hrs. Voltage-dependent trials were tested for 2 hrs starting at -1000 (vs. Ag/AgCl) and ending when there was no longer detectable fluorescence. A new set of CoCrMo discs (n=3) were used for each timed and voltage-dependent trial. Currents (i) were recorded prior to fluorescent spectroscopy analysis.

4.3.6. *Fluorescent Spectroscopy*

HTA (λ_{ex} = 315 nm, λ_{em} = 425 nm) and fluorescein (λ_{ex} = 485 nm, λ_{em} = 530 nm) fluorescent intensities were measured following applied potential. Chambers were sonicated in order to release any adhered molecules from the metal or glass surfaces into solution. Supernatants were removed and placed in 24-well plates in 1 mL volumes. Three control wells (I_O) were tested alongside the three sample wells (I). Plates were read in the microplate reader (Synergy 2, Biotek, Winooski, VT) at a fixed gain with measured light flux falling on 50% using a tungsten lamp and appropriate filter sets. Log[I/I_O] was plotted against time and voltage. Hydroxyl radical and hydrogen peroxide concentrations were calculated by applying regression lines of best fit (Excel) from the standard curves to the measured relative fluorescent intensities, assuming a one-to-one stoichiometric ratio of HTA:hydroxyl radical and fluorescein:hydrogen peroxide.

Hydrogen peroxide concentrations were also calculated for comparison using the currents obtained at each time point during the -1000 mV (vs. Ag/AgCl) potentiostatic trials on CoCrMo. Hydrogen peroxide concentration (ρ) was calculated using the following density equation and reduction reaction

$$\rho = \frac{M_w}{nFV}\int_0^m idt \qquad [13]$$

$$O_2 + 2H_2O + 2e^- \rightarrow H_2O_2 + OH^- + OH\cdot \quad [14]$$

where ρ is the concentration of hydrogen peroxide in solution (g/mL), M_w is the molecular weight of the species produced (H_2O_2, 34.0147 g/mol), n is the moles of electrons needed per moles of H_2O_2 produced (2, See Eqn. 14), F is Faraday's constant (96,485 C/mol e^-), V is the volume of solution (1 mL), i is the measured current (C/s) after m seconds. The concentration (g/mL) can then be converted into a molar concentration (M) by dividing by the molecular weight (g/mol). It is estimated that the limited current efficiency for hydrogen peroxide production without stirring of the electrolyte is 10%[78], therefore we compared the measured hydrogen peroxide concentrations with this assumption.

4.3.7. *Statistical Analysis*

All experiments and techniques were repeated in triplicate. Averages and standard deviations were reported using one-way ANOVA and Tukey's *post hoc* pairwise comparison with simple effect. A minimum 95% confidence interval ($p < 0.05$) was taken to be significantly different.

4.4. *Results*

4.4.1. *Electrochemistry*

There was a significant effect on current (i) with the addition of $FeCl_2$ (Fig. 5). Measured currents were significantly higher ($p < 0.01$) than all other test solutions up to 4 hrs, and significantly higher ($p < 0.05$) up to 8 hrs. Solutions containing 2 mM TA and 2 mM TA + 1 mM $FeCl_2$ displayed decreased currents with time and 0.1 mM HTA and 0.9% NaCl solutions showed no change in currents with time. Currents measured for H_2O_2 trials before the addition of PFF + EtOH solutions decreased initially and then plateaued for the duration of the experiments, as expected, up to 16 hours. Solutions containing 2 mM TA + 15 mM H_2O_2 currents are not displayed due to lack of conductivity of the solvent (deionized water). During potentiostatic trials at -1V with $FeCl_2$ solutions, a bright yellow precipitate formed on the surface of the CoCrMo discs. No other solution produced any visible reaction precipitate.

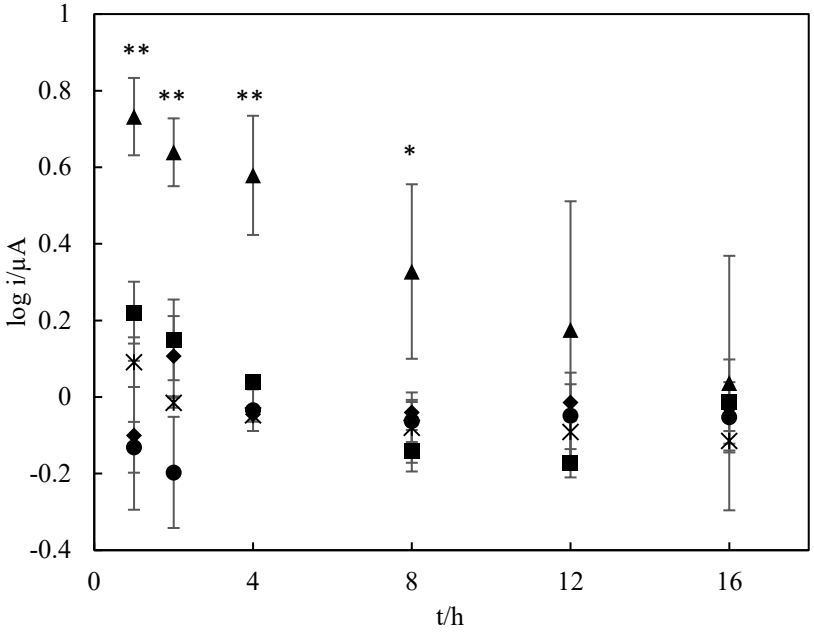

Figure 5: Current (i) measured (absolute) as a function of time in the presence of CoCrMo with -1V (vs. Ag/AgCl) applied potential: 0.9% NaCl (circle), 1X PBS (cross), 2 mM TA (0.9% NaCl) (square), 0.1 mM HTA (0.9% NaCl) (diamond), and 2 mM TA + 1 mM $FeCl_2$ (0.9% NaCl) (triangle). Currents were measured for NaCl based solutions with pure 0.9% NaCl treated as the control. Solutions containing $FeCl_2$ currents were significantly higher ($p < 0.05$) in current than all NaCl based solutions up to 8 hrs, indicating a change in the reduction reactions at the surface

4.4.2. *Fluorescence Spectroscopy*

The log relative fluorescent intensity (Fig. 6) increased for solutions containing TA + H_2O_2 up to 16 hours indicating the generation of hydroxyl radicals. Samples containing only TA (0 M H_2O_2) did not produce a change in relative fluorescence ($\log[I/I_O] \approx 0$, 0 hrs $\leq m \leq$ 16 hrs), and samples containing TA + $FeCl_2$ and HTA decreased as time increased. The decrease in these samples was rapid in the first four hours, after which the log relative fluorescent intensity remained constant with increasing time. This indicated that the HTA lost its fluorescent intensity or was consumed with continued exposure to the cathodic electrode. Fluorescein detection solutions containing 0.9 mM PFF (1X PBS:EtOH, 1:1) increased in relative log fluorescent intensity up to 2 hrs and then plateaued in intensity up to 16 hrs.

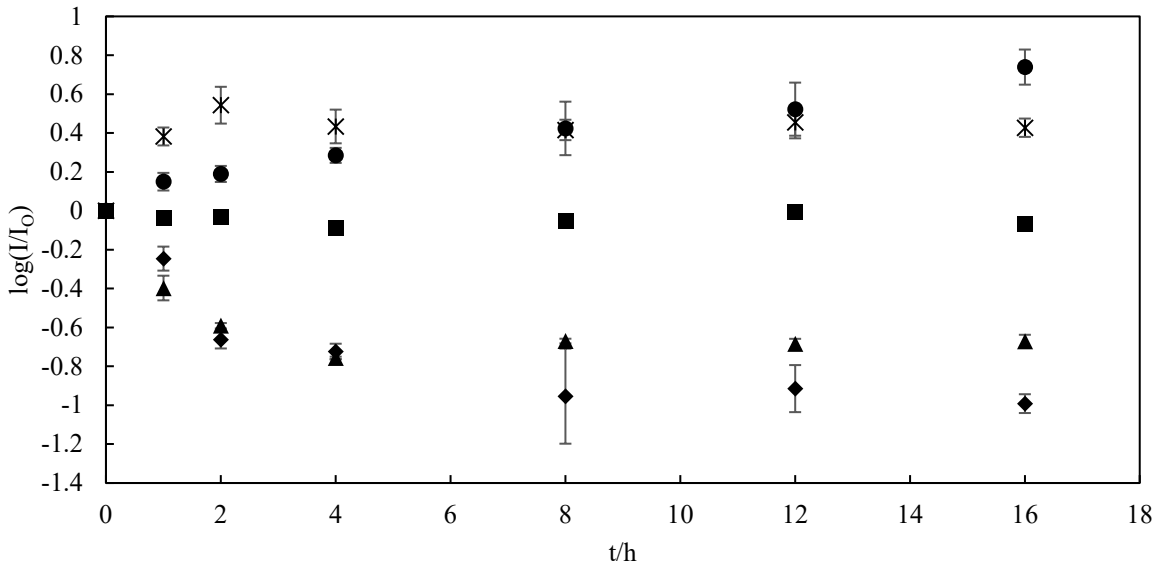

Figure 6: HTA and PFF fluorescence vs. time of applied potential (-1V): 2 mM TA (0.9% NaCl) (square), 2 mM TA + 15 mM H_2O_2 (DI) (circle), 0.1 mM HTA (0.9% NaCl) (diamond), 0.9 mM PFF (1X PBS:EtOH, 1:1) (cross), and 2 mM TA + 1 mM $FeCl_2$ (0.9% NaCl) (triangle). Final fluorescent intensities are relative to initial intensities measured of untested solutions at each time point (I/I_O), where positive $\log(I/I_O)$ values indicate an increase in fluorescence and negative values indicate a decrease from the starting solution

Alternate hypothesis tests involving Co(II) and Cr(III) ions did not increase in fluorescence intensity with increasing H_2O_2 concentrations in the absence of applied voltage (data not shown).

The measured H_2O_2 concentrations increased for solutions containing 0.9 mM PFF (1X PBS:EtOH, 1:1) up to 2 hours (Fig. 7), followed by a steady-state up to 16 hours indicating that hydrogen peroxide was generated and consumed within the electrochemical cell. Concentrations calculated using Eqns. 13-14 were plotted as a function of time with an estimated 10% conversion of oxygenated molecules (Fig. 7). Hydroxyl radical and hydrogen peroxide relative fluorescent intensities were converted into concentrations using the standard curves (Table 1).

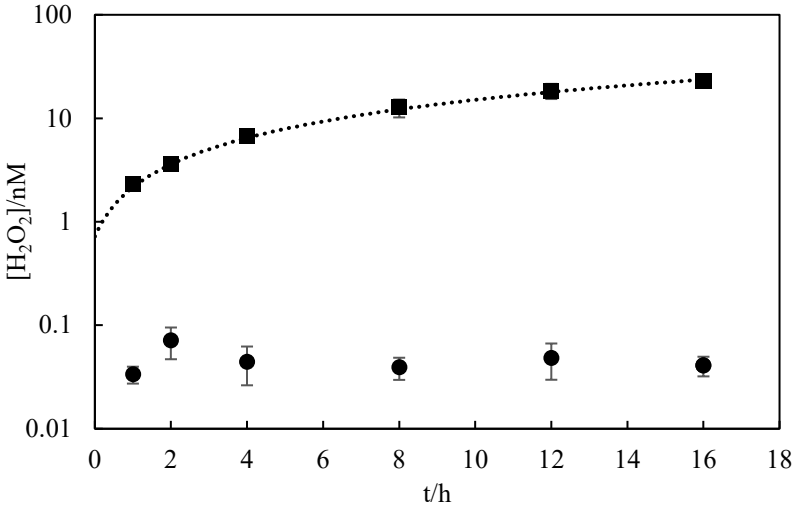

Figure 7: Measured (circle) and calculated (square) H_2O_2 [nM] concentrations vs. time of applied potential (-1V) of the CoCrMo surface. Calculated concentrations were made using measured 1X PBS solution currents and assuming a 10% reduction of oxygen and water molecules into hydrogen peroxide molecules, and fit to a linear regression ($y = 1.4343x + 0.7198$, $R^2 = 0.9966$)

Fluorescent intensities of potential dependent trials (Fig. 8) were measured after 2 hrs where the log relative fluorescent intensity decreased from -1000 mV to -600 mV (vs. Ref), at which point there was no longer any detectable H_2O_2 in solution. Voltages above -600 mV were not tested due to this outcome.

4.5. Discussion

The experimental design using TA and PFF as dosimeters successfully captured the production of ROS near a cathodically-charged CoCrMo surface. It was found that TA in the presence of H_2O_2 in DI water at -1V vs. Ag/AgCl yielded increasing amounts of HTA with time. We hypothesize that hydrogen peroxide is actively produced at cathodically biased CoCrMo surfaces in all TA and PFF solutions and is subsequently reduced, at least partially, through the excess electrons at the CoCrMo surface to hydroxyl radicals and/or hydroxide ions. This can explain the increase in HTA fluorescence as a direct result of the addition of H_2O_2 in solution where hydrogen peroxide molecules are reduced into hydroxyl radicals and other reactive intermediates, as well as the increase in fluorescein detection in PFF trials in the absence of H_2O_2 initially in solution. We hypothesize that the fluorescence levels off due to a net balance between H_2O_2 production and consumption within the system. The alternate hypothesis tests indicate that surface electrons, not metal ions, are critical for the conversion of solution hydrogen peroxide to hydroxyl radicals in the presence of CoCrMo. It is not known at this time if metal ions in combination with electrons contribute to the reduction of hydrogen peroxide ions. Further tests measuring solution ions after cathodic polarization would help

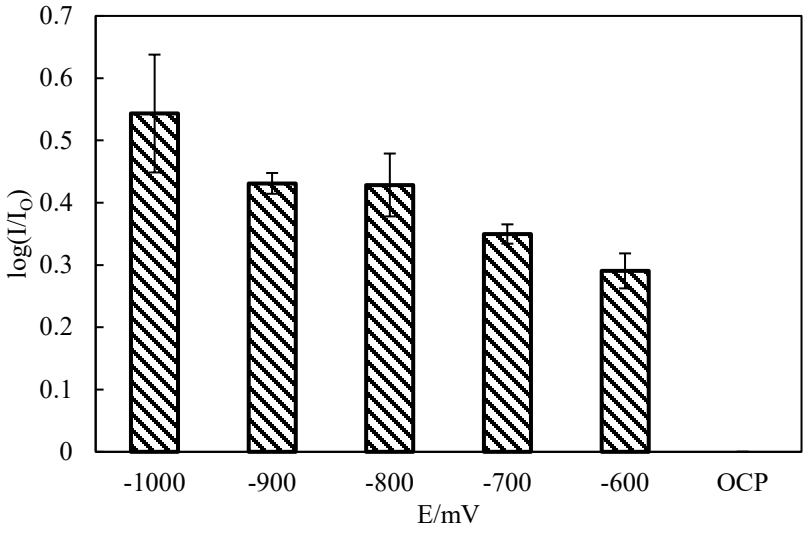

Figure 8: Fluorescein fluorescence (528 nm) vs. applied potential (E) after 2 hrs. There was a net zero intensity at potentials above -600 mV (vs. Ag/AgCl), indicating that reduction reactions at these higher voltages do not produce a measurable amount of H_2O_2 under the given experimental conditions

explain if metal ions are produced in the given experimental set-up and to what quantity. The hydrogen peroxide concentration results also suggest that there is a significant reduction in detected H_2O_2, assuming the 10% conversion of water and oxygen molecules. This aligns with our hypothesis that H_2O_2 is consumed as reaction time is increased.

One of the purposes of this study was to provide evidence of H_2O_2 production from a cathodically-biased CoCrMo surface and use this information to support H_2O_2-induced cell death modes seen during *in vivo* experiments. Brenner et al. found that C6 glioma cells incubated from 1 to 24 hrs with H_2O_2 resulted in median cytotoxic concentrations (EC_{50}) of 500 to 30 µM, respectively[85].

t/h	0	1	2	4	8	12	16
[HTA Consumption]/ µM	100 ± 0	57.4 ± 8.51	21.9 ± 2.26	19 ± 1.66	12.7 ± 5.49	12.6 ± 3.27	10.3 ± 1.17
[HTA Production]/ µM	--	0.36 ± 0.29	0.57 ± 0.28	1.35 ± 0.39	3.57 ± 2.15	5.42 ± 2.84	10.83 ± 2.80
[Fluorescein]/ nM	--	33.6 ± 6.23	71.1 ± 24.1	44.3 ± 18	39.1 ± 9.44	48.2 ± 18.5	40.9 ± 8.79

Table 1: HTA [µM] and fluorescein [nM] molar concentrations as a function of time against -1V (vs. Ag/AgCl) in the presence of CoCrMo. Molarities were calculated using standard curve regression line fits. Fluorescent probe molar concentrations are assumed to be equal stoichiometric ratios with corresponding hydroxyl radicals and hydrogen peroxide molecules

Schraufstatter et al. studied alike incubation effects of $P388D_1$ leukocytes exposed to 2.5 mM H_2O_2, where cells retained 10% viability after 6 hrs[86]. Similar to how different cell phenotypes display different ranges of viability in response to a spectrum of potentials or an 'electrochemical zone of viability'[87], it is reasonable to assume that there exists a cell-specific lethal dose of H_2O_2.

It is also possible that the generation of ROS may impact the corrosion resistance of the CoCrMo alloy itself by impacting the oxide film on the surface. Such effects may play a role in

ongoing corrosion within biological systems where the alloy electrode potential reaches these levels within crevices during mechanically assisted crevice corrosion.

This methodology is limited by its ability to be translated *in vivo* as well as understanding the individual and overall kinetics of ROS production and consumption, as seen from the preliminary hydroxyl radical and hydrogen peroxide trials. In addition, this work did not explore the wide range of other ROS-based chemistries that may be generated by cathodic electrode surfaces. The primary goal of this work was to demonstrate the generation of any ROS. Future work will assess the possibility of additional species being generated.

Other labs have successfully converted H_2O_2 into hydroxyl radicals and measured output using HTA, however these groups explored different experimental conditions and capture modes such as liquid-phase pulsed corona discharges, radiation or sonochemical spectroscopy[88-90]. Tang et al. used Co^{2+} to catalyze the aromatic hydroxylation of TA to HTA in the presence of H_2O_2 using flow injection analysis spectrofluorimetry[91]. Other lab groups have also looked into the effects of Fenton-like reactions involving transition metal ions in the presence of TA and H_2O_2. Hassanzadeh et al. found that TA mixed with cholesterol oxidase generated-H_2O_2, silver nanoclusters (AgNC) and MoS_2 nanosheets, resulting in high HTA fluorescence emission[92]. This would indicate that silver ions have a greater effect in Fenton-like reactions with H_2O_2 than cobalt(II) and chromium(III) ions.

Other limitations surrounding the work with TA involve the use of saline based solutions where output resulted in either a net zero or decreased fluorescence intensity. We hypothesize this is due to free salt or iron ions in solution competing and preferentially binding to the TA over hydroxyl radicals, explaining the yellow precipitate in solutions containing $FeCl_2$. It was later found that iron(III) chloride-hexahydrate and TA are used to make crystal-like metal

organic frameworks (MOF) using basic dissolution[93], similar to our solution preparation. Zhao et al. first reported the use of disodium terephthalate as a novel electrode for sodium-ion batteries, where TA in the presence of sodium ions and electrons rapidly form a high-performance anode material[94]. This confirms our hypothesis that iron(II) and sodium ions were competing with hydroxyl radicals, leading to a decrease in fluorescence intensity. It remains unclear why HTA is consumed within our experimental set-up as well as why it decays similar to a first-order reaction, however we have determined that HTA is not the ideal dosimeter for our experimental conditions and other fluorophores are being considered. Consequently, PFF demonstrated that it reacts with solution hydrogen peroxide during cathodic potentials likely present during mechanical abrasion of the surface and can be a useful probe in the future when simulating *in vivo* environments such as in the presence of retrieved synovial fluids or within tribocorrosion experimental chambers.

4.6. Conclusion

Reactive oxygen species (ROS) are created during reduction reactions at CoCrMo surfaces under cathodic potentials. Such potentials may arise as a result of mechanical abrasion of the oxide film on metallic implants during tribocorrosion processes. By applying protocols developed for fluorescently labeling individual ROS, it was shown that concentrations of hydroxyl radicals and hydrogen peroxide increase with increasing time. Additionally, hydrogen peroxide was shown to be both generated and consumed within the electrochemical experiments, assisting in the formation of hydroxyl radicals through reduction reactions. Hydrogen peroxide concentration gradients were highest in short term potentiostatic trials, indicating that the ROS has its greatest effect during the initial applied potential. It has been previously demonstrated that cathodic excursions have a significant effect on local cell viability, therefore determining the

quantities and vicinity to the implant surface of these reaction byproducts is critical in our understanding of the inflamed joint space during mechanically assisted corrosion.

5. Electrochemical potential zone of viability on CoCrMo surfaces is affected by cell type: Macrophages under cathodic bias are more resistant to killing

Wiegand, MJ, Kubacki, GW, Gilbert, JL. 2019. Electrochemical potential zone of viability on CoCrMo surfaces is affected by cell type: Macrophages under cathodic bias are more resistant to killing. *Journal of Biomedical Materials Research Part A* 2019: 107A: 526– 534.

Author names:

Michael J. Wiegand[a,b], Gregory W. Kubacki[a,b], Jeremy L. Gilbert[a,b,c,d,*]

Affiliations:

[a]Department of Biomedical and Chemical Engineering, Syracuse University, Syracuse, NY

[b]Syracuse Biomaterials Institute, Syracuse University, Syracuse, NY

[c]Department of Bioengineering, Clemson University, Clemson, SC

[d]Clemson University-Medical University of South Carolina Program in Bioengineering, Charleston, SC

5.1. Abstract

Electrochemical interactions at the cell-metal interface determine cell viability and influence behavior in response to different electrode potential conditions, specifically cathodic biases. Mechanically assisted crevice corrosion, for example, induces cathodic potentials and the associated electrochemical consequences of increased reduction reactions at the implant surface may affect cell viability in a manner that is different for various cell phenotypes. Monocyte macrophage-like U937 cells were cultured on CoCrMo metal surfaces *in vitro* for 24 hours to assess cell behavior in response to sustained applied voltages. The electrochemical zone of viability for U937 cells polarized for 24 hours *in vitro* was $-1000 \leq mV < +500$, compared to $-400 < mV < +500$ for MC3T3-E1 preosteoblast-like cells cultured under the same conditions, likely as a result of intrinsic apoptosis. Voltages above +250 mV had a lethal effect on U937 cells that was similar to that seen previously for MC3T3-E1 cells on biased CoCrMo surfaces. It appears that cell phenotype directly influences behavior in response to cathodic electrochemical stimuli and that the monocyte macrophage-like cells are more resistant to cathodic potential stimuli than preosteoblasts. This may be due to a glutathione-based increased ability to quench reactive oxygen species and inflammatory-associated radicals hypothesized to be generated during reduction of oxygen.

Keywords: Electrochemical; cell viability; macrophage; CoCrMo; cathodic

5.2. Introduction

Cobalt-chromium-molybdenum (CoCrMo) alloy has been in use as a biomaterial for nearly ninety years due to its advanced ability to resist wear and corrosion when compared to other alloys[19, 44, 95], however, CoCrMo is susceptible to many types of corrosion typically associated with mechanically assisted crevice corrosion where the environment may be chemically and/or mechanically aggressive[2, 40]. During mechanically assisted crevice corrosion (MACC), electrode potentials at the CoCrMo surface can shift as far negative as -900 mV (vs. Ag/AgCl) from an unabraded open circuit potential of about -250 mV (vs. Ag/AgCl)[96]. On the anodic side, surface potentials can reach over +600 mV (vs. Ag/AgCl) in the presence of the inflammatory specie hydrogen peroxide[50]. Potentials of these magnitudes (above the breakdown potential for CoCrMo) result in the degradation of the protective oxide film and can result in rapid killing of cells cultured on the CoCrMo surface[45, 46]. The effects of both cathodic and anodic potentials on cells cultured on CoCrMo surfaces have important clinical implications that require additional study. One such question is related to the cell-specific response to cathodic and anodic potential conditions on cell viability. Do different cell types (e.g., immune cells versus preosteoblast-like cells) respond differently to cathodic and anodic potentials when these cells are cultured on CoCrMo surfaces?

The study of immune cell responses and interactions with metal alloys has primarily focused on the release of pro- and anti-inflammatory species and cellular behavior in response to metal ions (oxidation half-cell of corrosion) and particles generated due to tribocorrosion[22, 29, 97-100]. Metal ion release due to oxidation or abrasion of the CoCrMo alloy surface has been seen extensively when large anodic voltages [e.g., chromium, nickel, cobalt and molybdenum above +500 mV vs Ag/AgCl] or cathodic voltages [e.g., chromium at -1000 mV vs Ag/AgCl][45] are

developed or imparted. Chromium is potentially released in two forms (Cr^{+3}, Cr^{+6}) and cobalt is typically released as cobalt(II)[8]. Co^{+2} and Cr^{+3} ions can permeate the cell membrane and induce protein oxidation[29], initiating the release of tumor necrosis factor alpha (TNF-α) and interferon gamma (INF-γ) within inflammatory cells[28, 98, 101], and thereby stimulating the secretion of chemokines and cytokines linked as mediators of osteoarthritis and aseptic loosening of implants[12, 102]. Macrophages activated with lipopolysaccharide (LPS) express TNF-α and chemokine monocyte chemo-attractant protein-1 (MCP-1) when cultured on CoCrMo alloy[103]. Surface roughness and morphology[104] has also been documented to impact inflammatory cell activation responses. Anti-inflammatory cytokine (IL-10) production is favored on microrough CoCrMo surfaces whereas pro-inflammatory cytokine (TNF-α, IL-6 and IP-10) production is favored on smooth CoCrMo surfaces[19].

Reactive oxygen species (ROS) are another set of chemically active molecules that can contribute to oxidative stress on the cell as well as structural damage to the alloy surface. ROS like superoxide anion ($O_2^{\bullet-}$) and hydrogen peroxide (H_2O_2) are naturally produced by a drop in the mitochondrial transmembrane potential[64] in low concentrations through aerobic respiration and are neutralized intracellularly via catalase and superoxide dismutase enzymes[105]. ROS can also be synthesized via respiratory burst processes in immune and inflammatory cells in response to foreign bodies and infection. Neutrophils, monocytes, macrophages, foreign body giant cells, and even osteoclasts are known to generate ROS in respiratory burst processes when activated[106].

ROS are also produced at electrode surfaces during the reduction of oxygen. Reduction reactions must accompany associated anodic processes like the repassivation of the oxide film during mechanically assisted crevice corrosion (MACC)[96]. Molecular oxygen (O_2) and water (H_2O) are reduced near the electron-rich metallic surface reduction half-cell[40] during corrosion.

These molecules may be converted to hydroxyl radicals ($OH^{\cdot}$) as well as other electrochemically active ROS such as superoxide anions and singlet oxygen radicals as intermediates in the oxygen reduction reaction[107]. Hydrogen peroxide is produced as a catalytically-derived intermediate in the conversion of superoxide radicals to water and molecular oxygen via surface electron interactions and superoxide dismutase[80]. ROS build-up results in oxidative stress[64], abnormal cellular processes, mitochondrial and membrane lipid disruption[80], and eventual programmed cell death (i.e., apoptosis)[63].

Retrieved CoCrMo alloy hip implant surfaces with damage that is hypothesized to be the result of inflammatory cell-induced (ICI) corrosion has been recently reported[14, 15, 108]. Evidence of cellular remnants and biological material on the surfaces of CoCrMo alloy[14] was characterized as osteoclast resorption and the oxidizing effect of molecules (i.e. cytokines, hydrogen peroxide) released from vesicles during necrosis[14]. While some of these observations were later found to be the result of electrocautery effects[72], there were other examples where cell-induced corrosion appeared to play a role. ICIC has been simulated on stainless steel and titanium alloy surfaces using osteoclasts *in vitro*[18], but it has yet to be extensively characterized on CoCrMo alloy surfaces.

ICI damage has also been reported on other biomaterials such as polyurethane insulated leads for pacemakers. *Ex vivo* analysis revealed extracellular hydrogen peroxide permeated through the outer silicone insulation due to metal ion oxidation (MIO) of the outer metal contacting surface[109], and this phenomenon was reproduced *in vitro*[110]. The MIO mechanism resulted in crack propagation throughout the polyurethane and ultimate failure of the leads. It is hypothesized that monocyte derived macrophages and foreign body giant cells are the primary

mediators of polyurethane degradation *in vivo*[110], and that these cells release reactive chemical species (RCS) and reactive oxygen intermediates (ROI) that accelerate oxidative biodegradation.

It has been previously reported that pre-osteoblast-like cells (MC3T3-E1) cultured on CoCrMo alloy surfaces exhibit an 'electrochemical zone of viability'[45]. In this voltage range, MC3T3-E1 cells remained viable after 24 hours of applied potential between -400 and +350 mV (vs Ag/AgCl). Cells outside this zone experienced cell death in the form of apoptosis (-400 mV and below) and necrosis (+350 mV and above)[45]. Metal ions (Co, Cr, Mo, Ni) are released from the surface in large amounts at +500 mV and at -1000 mV (Cr). These ions likely contributed to the necrotic cell death mechanism in the upper anodic voltages (> +500 mV), whereas the apoptotic MC3T3-E1 cells within the large cathodic voltages (< -400 mV) were thought to be subjected to oxidative stress triggered by ROS[45]. ROS facilitated cellular caspase activation[111] and at cathodic voltages outside the viability range, MC3T3-E1 cells experienced apoptosis based on caspase-3 and -9 release[45]. It was hypothesized from this work that all cell-types subjected to an electrochemical bias experience a 'zone of viability' however it was not clear what the effect of cell phenotype was on the viability range as different cells possess different defense mechanisms.

In this study, monocyte macrophage-like cells (U937 monocytes) were induced to adhere to and be cultured on CoCrMo alloy and the resulting viability and cellular morphological changes as a function of anodic and cathodic voltages were investigated. It is hypothesized that these cells would be able to tolerate a larger electrochemical zone of viability.

5.3. Materials and Methods

5.3.1. Sample Preparation

CoCrMo high-carbon alloy discs (ASTM F-*1537*) with an exposed surface area of 5.1 cm^2 were mechanically polished to 600 μm grit followed by 1.0, 0.3 and 0.05 μm alumina polish until a mirror finish was obtained. Samples were then rinsed with deionized water and sonicated for 30 minutes in 70% ethyl alcohol to remove polishing material. Following sonication, samples were UV sterilized for at least 2 hours prior to use. To avoid contamination, samples were always handled with sterile tweezers and nitrile gloves.

5.3.2. Cell Culture

U937 macrophage monocyte-like inflammatory cells and MC3T3-E1 pre-osteoblast-like cells were grown in 90% Gibco's® RPMI 1640 medium (ThermoFisher) and 10% fetal bovine serum (FBS) (ThermoFisher) in separate T-75 flasks (Corning, NY) until confluent. Then, 200,000 U937 cells were pipetted at a volume of 50 μL (4,000 cells/μL) and seeded on the surface. Phorbol 12-myristate 13-acetate (PMA) (Sigma) was added to the media at a concentration of 100 ng/mL before cell seeding. This was added for better U937 cell attachment and adhesion to the metallic surface. PMA was not included with the MC3T3-E1 media volume and cells were seeded at a volume of 20,000 cells/50 μL due to the larger size of the MC3T3-E1 cells, and in agreement with previously done studies in the lab[45].

After cells were plated, discs were assembled in glass-chambers (Fig. 9) using a standard three electrode system where the CoCrMo disc served as the working electrode, and a graphite rod and chloride silver wire (Ag/AgCl) served as the counter and reference electrodes, respectively. The glass chamber was then carefully filled with RPMI media + FBS (20 mL total)

down the side of the glass as to not disturb the cells on the metal surface. The chamber was then capped with a rubber stopper where the chloride silver wire and graphite counter electrode were inserted into the media. The rubber stopper had an additional air hole to allow for gas exchange between the chamber and incubator. After the chamber was placed in the incubator (37°C, 5% CO_2), a potentiostat was connected to the electrodes and the incubator was sealed. Samples were held at the open circuit potential (OCP) with no applied voltage for 1 hour before cell viability experiments.

5.3.3. Cell Viability

U937 cell viability experiments were tested using CoCrMo discs (n=3) and potentials ranging from -1000 to +1000 mV (vs. Ag/AgCl) for 24 hours in increments of 250 mV. Cells were not tested at -250 mV, as this potential is similar to OCP and we did not expect to see a killing effect of cells. U937 cells at 0 mV served as the control group for cell viability experiments since it lies in the middle of the already established MC3T3-E1 'zone of viability.' MC3T3-E1 cells were only tested at -1000 and -750 mV to confirm total cell death data at large cathodic voltages seen previously[45]. After applied voltages, samples were washed with phosphate buffered saline (PBS) three times before fluorescent imaging stains were applied.

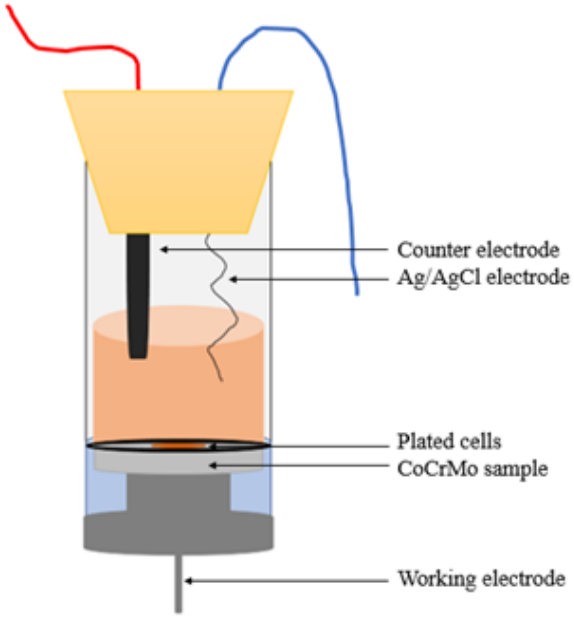

Figure 9: Experimental glass electrochemical chamber used in cell viability experiments

A live/dead/ viability/cytotoxicity kit for mammalian cells (L3224, Invitrogen, Oregon) was

used to confirm cell death at the predetermined voltage after 24 hours (vs. Ag/AgCl). After PBS washing, 3.33 μM of calcein AM and 4 μM of ethidium homodimer-1 in 3 mL of PBS was pipetted into each sample chamber. The chambers were then covered with aluminum foil and left in the bio-safety cabinet at room temperature with the lights off for 30 minutes to prevent photobleaching. The dye solution was then removed from the discs and the surfaces were then washed three times with PBS. Chambers were then disassembled, and discs were inverted on top of rubber O-rings in PBS filled petri dishes to avoid contact with the bottom of the dish. The dishes were then covered and transported for imaging.

Fluorescent imaging for live/dead assessment of cells was performed using an inverted microscope (Leica DFC 340 FX, Leica, GER) with a CCD mono-12 bit camera (Q-imaging, Canada) and an X-Cite 120 light source (EXFO America, TX). Leica application suite (LAS) version 4.1 (Leica Microsystems, GER) was used to capture live and dead images, and subsequently overlay images for further analysis. Live and dead cells were imaged using fluorescein bandpass filter (FITC) and Texas red dye filter, respectively. Discs were imaged in successive magnifications from 5X to 40X, and 10 images were taken at 20X at random areas on the surface for cell viability calculations. Dead cells were stained red-fluorescent from the ethidium homodimer-1 solution binding to the free or fragmented DNA, and live cells were stained with calcein AM. Calcein AM is converted to green-fluorescent calcein due to hydrolysis of the acetoxymethyl ester bonds (Invitrogen). Total cells of each image were counted, and the number of live and dead cells were reported for each image. Averages and standard deviations were reported for each potential and cell type.

5.3.4. *Cell Size*

ImageJ software (NIH) was used to measure cell size averages from live-dead images. U937 cells at 0 mV were used as the control group for cell size measurement, similar to cell viability experiments. Using previous techniques[45], cell size as a function of voltage was calculated by converting fluorescent images to 8-bit gray-scale images, conversion to binary images, and then subtracting the background using the sliding paraboloid method. Fast Fourier Transform (FFT) of all images using a bandpass filter to filter structures smaller than 3 pixels and larger than 10 pixels and a threshold inverse filter were performed prior to cell size analysis. ImageJ analyzed all cells within the image reporting a circularity between 0.4-1.0.

5.3.5. Scanning Electron Microscopy Analysis

Samples were sterilized and dehydrated with 70% ethyl alcohol before scanning electron microscopy analysis following fluorescent imaging. The morphology of the cells after cell viability tests was investigated using a scanning electron microscope (SEM; Jeol JSM-5600, Tokyo, Japan). Following dehydration, samples were dried and sputter coated with gold at 50 mTorr chamber pressure (Model Desk II, Denton Vacuum, NJ). Images were taken in secondary emission from 2.1 kV to 5.0 kV. Visual inspection was used to categorize cell morphologies and biological surface remnants.

5.3.6. *Statistical Analysis*

Results were reported as averages and standard deviations (SD) and each experiment was repeated in triplicate unless otherwise stated. Two-way ANOVA and Tukey's *post hoc* pairwise comparison with simple effect were performed to compare the effect of voltage on cell viability and size with a $p < 0.05$ taken to be significantly different.

5.4. Results

5.4.1. *Cell Viability*

Cell live/dead results, (Fig. 10-11), show that U937 cells retained viability from -1000 mV to +250 mV in these tests whereas MC3T3-E1 cells at -1000 mV to -400 mV were completely dead. There were statistically significant differences in the percent viable between the two cell types through the range of -500 mV to -1000 mV ($p < 0.05$) with decreasing viability as cathodic potentials increased. Above + 250 mV, again, and a statistically significant decrease in cell viability was observed ($p < 0.05$) for both cell types. The cell viability curve (Fig. 11) is similar to the one previously reported by Haeri et al.[45] in reference to MC3T3-E1 cells cultured on CoCrMo discs *in vitro*, with U937 cells surviving to larger cathodic bias. There were no significant differences ($p < 0.05$) in cells counted per 20X image between any two groups. The average number of cells counted per 20X magnified fluorescent image ranged from

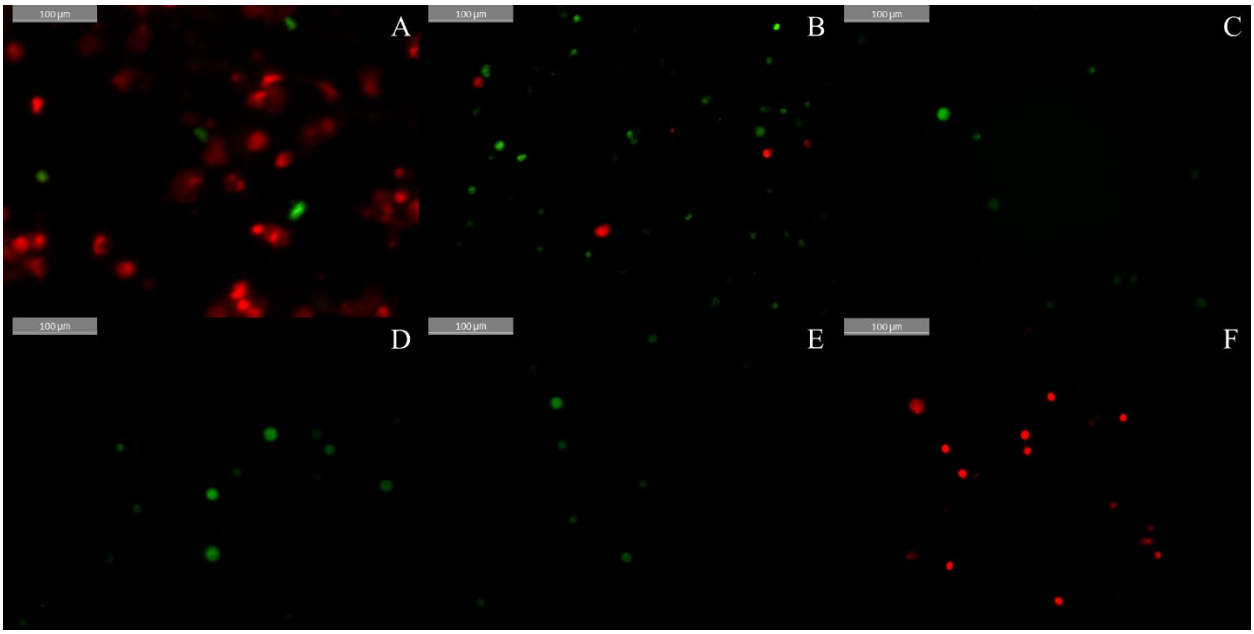

Figure 10: Live/dead images of U937 cells cultured on CoCrMo at (A) -1000 mV, (B) -750 mV, (C) -500 mV, (D) 0 mV, (E) 250 mV and (F) 500 mV for 24 hours *in vitro*. There were more cells in the anodic voltages (+250, +500 mV) when compared to the cathodic voltages

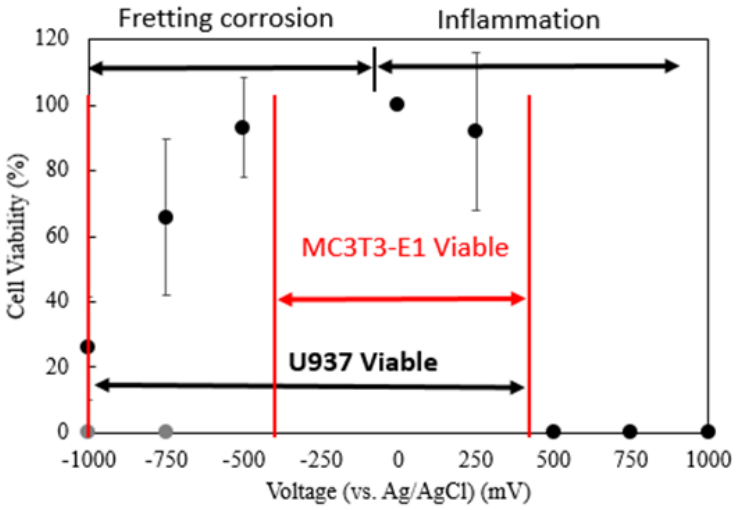

Figure 11: U937 and MC3T3-E1 cell viability cultured for 24 hours on the surface of CoCrMo disks at different voltages. U937 cells are shown with black circles and MC3T3-E1 cells are shown with grey circles

0.95 ± 0.6 (-500 mV) to 29 ± 26.4 (+1000 mV) with cell counts increasing with increasing cathodic and anodic potentials (away from OCP). Test groups between -500 mV and +250 mV ('90% zone of viability') resulted in the lowest cell count groups.

5.4.2. *Cell Size*

Average live cell size was at 0 mV (vs. Ag/AgCl) was 120.7 ± 56.2 μm² and was in the 65 μm to 103 μm range for the dead cells. There were no statistically significant differences in average cell size with potential (Fig. 12). The total number of cells analyzed per test group after PBS rinsing, fluorescent staining and image processing varied between 25 and 200 cells with the exception of -500 mV (n=7).

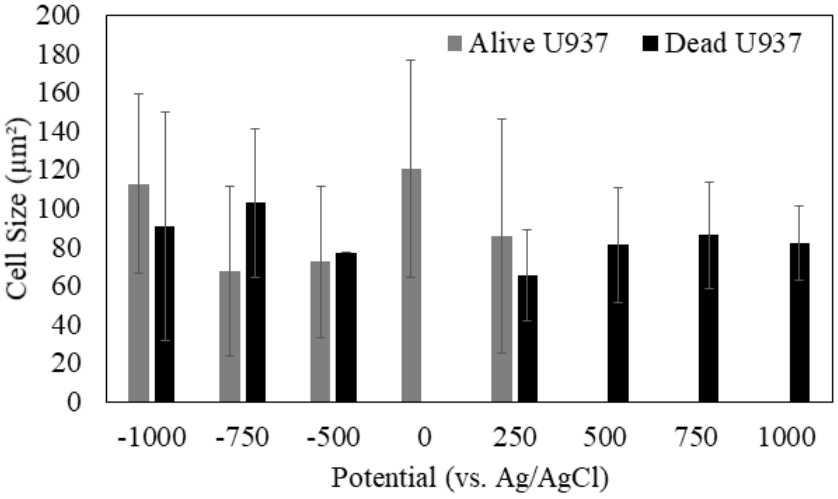

Figure 12: U937 cell size distributions of fluorescent stained images. Cells were separated into two groups, live and dead, and size was plotted as a function of voltage. There were no dead cells measured at 0 mV or alive cells measured above +250 mV

5.4.3. *Scanning Electron Microscopy Analysis*

Dead U937 cells at the lower limit (-1000 mV, Fig. 13A) exhibited evidence of extracellular remnants around central balled-up nuclei, consistent with apoptosis morphologies previously reported using this protocol[45]. This included fibrous remnants around a central cellular ball-like structure. U937 cells cultured between the potentials of – 500 mV and +250 mV remained 90% viable after potentiostatic trials for 24 hours. These cells appeared to have a round shape with no indications of cell migration, extensive apoptosis, fibrous perimeter, or degradation of the cell membrane on the CoCrMo surface in this potential range. The cell morphology at anodic voltages within the lethal range, > +250 mV, were disrupted with many of the cells exhibiting the appearance of spillage of the cellular content and the lack of visible cellular components including the nucleus, ECM and other vesicles.

5.5. Discussion

Shifts in electrode potential across metallic surfaces can arise from several different sources including abrasion of the oxide film[5, 112] or due to solution changes that can include the presence of ROS due to inflammatory cell-based responses[50]. Both anodic and cathodic potentials are feasible depending on the circumstances (highly tribocorrosive conditions vs. high inflammation). A zone of electrochemical viability has been defined within which cells remain viable and outside of which they will die over time. This work has shown that the electrochemical zone of viability is influenced by cell type, where U937 cells, emulating macrophage-like cells had a wider cathodic range of potentials under which they could remain viable than was observed previously for MC3T3-E1 preosteoblast-like cells[45]. For anodic potentials, both cell types exhibited cell death starting at about +350 mV (vs. Ag/AgCl) and were 100% dead by +500 mV.

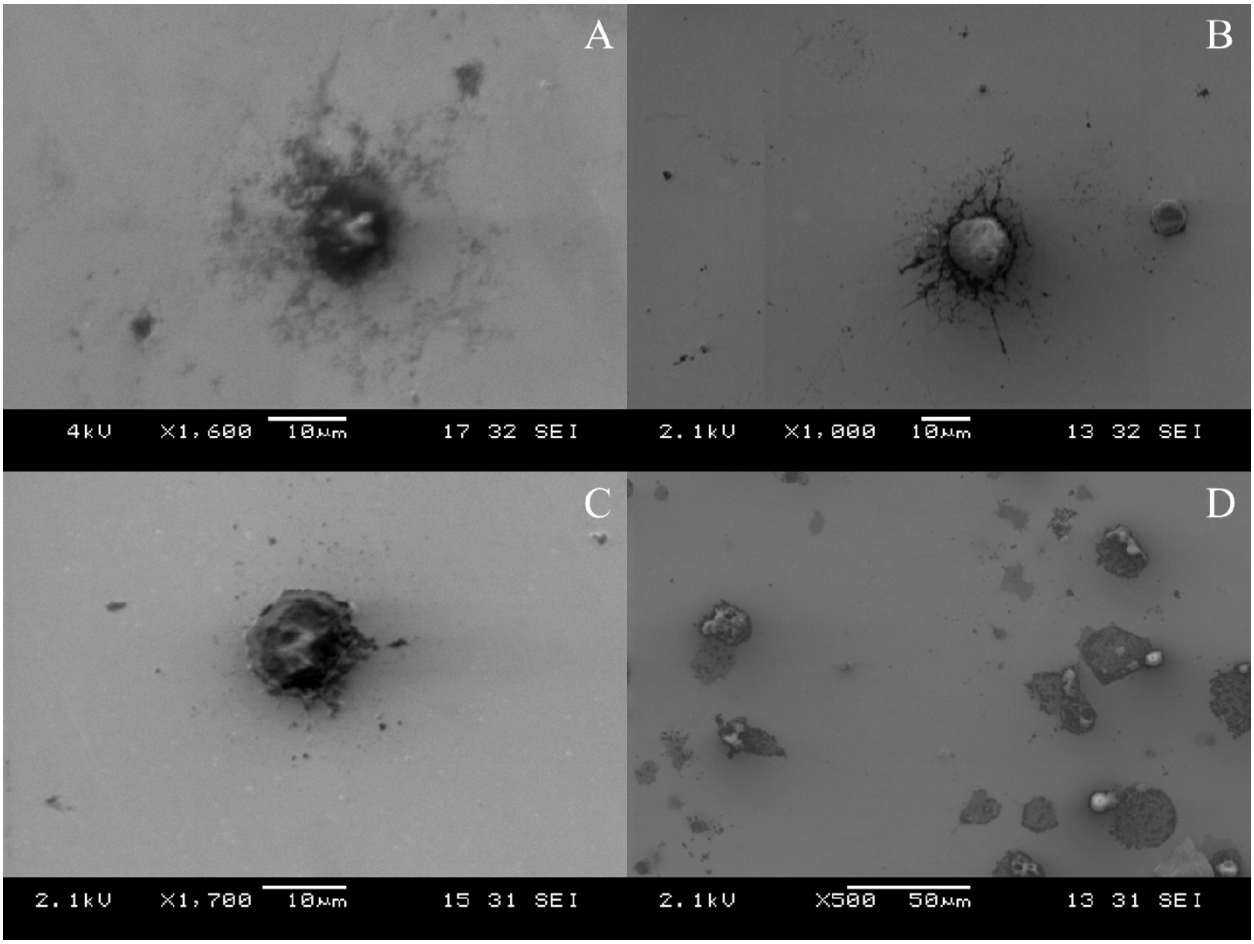

Figure 13: Scanning electron micrographs of U937 cells cultured on CoCrMo after 24 hours of polarization at (A) -1000 mV, (B) -500 mV, (C) 250 mV and (D) 500 mV *in vitro*. The dead cell in (A) appears to be balled up with a damaged cell membrane and cell components spread out in the near vicinity. The cells in the cathodic voltages (B, C) have a definitive shape, while the cells (D) appear to be damaged with evidence of extracellular remnants on the surface

The viability graph (Fig. 11) and SEM images (Fig. 13) show very different responses to cathodic vs. anodic voltages and the resulting U937 cellular structure after electrochemically-induced cell death. At the extreme cathodic voltages (i.e., -1000 mV), some U937 cells were still viable, but at a diminished percentage compared to behavior near OCP (± 250 mV) where > 90% viability was observed. Unlike MC3T3-E1 cells which exhibited a discrete fall in viability at -400 mV (vs. Ag/AgCl), there was a slower fall off in viability below -400 mV with retained

viability for some U937 cells even at -1000 mV (vs. Ag/AgCl). Cells within the electrochemical zone of viability reported higher size averages than those outside the range. These data (Fig. 11) suggest that the immune cells react differently to cathodic and anodic conditions where the dead cell morphology and cellular remnants are distinctly different in appearance with a more fibrous appearance around the cell perimeter at cathodic potentials and a more blotted appearance in the anodic images. These differences may reflect different modes of cell death taking place. This can also explain the number of cells present on the surface as a function of voltage. There were more cells imaged per area at the cathodic and anodic bounds of the test (-1000 mV, +750 mV and +1000 mV), with the fewest cell counts paralleling the highest viability groups. This would indicate that the dead cells outside the zone of viability were able to remain adhered to the surface with decreased surface area maybe playing a factor in adhesion. Perhaps the cells decreasing in size activates increased adhesion on the basal surface of the cell. Overall, there were more cells present on the surface during applied anodic potentials compared to cathodic potentials. It has previously been reported that reactive oxygen species and cathodic potentials affects cellular adhesion, specifically how the membrane proteins and actin are denatured[113, 114].

It is unclear, however, if the cells exhibit the same phenotype as they did at OCP. Phenotypic measures were not undertaken in this study, but changes in cell behavior may be inferred by the differences in the cell morphology on the metal surface. At these negative potentials, oxygen is being reduced at the surface and generating ROS (hydroxyl ions, singlet oxygen, super oxide anion, hydroxyl radicals, peroxyl radicals, alkoxyl radicals and hydrogen peroxide)[40, 115, 116]. High concentrations of ROS and low oxygen concentrations can alter cell behavior and damage internal organelles eventually leading to cell death[62, 117, 118]. Oxidative stress has been shown to alter cellular adhesion[113, 114], which could explain the low and variable

cell count at cathodic potentials when compared to anodic potentials. Cells in high cell density images were difficult to measure due to overlapping or weak RGB signals below the processing threshold. Also, several intact cells that were reported in our viability data did not filter successfully through our uniform rendering process for size measurements.

We hypothesize that there are defense mechanisms within U937 inflammatory-like cells that help maintain viability at extreme cathodic voltages. Common inflammatory cells (i.e. macrophages, hepatocytes) synthesize reduced glutathione (GSH) when stimulated by oxidative stress[119-122]. GSH is an antioxidant and functions as a ROS scavenger[63] protecting the cell from ROS-driven apoptotic processes such as reduction in cell growth, increased cell permeability and nuclear/internucleosomal DNA fragmentation[121]. GSH has been shown to protect macrophage (RAW 264.7) and monocyte macrophage-like (U937) cells from apoptosis induced by triptolide[123], 7-ketocholesterol[124], ceramide[80] and *tert*-butylhydroperoxide (*t*-BOOH)[125]. Ghibelli et al. reported GSH loss from cells before irreversible morphological changes in U937 cells before apoptosis[119] with GSH expulsion from the cell being one of the final stages in the apoptotic pathway in macrophage monocyte cells. By preserving viability of many of the key cellular components[126], GSH extrusion and intracellular oxidation[62] may explain the increased cathodic viability when compared to preosteoblast-like cells (Fig. 14).

Nitric oxide (NO) is another reactive chemical species (RCS) released by macrophage cells in inflammatory conditions[52, 127]. Lin et al.[16, 53] found that macrophages (TIB-71, RAW 264.7) stimulated to release nitric oxide (NO) enhanced the CoCrMo surface oxide layer through oxidation and nitration reactions. Maintaining the surface oxide at cathodic potentials due to NO production in addition to GSH extrusion may have contributed to the increase in U937 cell viability in the presence of ROS.

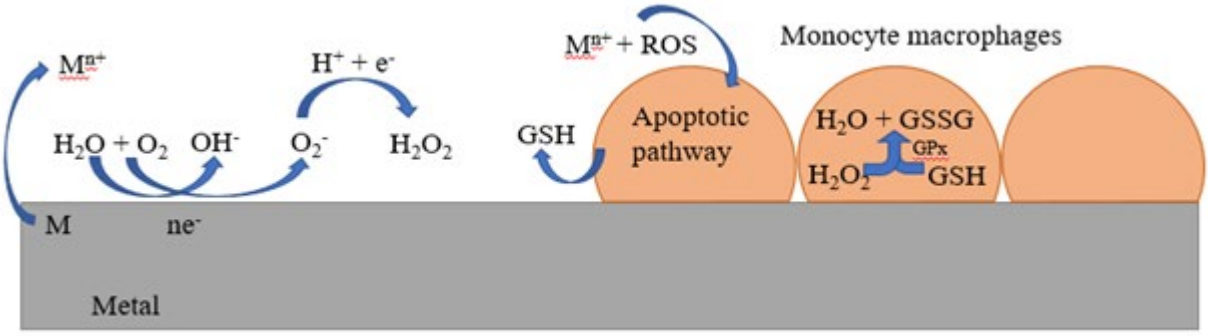

Figure 14: Schematic displaying the role of GSH during ROS production both within and outside the cell during polarization tests. GSH attacks hydrogen peroxide within the cell and is oxidized to its dimer and water. During the final stages of apoptosis, GSH is expelled through the cell membrane and then scavenges for nearby oxidative radicals

Fenton and Haber-Weiss reactions occur as a result of metal ion elution[26] from the surface and these processes can significantly damage cellular proteins, lipids and DNA[62]. Above +500 mV, Cr^{+3} ions are oxidized to Cr^{+6} ions which can readily be taken through cellular membrane anion transport systems[128]. When Cr^{+6} is metabolized within the cell, glutathione reductase (GR) activity is inhibited and GSH is oxidized to its dimer glutathione disulfide (GSSG) using glutathione peroxidase (GPx)[66]. While the cells expelling GSH are in the final stage of the apoptotic pathway, GSH functions as a scavenger to react with nearby ROS, decreasing the ROS concentration surrounding the nearby viable cells. We hypothesize that both

the synthesis of GSH within the cell and depletion across the cell membrane contributed to the added U937 resistance to cathodic polarization.

It should be noted that these cells were only tested for 24 hours and there might exist a narrower electrochemical zone of viability as time is increased, and vice versa for shorter test periods. It should also be stated that surface roughness was not measured but all samples were prepared and polished to the same mirror finish. The extent to which the surface is polished might play a role in adhesion and viability characteristics of the different cell types, and this work should be further characterized. Future work will include the characterization of intra- and extracellular GSH during cathodic and anodic polarization. This will give better insight into this proposed immune cell defense mechanism during ROS production along the alloy surface.

While the data presented here is a good indicator of cell activity with response to electrochemical stimuli, there are limitations to this work that would impact its physiological relevance. During active corrosion of the implant surface, several cell types are recruited (neutrophils, M1/M2 macrophages, etc.) with eventual foreign body giant cells developing at the site of inflammation. Constructing a complex model using these cells would not be feasible due to lack of material and survival rate of some of the cell types outside the human body. Our model displays that there is a difference in the electrochemical zone of viability between different cell types.

These results raise possible in vivo implications that merit further consideration. It is clear that mechanically assisted corrosion processes, whether within modular taper crevices or associated with any oxide film disruption process (e.g., fretting at screw-countersink interfaces, bear wear of metal surfaces, etc.) will result in associated drops in electrode potential of the implant. The amount of potential drop will depend on the severity of the abrasion-oxidation

processes and the area of the implant exposed to the environment. If these processes are sufficiently large, then the potential of the alloys may fall outside of the zone of viability for some cell types (e.g., osteoblasts) whereas other cells with an ability to defend themselves against these potential excursions, may be better protected. Whether such potential excursions play a role in clinically observed effects like adverse local tissue reactions associated with total hip replacements experiencing tribocorrosion processes is unknown, however, these results imply that such conditions may be possible. Sub-lethal exposure conditions may also modify cell phenotype and drive macrophages into specific reactive pathways. Such effects remain to be explored at this time.

Further studies should be conducted using other cell phenotypes in order to further quantify these observed cellular interactions. Voltage-induced cell death on metallic implants could be advantageous in designs of metallic biomedical devices and understanding cell-metal interface behaviors will further advance this area of research. Targeting the glutathione metabolic pathway could be the next step in suppressing ROS accumulation as well as other harmful radicals within and near inflammatory cells.

5.6. Conclusion

The electrochemical potential zone of viability for U937 cells, a monocyte macrophage-like cell, was shown to extend to more negative (cathodic) potentials compared to MC3T3-E1 cells but was the same for each at positive potentials. These results support our hypothesis that there are internal defense mechanisms responsible for monocyte macrophage-like inflammatory U937 cells' resistance to impressed cathodic voltages. Metallic biomaterials and medical devices can experience voltage excursions in both anodic and cathodic potential direction and these excursions have demonstrable effects on macrophage-like cell viability. Control of the surface

potential of metallic biomaterials relative to the zone of viability allows certain cells to remain viable while other cells can be killed. This approach may provide therapies that can monitor or affect the immune response to the metallic biomaterial.

6. Sensing localized surface corrosion damage of CoCrMo alloys and modular tapers of total hip retrievals using nearfield electrochemical impedance spectroscopy (NEIS)

Wiegand, MJ, Shenoy, AA, Littlejohn, SE, Gilbert, JL. 2019. Sensing localized surface corrosion damage of CoCrMo alloys and modular tapers of total hip retrievals using nearfield electrochemical impedance spectroscopy (NEIS). *ACS Biomaterials Science & Engineering* (In-Review).

Author names:

Michael J. Wiegand[a,b], Aarti A. Shenoy[a,b], Sara E. Littlejohn[a], Jeremy L. Gilbert[a,b,*]

Affiliations:

[a]Department of Bioengineering, Clemson University, Clemson, SC

[b]Clemson University-Medical University of South Carolina Program in Bioengineering, Charleston, SC

6.1. Abstract

Wear and corrosion damage of biomedical alloys alters the structure and electrochemical properties of the surface heterogeneously. It was hypothesized that local regions on the same surface systematically differ from one another in terms of their impedance characteristics. To test this hypothesis, CoCrMo discs exposed to electrosurgical and inflammatory-species driven damage were characterized using a novel impedance technique, nearfield electrochemical impedance spectroscopy (NEIS), to assess local surface integrity in response to applied damage. It was found that electrosurgical damage, as may arise during primary arthroplasty and revision surgeries, and hydrogen peroxide concentrations of 5-10 mM significantly alters the corrosion susceptibility of the local surface compared to the as-polished CoCrMo surface. A CoCrMo retrieved neck taper (Goldberg score of 4) was scored in different local regions relative to one another, and it was found that there is a direct relationship between increasing local relative Goldberg score and decreasing impedance, with the global surface impedance closest to the most severe-scored local region. This non-invasive method, which uses a milli-electrode configuration to test localized regions, can measure the heterogeneous electrochemical impedance of an implant surface, and specifically associate the response to damage mechanisms such as fretting corrosion, femoral cracking and intergranular corrosion.

Keywords: electrochemical impedance spectroscopy (EIS), CoCrMo, electrosurgery, inflammation, polarization resistance

6.2. Introduction

Biomedical alloys, including cobalt-chromium-molybdenum (CoCrMo) alloys used in total hip (THA) and total knee (TKA) arthroplasties, may experience a range of normal wear and tear initiated by several damage mechanisms during their use such as assembly forces during initial implantation[71] or cyclic fretting of two articulating surfaces within the prostheses[43]. Total hip replacements (THRs) have advanced in their materials since their initial conception with several alloys protected by a thin oxide layer that spontaneously forms on its surface[20, 53, 129, 130], and the most impactful design parameter has been the implementation of modularity. While the functionality and ease of use of modular junctions has increased mobility, cost effectiveness and has addressed patient-specific needs, the additional interfaces of modular junctions may increase the need for revision surgeries and replacements among THRs.

Modular junctions are subjected to mechanically assisted crevice corrosion (MACC) where metal ions, oxides and tribocorrosion debris are released from the alloy surface[40, 48, 50, 76]. Recently, it has been shown that the addition of molybdenum (Mo) within CoCrMo alloy may reduce the effect of wear loss compared to commercially pure CoCr alloy[131], however CoCrMo devices are more susceptible to the effects of MACC due to microstructure[132] and detachment of the metal carbides during wear[133]. These damage processes are thought to be associated with immune and inflammatory responses, often referred to as an adverse local tissue reaction (ALTR)[12, 14, 24].

During wear, the passivity of the surface is dependent on the electrochemical properties of the passive oxide film[134] with surface potentials dropping as low as -900 mV (vs. SCE) during disruption of the oxide film[43]. In addition, potential drops of this sort significantly increase

reduction reactions present at metal surfaces which includes increasing the generation of reactive oxygen intermediates (ROIs) directly at the implant surface[135]. These reduction products have been shown to induce killing of cells in proximity to the metal surface[42, 45]. Immediately following this potential drop, biological material[31] including immune cells, foreign body giant cells (FBGCs), host tissue, reactive oxygen species (ROS) and dysregulated enzymes can penetrate and attack crevices which then furthers the breakdown of the implant surface as well as the loosening of the joint prostheses[17, 70]. Corrosion of this nature may facilitate other responses from the surface such as intergranular corrosion and fatigue crack nucleation, ultimately leading to the failure of the implant, however these links have not yet been demonstrated.

In addition to mechanical, electrochemical and biological-based damage, implant surfaces can also be exposed to electrical-based injury as a result of electrocauterization techniques. Previous reports of inflammatory cell-induced (ICI) corrosion[14] noted pitting features with trail-like evidence of cellular artifacts on metal surfaces, however many of these topographies have since been reproduced using electrocautery[72, 136].

During surgery, clinicians must cauterize local blood vessels to minimize bleeding and achieve hemostasis. However, the electrical energy from electrocautery can propagate plasma arcs from the electrosurgical pencil to the metal surface, resulting in localized flash melting and plasma-field induced wave-like pitting[72] of metal implant surfaces. Electrosurgical generators can achieve potentials up to 5 kV with frequencies of 500 kHz[72]. When the plasma arc is transmitted from the pencil to the surface, wave-like surface defects resulting from localized melting are created and cause a drop in the overall corrosion resistance of the metal by decreasing the impedance and altering the oxide film[137]. Electrosurgical damage has also been

documented to travel through up to 3 mm of simulated tissue, making it very feasible that multiple electrosurgical melted pits are generated during surgery without the pencil ever making physical contact with the surface. It has been hypothesized that these contact points could lead to an accumulation of stress within the surface layers, eventually leading to femoral cracking of the implant with future full mechanical failure[72, 136].

One of the greatest challenges surrounding orthopaedic alloys is assessing levels of damage and documenting sources of implant failure. There are certain types of wear and corrosion mechanisms closely associated with failure of implants including aseptic loosening, crack propagation within the neck or stem, or tribocorrosion debris generation. However, there is no single diagnostic method which can easily quantify the extent of damage outside of a visual subjective inspection by the surgeon. Two questions that are becoming more relevant during implant assessment are 1) is there an *in situ* diagnostic measurement method that can quantitatively assess the integrity of implant surfaces?, and 2) can such a method be applied in real-time during surgery without compromising the safety of the patient?

One approach, considered here, is to utilize EIS methods on a nearfield basis where only a small region of the surface is analyzed for its impedance properties (resistive and capacitive character). EIS typically investigates large areas of an electrode where a wide range of surface structures and properties may be present, and a surface area averaged response will be obtained[40, 42, 48, 138-143]. In addition, for evaluation of orthopaedic implants, EIS is generally an *ex vivo* practice with limited capability for in situ evaluation.

We hypothesized that if we can control the working electrode area by limiting the cell geometry to fit inside a standard pipette tip, we could record local EIS spectra wherever we

choose on the surface such as a severely corroded point on an otherwise undamaged surface. This would allow us to compare site-specific electrochemical properties to that of the entire system. Therefore, the goals of this study were to expose CoCrMo surfaces to various known and characterized types of damage and to use nearfield electrochemical impedance spectroscopy (NEIS) to characterize localized impedance responses. CoCrMo retrievals were assessed for damage and the NEIS techniques were used to correlate Goldberg score and corrosion type with electrochemical behavior. Non-destructive evaluation (NDE) techniques of implant surfaces may advance our knowledge of corrosion mechanisms within the human body, specifically how different damage modes contribute to the overall failure of a device.

6.3. Materials and Methods

6.3.1. Sample Preparation

High-carbon CoCrMo alloy discs (ASTM F-1537) were polished up to 1.0 µm alumina until a mirror finish, rinsed with deionized water, sonicated with 70% ethyl alcohol for 30 minutes and dried using nitrogen before electrocautery and inflammatory species-induced damage. The surface was damaged using the electrosurgical generator and pencil with the disc placed on a Macrolyte^{TM} dispersive pad to complete the circuit (Conmed System 2450, Conmed, Utica, NY). Standard coagulation mode at power 50 was used to produce all electrosurgical damage with the pencil lowered until close proximity but not touching (< 1 mm) at each location for less than a second, producing plasma arcs as a result of circuit activation. The polished as-is CoCrMo surface served as the control group. The four groups tested (Fig. 15A) were adapted from ones previously explored[72], where electrosurgical damage was induced on a 1) dry surface, 2) a phosphate buffered saline (PBS)-wetted surface, and through 3) 1 mm and 4) 3 mm of PBS-

soaked agar. The varying thicknesses of agar mimicked local tissue and the PBS group mimicked blood likely present during primary and revision arthroplasty procedures. CoCrMo surfaces were cleaned and dried of PBS and agar remnants prior to NEIS measurements.

The inflammatory test disc was assembled by gluing a Teflon chamber with 3-openings to the surface. Each opening was then filled with deionized water containing a varying level of hydrogen peroxide (H_2O_2) (1, 5, 10 mM) and then sealed with Parafilm (Bemic Company, Neenah, WI) at room temperature. Solutions were replaced with newly prepared solutions every 7 days to account for potential dissolution or degradation of H_2O_2 in solution. Teflon discs were carefully pulled away from the surface following 21 days and NEIS was performed on the test locations. The polished as-is surface not exposed to solution served as the control group.

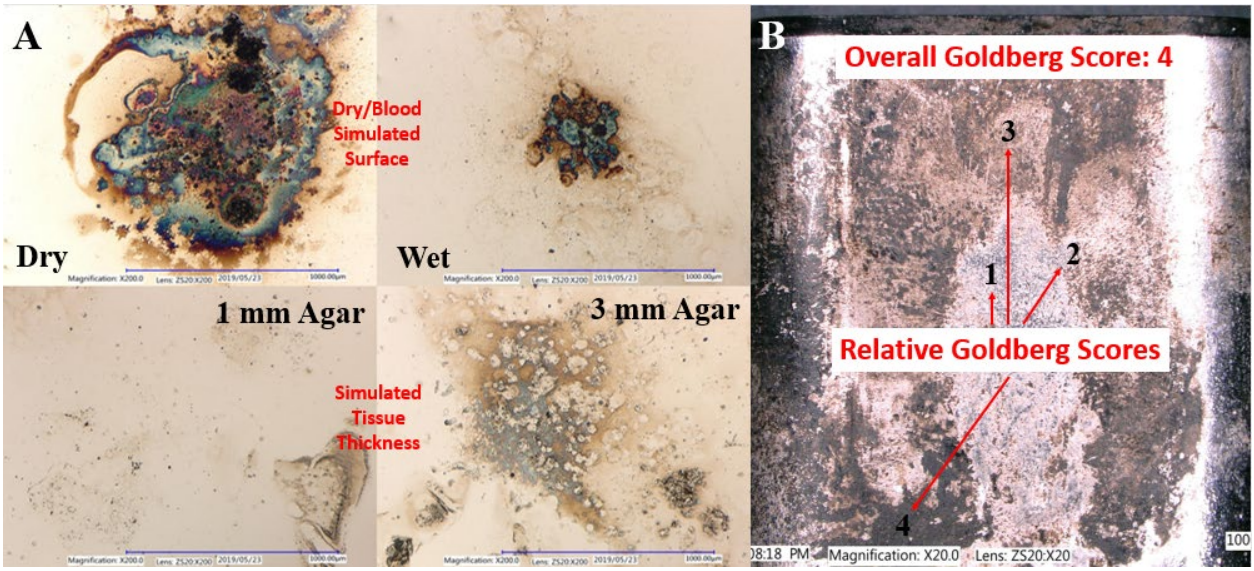

Figure 15: CoCrMo electrosurgical damage discs (A) and neck taper retrieval (B). Taper retrieval base around where local Goldberg score NEIS measurements were recorded

A retrieved CoCrMo neck taper with an overall Goldberg score of 4 (severe corrosion, Fig. 15b) was tested in four locations within the neck taper region. The Goldberg scoring system (GB 1-GB 4) in brief is as follows[144]: no visible signs of corrosion (GB 1), less than 30 percent

of the area is discolored (GB 2), greater than 30 percent of the area is discolored or less than 10 percent of the area is black material, etched or pits (GB 3), and greater than 10 percent of the area is covered with black material, etches or pits (GB 4). The neck taper surface was scored locally in four areas all relative to one another for corrosion and electrochemically analyzed using NEIS. Therefore, the relative score of 1 (Rel. GB 1) is not a true Goldberg score of 1, it is however the least corroded area on the surface in comparison to the other sites measured (Rel. GB 2-Rel. GB 4). The neck taper region was also measured as a whole and referred to as the global surface (GS) in the results and discussion.

6.3.2. Electrochemical Experiments

Previously-developed techniques[145] were used to define the NEIS protocol. Briefly (Appendix C.1), a PBS-filled pipette tip with an area of 1.96×10^{-3} cm^2 (I.D. = 0.5 mm) was placed flush against the CoCrMo surface (Fig. 16) to prevent PBS leakage onto the surface and limited the working electrode area to that of the pipette tip opening. Counter and reference electrodes were inserted through holes along the side of the tip where platinum (Pt) and chlorided-silver wire (Ag/AgCl) served as the counter and reference electrodes, respectively. The top of the pipette tip was then covered with Parafilm to create a partial-vacuum seal. Previous reports[146]

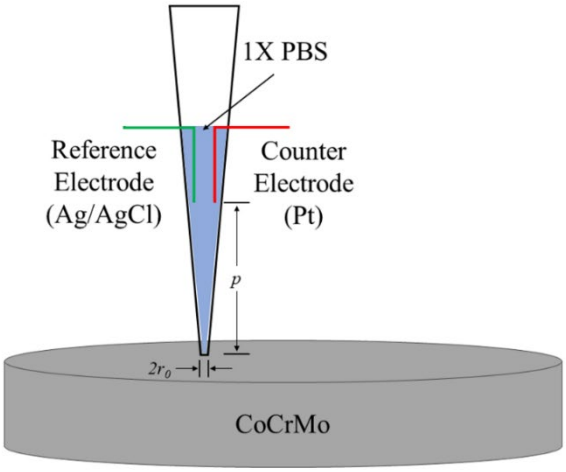

Figure 16: Test set-up used in all nearfield electrochemical impedance spectroscopy (NEIS) measurements

regarding cell geometry determined that the counter and reference electrode tips be placed a minimum dimensionless distance of 2P from the working disk electrode where $P = \frac{p}{r_o}$, (p = distance between the reference or counter electrode tip and working electrode, r_o = radius of working electrode area). This distance was found to eliminate frequency dispersion in the local impedance response and support steady-state calculations[147]. The tip recorded open circuit potential (OCP) for all test groups for 30 mins, allowing for potential stabilization prior to NEIS across a frequency range of 20,000 to 0.01 Hz. Impedance magnitude (|Z|) at the lowest frequency recorded (0.01 Hz) was used for assessing impedance differences and all other electrochemical properties including constant phase element (CPE) capacitance response (Q) and CPE exponent (α) were fit to the most appropriate model made up of resistors and constant phase elements using a non-linear least squares fitting program in ZView (Scribner, Southern Pines, NC).

6.3.3. High Magnification Microscopy

Following NEIS, different modes of corrosion and surface damage were identified and captured for the experimental groups (electrocautery, retrieval) using digital optical microscopy (DOM, Keyence VHX-6000, Japan) and scanning electron microscopy (SEM, Hitachi S-3700N, Japan). DOM and SEM images were taken at the exact points of NEIS measurements for comparison with NEIS spectra.

6.3.4. *Statistical Analysis*

All experiments and techniques were repeated in triplicate. Averages and standard deviations were calculated and one-way ANOVA and Tukey's *post hoc* pairwise comparison

with simple effect was performed to assess statistically significant differences between groups. A 95% confidence interval ($p < 0.05$) was taken to be significantly different.

6.4. Results

6.4.1. Electrochemical Experiments

Open circuit potential (OCP) was measured for 30 mins prior to NEIS measurements for all samples and test groups (Fig. 17). OCP (mV) was significantly ($p < 0.05$) higher for all test groups when compared to the as-polished CoCrMo control surface. Per sample, the dry condition, 10 mM H_2O_2, and global surface had the greatest effect on OCP for the electrosurgical disc, H_2O_2 treated disc, and CoCrMo neck taper retrieval, respectively.

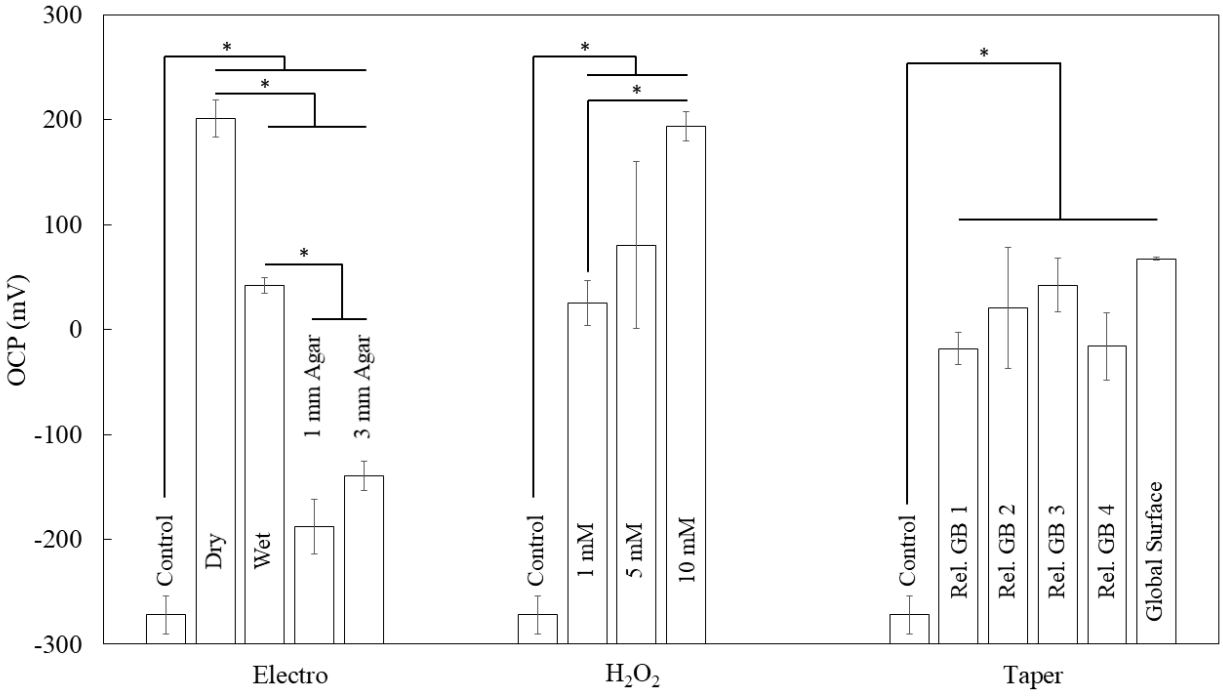

Figure 17: NEIS measurements (n=3) of open circuit potential (OCP). All test groups were significantly higher ($p < 0.05$) in OCP (mV) when compared to the as-polished control CoCrMo surface, indicating a change in surface electrochemical characteristics following damage conditions. Brackets indicate multiple groups with significantly different OCP

Impedance magnitude (|Z|) and phase angle (θ) were recorded and plotted against log of the frequency (Hz) for all samples and test groups (Fig. 18-23). |Z| was significantly decreased ($p < 0.05$) compared to control for all electrocautery (Fig. 18A) and surfaces treated with 5 and 10 mM H_2O_2 relative to PBS (Fig. 18C). There appeared to be a strong correlation between decreasing |Z| and increasing concentrations of H_2O_2 as well as conditioned electrocautery surfaces (Wet, 1mm Agar, 3mm Agar). The dry contact region on the electrocautery disc was significantly lower in |Z| than all other groups and an order of magnitude lower than the control group. It should be noted that the jump in |Z| below 1 Hz in several impedance plots is an artifact of the EIS system that appeared in some, but not all scans.

Phase angle (θ) plots (Fig. 18B, 18D) were able to reveal the electrochemical state of the surface, with some groups fit to a constant phase element (CPE) Randles circuit and others fit to one of two coated models as opposed to the standard Randles circuit (control). The presence of a shifted rise in the high frequency domain (5 mM, 10 mM), multiple peaks (Dry), or delayed decrease in phase angle (Wet, 3 mm Agar) when compared to the control indicates that the surface response behaves like a coated model.

The Bode plot responses for the retrieval groups displayed the largest coated model behavior and direct correlations between increasing levels of damage and impedance characteristics (Fig. 19-22). SEM micrographs of each Relative Goldberg score were placed adjacent to the Bode plots to better visualize the impedance curves. All of the Relative Goldberg score groups (Rel. GB 1-4) displayed a bimodal peak within the phase angle plot with peaks aligned with inflection points in the |Z| vs. frequency plot. This response is revealing of a coated model behavior, with the response appearing to be more pronounced with increasing Relative

Goldberg score associated with greater amounts of corrosion debris present. The global surface (GS) Bode plots (Fig. 23) are a holistic electrochemical response with the behavior alike to the most severely corroded region (Rel. GB 4). It appears the GS phase angle response has one peak with the overall magnitude and shape of the curve like that of a coated model.

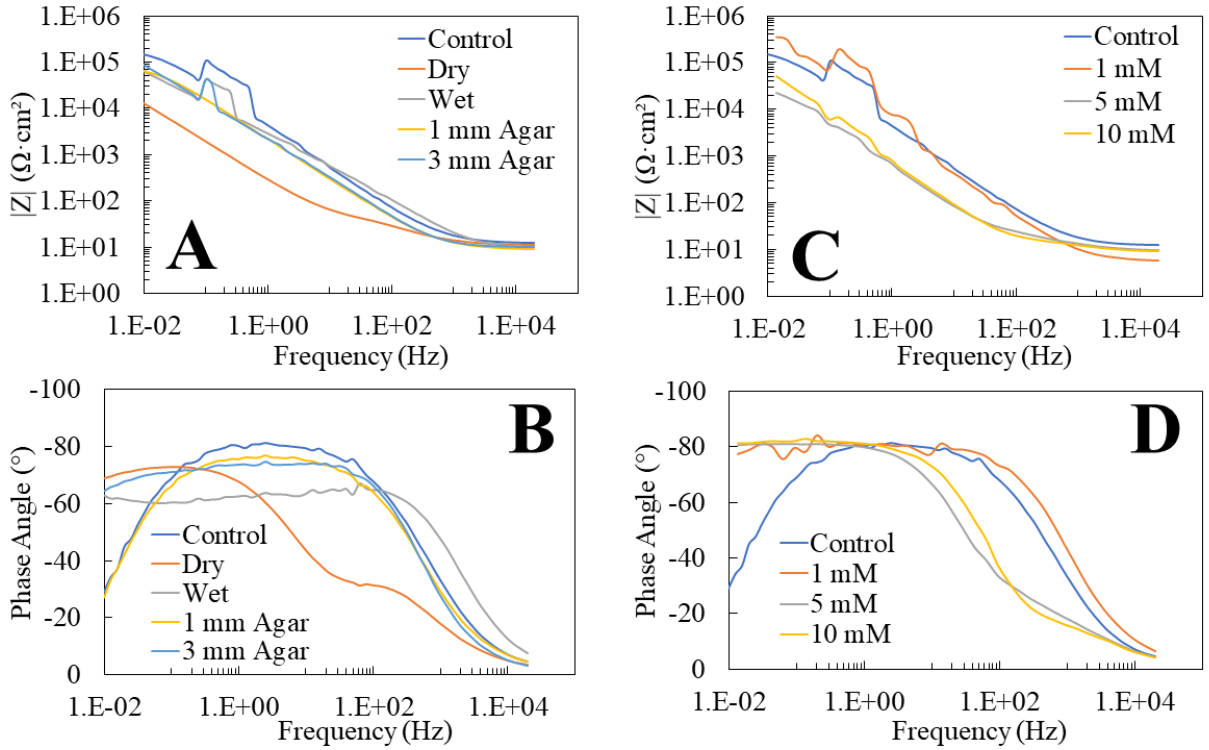

Figure 18: Impedance magnitude (|Z|) (Ω·cm^2) and phase angle (θ) plotted against frequency (Hz) of the electrosurgical damaged CoCrMo disc (A, B) and hydrogen peroxide treated disc (C, D). Each line represents one continuous measurement across the frequency range, and the 'hitches' in the |Z| plots between 1E-02 and 1 Hz are gain delays within the software (ZView). These plots (A, C) display the differences in impedance magnitude, specifically in the lower frequencies that are representative of the sum of the solution and polarization resistances (R_S, R_P). The phase angle plots (B, D) display noticeable changes in rise of the phase angle in the higher frequencies, as well as the presence of multiple peaks, indicating multiple time constants and states of the surface/oxide film. These changes also align with the |Z| plots, where the inflection point of the impedance curve matches up with the inflection point of the phase angle at the same frequency

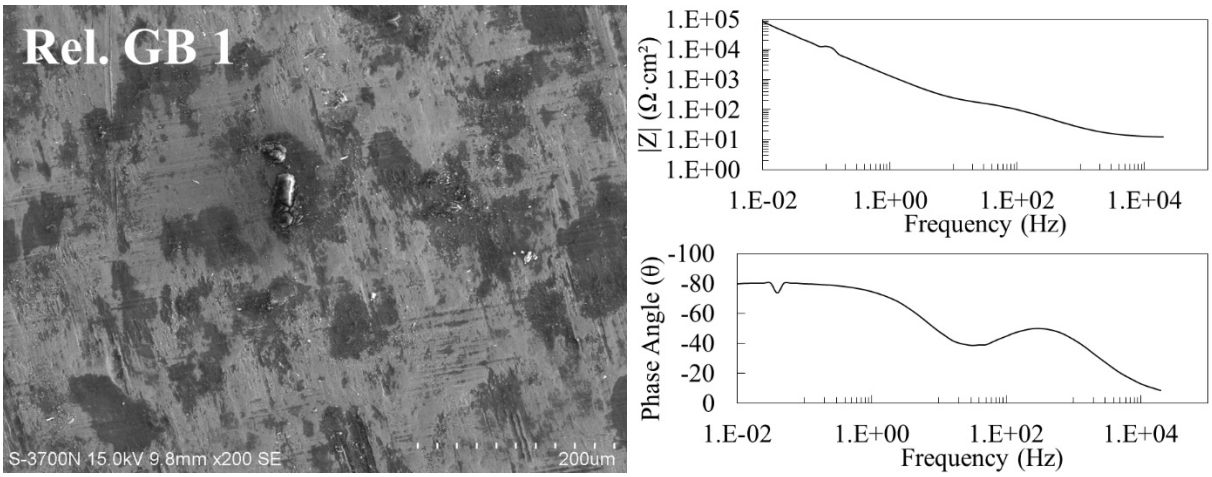

Figure 19: Scanning electron micrograph taken in secondary (SE) with corresponding Bode impedance magnitude (|Z|) and phase angle (θ) plots of Relative Goldberg 1 test location. The micrograph displays evidence of perpendicular machining marks with minimal debris on the surface. The phase angle plot displays two peaks that align with the inflection points in the impedance magnitude plot, representative of a coated model with two separate CPE exponent constants

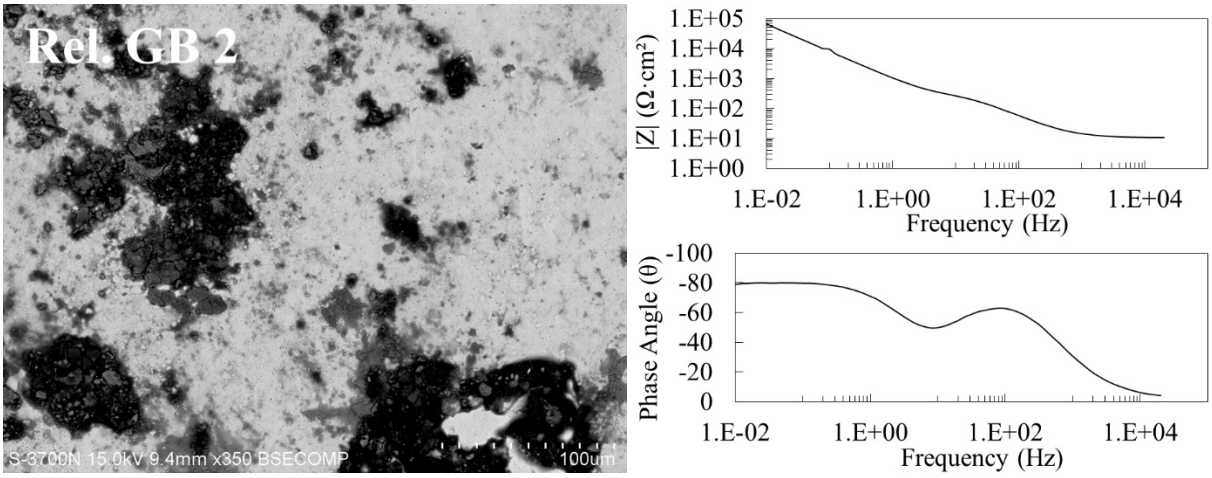

Figure 20: Scanning electron micrograph taken in backscatter (BS) mode with corresponding Bode impedance magnitude (|Z|) and phase angle (θ) plots of Relative Goldberg 2 test location. The heterogeneity of the surface is clearly displayed by the dispersed black carbonaceous material and grey oxides atop the bright metallic surface. The phase angle has a more prominent high frequency peak when compared to the Rel. GB 1 location, with a decreased overall |Z|

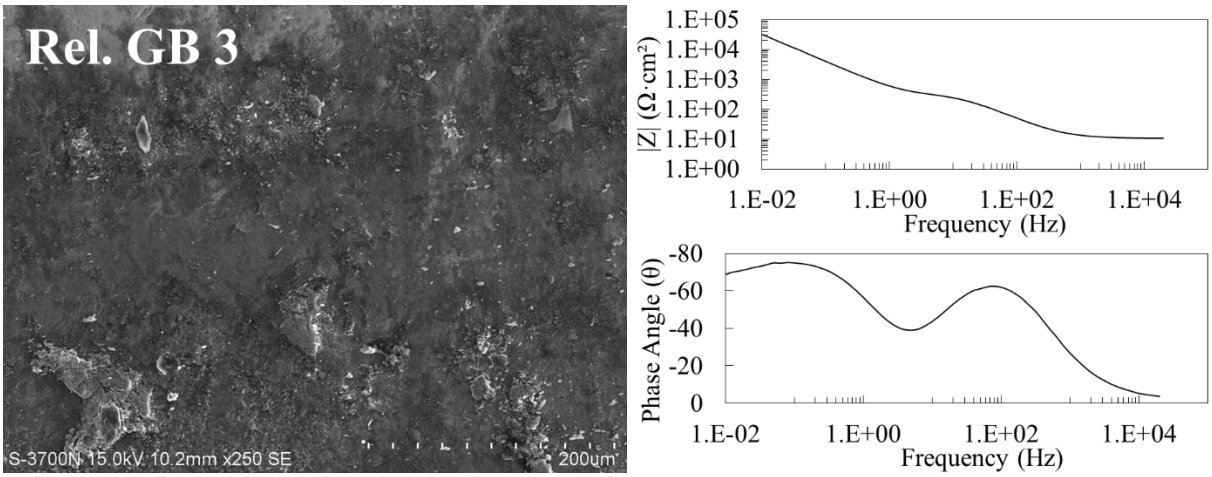

Figure 21: Scanning electron micrograph taken in secondary (SE) with corresponding Bode impedance magnitude (|Z|) and phase angle (θ) plots of Relative Goldberg 3 test location. This location has more debris of varying sizes than the less severe test groups, with differences in the oxide topography in the micrograph. The phase angle plot bimodal peaks are more distinct than the Rel. GB 1-2 locations, in addition to a lower |Z| response. This is reflective of a more coated response with decreased resistive properties

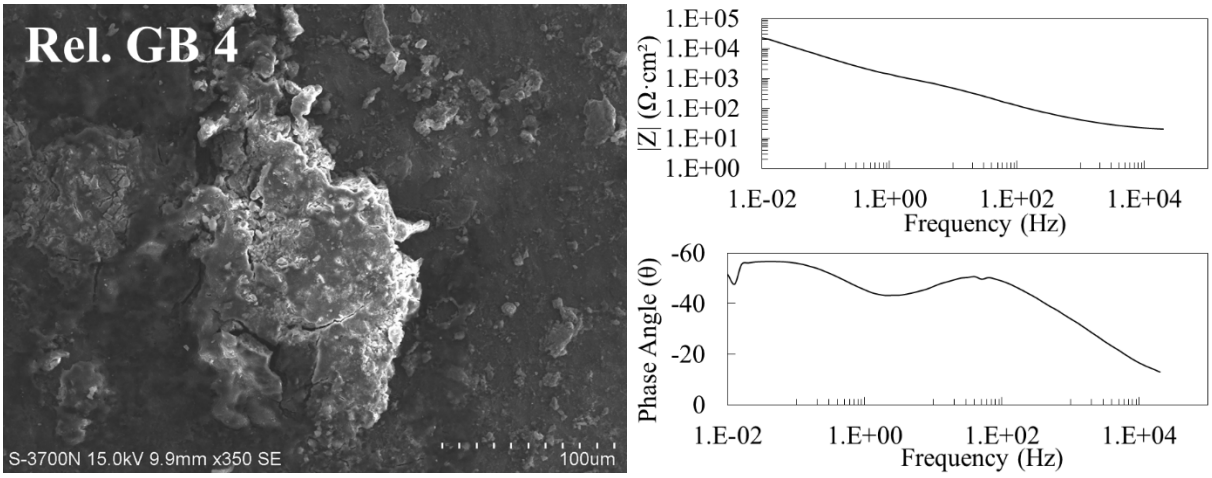

Figure 22: Scanning electron micrograph taken in secondary (SE) with corresponding Bode impedance magnitude (|Z|) and phase angle (θ) plots of Relative Goldberg 4 test location. The severity of the corrosion can be seen in the micrograph, where the highlighted oxide/debris is dispersed across the surface with large pieces of the oxide decayed in appearance. The phase angle and |Z| plots are similar to previous test groups, with a bimodal phase angle response and two inflections points in the |Z| curve. The phase angle and |Z| curves are both lower in magnitude than the other test groups, signifying the greatest effect on the resistive properties of the CoCrMo surface

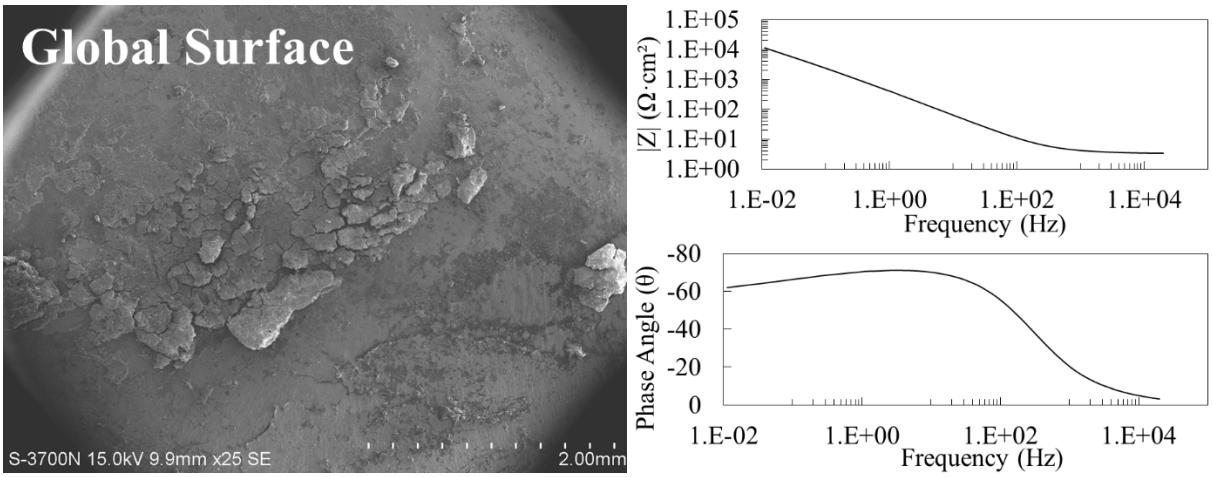

Figure 23: Scanning electron micrograph taken in secondary (SE) with corresponding Bode impedance magnitude (|Z|) and phase angle (θ) plots of the global surface in low magnification. The difference in oxide film build-up, debris, machining marks and visible bare metal all contribute to a 'smearing' effect in the electrochemical responses, where the phase angle plot has one large distorted peak with a delayed decrease in intensity. The |Z| response has only one inflection point to match up with the phase angle, and the data taken from this response are most closely associated with the most severely corroded location (See Discussion, 6.6)

CPE exponent (α), capacitance (Q) and impedance magnitude (|Z|) were measured and calculated using the non-linear least squares fitting algorithm within the impedance software (ZView) and the log of Q was plotted against the log of |Z| at 0.01 Hz (Fig. 24). α is a measure than relates to the non-ideal behavior of the CPE, where the closer α is to 1, the more the CPE behaves like a true capacitor. |Z| at 0.01 Hz was taken to be representative of the impedance of the surface, as opposed to the polarization resistance (R_P) of the surface, due to the fact that the low-frequency plateau in the |Z| vs. frequency plots (Fig. 18-23) was not fully captured within the frequency range (20,000-0.01 Hz). The algorithm in the software extrapolates the |Z| response to an estimated R_P value. Hence, we used |Z| at 0.01 Hz to better explain shifts in behavior using recorded data at a uniform frequency, rather than estimated/extrapolated results.

There were no observable trends between levels of retrieval damage or electrocautery damage conditions and CPE exponent (Fig. 24A). Higher concentrations (5 mM, 10 mM) of the inflammatory-species resulted in lower CPE exponents. The wet surface had a significantly lower ($p < 0.05$) α than all other electrocautery test groups and the 1 mM H_2O_2 group had a significantly higher α than all other H_2O_2 groups, indicating that the wet surface and higher inflammatory-species concentrations lead to more of a non-ideal behavior.

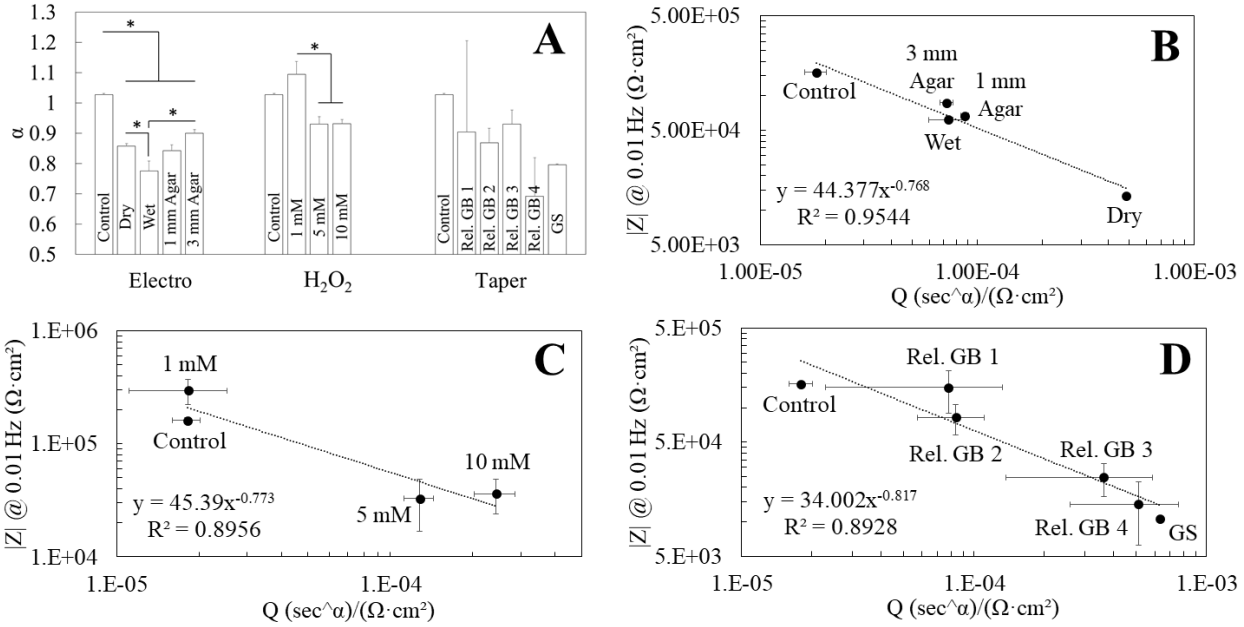

Figure 24: Constant phase element (CPE) exponent (A) and Q vs. |Z| (B-D) from CPE Randles and coated model non-linear least squares algorithm fit (ZView) of test groups. Exponent (α) group averages that are significantly different ($p < 0.05$, *) from the other sample sets are indicated. It should be noted that α for the control and 1 mM H_2O_2 groups are above 1, which is not possible, however the fitting algorithm can return such values and this is taken into consideration during analysis. CPE capacitance (Q) is plotted against impedance magnitude (|Z|) at 0.01 Hz of the electrosurgical damaged CoCrMo disc (B), hydrogen peroxide treated disc (C) and severely corroded CoCrMo neck taper (D). The samples treated with the highest concentrations of H_2O_2 and the most corroded retrieval surfaces (Rel. GB 4, GS) displayed the largest decrease in α.There are strong correlations between decreasing |Z| and increasing Q, where increasing the Q shifts the high frequency domain of impedance values towards the lower frequencies, thus decreasing the |Z| value

CPE Q significantly increased and the |Z| decreased for all electrocautery and retrieval experimental groups (Fig. 24B, 24D), and for the 5 mM and 10 mM H_2O_2 test groups (Fig. 24C) when compared to the control surface ($p < 0.05$). There existed a strong inverse correlation between the two variables with calculated measures of fit confirming this observed trend (R^2 = 0.9544 for electrocautery, R^2 = 0.8956 for H_2O_2, R^2 = 0.8928 for retrieval). This behavior is due to when the Q increases, it shifts the transition point between resistive and capacitive response towards lower frequencies (left shift in the Bode plots, Fig. 18), which directly results in a decrease in |Z| at 0.01 Hz. This electrochemical phenomenon is most prominently seen in the dry contact test group with a significantly higher Q and lower |Z| than all other electrocautery test groups and the control (see Fig. 24B).

6.4.2. High Magnification Microscopy

Scanning electron micrographs of the electrocautery disc (Fig. 25) and severely corroded taper (Fig. 19-23) were taken in both secondary and backscatter modes at the sites of NEIS measurements. The surface topographies following electrocautery induced damage were consistent with what has been previously reported[72], with appearances of flash melting, wave-like features around a centralized pit with balled-up metal debris. The wet and agar-treated surfaces appeared to result in less microscopically apparent damage than the dry condition, indicating that the resistance and barrier provided by the PBS or agar limited the electrocautery induced damage.

Microscopic observations of the retrieved neck taper surface show nominal differences in the differently scored regions, which forms an interface with the stem taper, and, therefore, experiences assembly and subsequent fretting corrosion damage. Scanning electron microscopy (SEM) shows further evidence of micro-scale differences within the Relative GB scores from 1-4 (Fig. 19-22). Assembly scratches are seen at the distal edge of the taper, which are longer in length and do not have parallel scars which is a feature of fretting damage. The central, Rel. GB

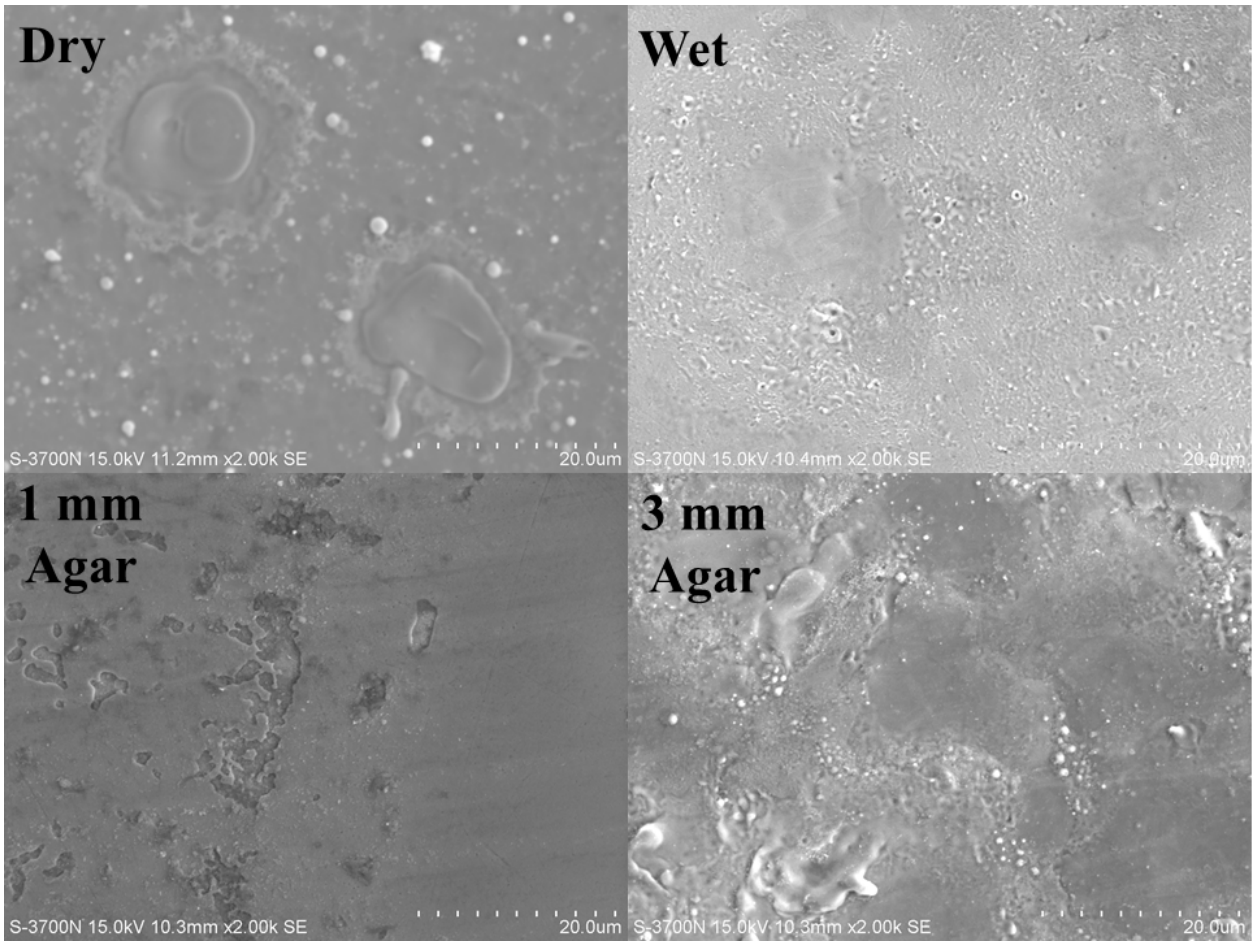

Figure 25: Scanning electron micrographs taken in secondary (SE) at 2,000X magnification of the four different test conditions on the electrosurgical damaged CoCrMo disc. Micrographs are similar to previous reports of electrosurgical damage[72] with localized melting and surface deposits, characterized by central pits and fluttering features. The four damage conditions appear to present different surface morphologies and states, agreeing with the unique spectra obtained during NEIS measurements

1 region (Fig. 19) shows more fretting type damage, with parallel scarring and shorter lengths (< 100 μm). In backscatter mode, dark deposits (carbon-rich, confirmed by energy dispersive x-ray spectroscopy (EDS)) and intermediate contrast (oxide-based) deposits are seen in region 2 (Rel. GB 2, Fig. 19) which act as a coating on the original taper surface. Rel. GB 3-4 (Fig. 21-22, respectively) demonstrate more extensive damage, with the underlying microstructure revealed in some parts and a larger surface area covered by similar deposits as Rel. GB 2. The various states of the retrieval surface can further explain the differences in NEIS spectra, indicating that there might be specific conditions and materials that influence and bias impedance characteristics.

6.5. Discussion

In furthering our understanding of how different damage modes might affect electrochemical performance of CoCrMo surfaces, the NEIS technique offers some useful context to visual observations. The presence of an asymmetrical phase angle plot or a change in slope in the |Z| plot is an indication of the surface's deviation from ideal or CPE Randles circuit (Fig. 18-23). Multiple peaks in the coated model correspond with multiple Randles-CPE elements (i.e., coated model) and two distinct states of the surface, usually build-up of debris in the high frequency domain and the thin native oxide film in the low frequency domain.

Electrosurgery damage is characterized by flash-melting local areas where the plasma arc makes contact with the alloy surface (Fig. 25). Oxide defects are therefore a consequence, however the addition of material (PBS and/or agar, to mimic blood and tissue) forms a semi-protective coating on the surface, which is corroborated by the impedance and phase angle plots in Figure 18B-C. Except for the 1 mm agar gel condition (CPE Randles), all three conditions

(Dry, Wet, 3 mm Agar) seem to exhibit a coated model-like impedance behavior. It is unclear at this time why the thinner agar test group (1 mm) appears to be less damaged (Fig. 25) with decreased electrochemical characteristics when compared to the thicker group (3 mm) with more prominent indications of surface damage.

Regions of the disc exposed to different concentrations of H_2O_2 exhibited closer to a CPE Randles type behavior, as seen in Figures 18C-D. This is to be expected since hydrogen peroxide did not microscopically alter the passivating oxide film (based on SEM imaging analysis) on the disc surface, nor did it form a film or coating of any sort (images not shown).

The retrieved neck taper demonstrates the benefits of this approach most explicitly. All four Relative Goldberg score regions exhibit a coated model behavior, even though physical deposits are only seen in Rel. GB 2-4 (Fig. 20-22). Rel. GB 1 region still shows oxide defects, and formation of irregular features on the surface, which can induce local capacitive or resistive characteristics, thereby altering the overall impedance characteristics of the surface. Overall, the use of imaging techniques and nearfield impedance measurements can be useful in describing the nature of the surface and its corrosion resistance properties. The electrochemical characteristics (OCP, |Z|, Q) of the retrieval global surface (GS) (A = 0.110 cm^2) were measured or calculated and most closely associated with the locally scored region of 4. This is due to the fact that the overall |Z| of the surface is determined by the integral over the area of the reciprocal of |Z| i.e. the lowest |Z| regions will bias and shift the signal towards the most severely damaged regions. OCP and Q were highest in the GS compared to all other test groups, and the GS had the lowest measured |Z| for the retrieval group.

It was the goal of this study to develop reproducible protocols that could capture key electrochemical-surface properties in a location-specific manner and assist in the subjective retrieval assessment, i.e. Goldberg scoring system. Our data agrees with previous studies on the heterogeneities that exist on metallic biomaterial surfaces. For example, CoCr wallstent wires have reported nonuniform electrochemical properties, such as interfacial resistance and capacitance[148], where significant changes in impedance values were associated with premature fracture of the wallstent. Indira and Nishimura[149] similarly observed an impedance drop over scratched Cr-steel surfaces compared to the unabraded areas, with increasing chromium content resulting in higher impedance values and increased corrosion resistance in oxidized scratched-locations. It was also reported that chloride ions and oxygen molecules, serving as reactive species during reduction, accelerated the corrosion process based on EDS spectra of the corroded Cr-steel surfaces. Balusamy et al.[150] also studied scratched surfaces and noted that abraded epoxy on top of carbon steel resulted in a decrease in $|Z|$ due to an accumulation of intermediate corrosion products as opposed to decreased $|Z|$ from water induced adhesion loss.

The NEIS protocol also provides an alternative technique in capturing the area-normalized electrochemical impedance data with respect to other reported localized electrochemical impedance spectroscopy (LEIS) methods[151]. Others like Bayet et al.[152] have used a scanning vibrating electrode technique (SVET) to measure local potential and current to define impedance during simulated corrosion. Wittmann et al.[153] detected chemical and physical defects like absorbed oil and subsurface bubbles of organic coatings on steel using a five-electrode system with a split microreference electrode. Using a scanning electrochemical microprobe, Zhong et al.[154] found that impedance properties of oxide film defects are both size and time dependent. The oxide film repassivation is affected by the accumulation of localized corrosion

byproducts over time for defects measuring under 200 μm in diameter, whereas defects larger than this were resistant to the effects of byproduct accumulation and time due to the larger open geometry of the defect.

The NEIS protocol could be used to further investigate the breakdown conditions at the grain boundary within several alloys susceptible to intergranular corrosion. Annergren et al.[154, 155] successfully used LEIS protocols to study pit initiation and growth on iron-chromium alloys, specifically noting how the EIS response at the active sites differed from the global spectra with location and time-influenced contributions from the passive areas. Baril et al.[156] used LEIS techniques on as-cast AZ91 magnesium alloy in Na_2SO_4 electrolyte, noting how the alloy corrodes at the grain boundaries with significantly decreased impedance properties before the rest of the alloy body. We would expect to see similar results using our NEIS techniques during tribocorrosion of the CoCrMo surface due to the alloy's microstructure with metal carbides corroding preferentially during wear[133].

The limitations of this technique exist in the feasibility of integrating it as a real-time diagnostic during revision surgery. Ideally, NEIS could be applied by a clinician in the operating room to determine the integrity of the surface in a very short time-scale with specific spectra ranges corresponding to a failed or near-failed implant. Measuring frequencies in the lower range corresponding to the state of the thin oxide plates is not currently practical in a surgery environment given the current time allotted per run (~ 2 hrs to measure down to 0.01 Hz at 10 points per decade). Also, the spectra obtained from the NEIS technique is to an extent, a function of the properties of the test method itself. Solution resistance and pH, ambient temperature, and time removed from physiological conditions will all impact the electrochemical properties and

oxide film physical properties. It is also possible that various corrosion mechanisms and materials on the surface share similar ranges of measured impedances, thus requiring secondary confirmation for failure-associated corrosion types via high magnification imaging. Currently, this technique presents itself as a powerful alternative and/or supplement to visual inspection of retrievals given the correlations between higher corrosion scores (Goldberg scale) and decreased impedance measurements.

6.6. Conclusion

Impedance monitoring using NEIS techniques provides a complementary way to assess surface heterogeneities that are otherwise estimated subjectively. The NEIS results suggest that wetted surfaces damaged by electrocautery-induced plasma arcs, higher concentrations in hydrogen peroxide, and higher relative Goldberg scores result in significant changes in impedance and other electrochemical properties compared to the as-is polished CoCrMo surface. The work in this study provides a simple method for useful and reliable feedback for inspecting mixed damaged mode metallic surfaces. Developing relationships between extent of local damage and locally measured electrochemical properties is advantageous to the field of orthopaedics because it will lead to better diagnostics during retrieval analysis, supplementing the often subjective and qualitative clinician-based assessment.

7. Modeling synthetic synovial fluid for comprehensive *in vitro* testing in simulated periprosthetic joints using the Taguchi array approach

Wiegand, MJ, Khullar, P, Gilbert, JL. 2019. Modeling synthetic synovial fluid for comprehensive *in vitro* testing in simulated periprosthetic joints using the Taguchi array approach. (Prepared for publication).

Author names:

Michael J. Wiegand[a,b], Piyush Khullar[a,b], Jeremy L. Gilbert[a,b,*]

Affiliations:

[a]Department of Bioengineering, Clemson University, Clemson, SC

[b]Clemson University-Medical University of South Carolina Program in Bioengineering, Charleston, SC

7.1. Abstract

Previous models of synthetic synovial fluid have been developed to address specific questions related to tribological interactions with implant materials in the absence of cells. These models have generally included one single organic additive variation with the intended goal of measuring wear properties. This has resulted in a gap in knowledge of the interplay between multiple joint fluid species, tribocorrosion processes and cell processes that more closely represent the periprosthetic joint environment. The purpose of this work was to determine which synovial fluid components greatly influenced solution and material properties in the presence of cells with the intended development for future use in cell culture-tribocorrosion experiments of orthopaedic alloys. Using a Taguchi orthogonal array design of experiment, we were able to investigate individual contributions from five independent variables at 2 or 4 levels (ratios or concentrations) on 13 individual responses. The responses measured consisted of cell and solution response, as well as the direct current and impedance response. Using level average analysis, it was found that altering the hyaluronic acid (HA) to lecithin (PL) ratio resulted in the greatest effect on 12 of the 13 responses, with significant effects ($p < 0.05$) on the means (cell viability (%), reduced glutathione (GSH) intensity output (I/I_O), pH, constant phase element (CPE) capacitance (Q)) and signal-to-noise (S/N) ratios (GSH I/I_O, pH, solution resistance (R_S), Q). No single factor significantly affected each response, therefore reduced models can be made from our data set depending on the desired response. Solution 13 (HA: PL 4 (level), A:G 1, $[H_2O_2]$ 2, $[Co^{2+}]$ 2, $[Cr^{3+}]$ 1) resulted in the greatest decrease in cell viability in addition to relatively (compared to all other solutions) large increases in pH and GSH I/I_O. Given this information and how it relates to the joint fluid environment, this solution is recommended to mimic severely inflamed joint fluid in a cell culture-tribological setting. Synthetic synovial fluid

is very difficult to model as the system surrounding a joint is dynamic in nature, and by using a condensed factorial design (Taguchi approach), we were able to study and determine which factors might be contributing to the overall behavior at the solution-metal interface.

Keywords: synthetic synovial fluid, CoCrMo, Taguchi methods, cell viability, electrochemical

7.2. Introduction

There have been approximately one million metal-on-metal (MoM) total hip arthroplasties (THAs) implanted worldwide with the primary goal of restoring patient quality of life[157]. The most common cases for revision within a THA are infection, aseptic loosening, or painful inflammation due to adverse local tissue reactions (ALTR)[158]. ALTR is hypothesized to originate from degradation of the material's bearing surfaces where soluble wear particles are engulfed by surrounding tissue[159] leading to fibrosis, necrosis and aseptic lymphocytic vasculitis-associated lesions (ALVAL)[160], however the exact origin of ALTR remains unknown or is not universally accepted. Revision and removal of implants associated with ALTR can be assessed through pain, discomfort and detailed visual inspection of the implant surface, however retrieved synovial fluid analysis can reveal in much more detail the unhealthy state environment of the periprosthetic joint.

Synovial fluid plays a critical role within joints by providing lubrication, both hydrodynamic and boundary[161] and reducing friction between articular cartilage during movement[162]. Healthy synovial fluid is principally made up of hyaluronic acid (HA), proteins, proteoglycans and phospholipids, in addition to other smaller constituents[163]. Synovial fluid diagnosis can be both quantitative and qualitative by assessing the fluid's color, viscosity, and white blood cell count, amongst other factors, with strong correlations existing between wear damage and metal ion concentrations in serum and synovial fluid[164, 165]. Inflamed, osteoarthritic, infected and otherwise unhealthy joint fluid can contain a variety of indicators such as high metal ion, ROS, phospholipid and protein concentrations, oxide and wear debris, as well as degraded proteoglycans such as lubricin and most notably, lower molecular weight HA[166-169].

The standard for simulating synovial fluid during *in vitro* wear tests is fetal bovine serum (FBS) due to its viscosity and lubricating characteristics, however there has arisen concerns as far as the simplicity of this solution, degradation and precipitation of proteins, and electrochemical characteristics and accuracy of joint simulation[170]. It has been reported that retrieved synovial fluid has electrochemical properties that differ drastically from FBS, chiefly hypothesized due to the effects of ROS, with open circuit potentials (OCPs) related to the color of the fluid and corrosion rates much larger than expected[171]. These properties were also shown to have a direct impact on CoCrMo alloys after immersion when compared to phosphate buffered saline (PBS) and water, where the retrieved synovial fluid created a thin oxide-hydroxide layer[172].

It is well documented that some of the major constituents of synovial fluid not found in FBS such as HA and metal ions directly impact inflammation properties, surface-solution interactions and organometallic composite layer formation surrounding an artificial joint. HA in addition to proteoglycans and proteins competitively adsorb to the surface, contributing to a multilayer film composite on top of the metal-oxide film and underneath a much thicker albumin-phosphate layer[173]. Albumin and phosphates adsorb to the surface, thus altering the passive conditions and capacitive electrochemical behavior, and ultimately the corrosion susceptibility of the implant. Amino acids react with metallic surfaces to form another type of organometallic oxide composites that aid in lubrication properties, specifically reducing friction and wear[174]. MoM hip replacements elevate local levels of cobalt (Co^{2+}, 30 μM) and chromium (Cr^{3+}, 25 μM) ions in the synovial fluid with wear compared to normal whole blood levels (0.005 μM) while having a direct impact on human osteoclast and osteoblast viability *in vitro*[175, 176]. In comparison, metal-on-polyethylene (MoP) hip replacements release far less polyethylene (PE)

particles than metal ions from MoM hip replacements, however the actual volume of PE particles is much higher due to their relative size with respect to metal ions[30]. Similarly, a metal ion dose-dependent non-linear lymphocytic response produced by the bearing surface contributing to surface necrosis and inflammation has been studied and defined[177].

While the above studies have explored the role of synovial fluid interactions with metallic surfaces in vivo, there is little work focused on developing appropriate simulated synovial fluid compositions for in vitro analysis of tribocorrosion and cell response/interaction. This coupling of the tribocorrosion processes with living cell systems in vitro will further advance our ability to assess the interactions between biomaterials-focused degradation processes and the associated biological inflammatory and cell-killing processes associated with ALTR. Such an in vitro test approach could assist in asking and answering fundamental questions about tribocorrosion degradation and ALTR.

Therefore, the goal of this study was to create synthetic synovial fluid using a simplified factorial design (Taguchi) that could be tailored for tribocorrosion-based experiments involving cell culture. By applying a Taguchi design using multiple factors and levels, we were able to test a range of compositions representing healthy and diseased or inflamed joint fluid in order to determine which components of synovial fluid most significantly influence material and electrochemical properties while minimizing experimentation time and supplies used. This work explores specifically the effects of HA to phospholipid (lecithin) (HA:PL) and albumin to globulin (A:G) ratios, as well as the presence of metal ions (Co^{2+}, Cr^{3+}) and ROS (H_2O_2). Factors were assessed using a level average analysis technique on 13 different dependent variables, split into three categories (cell and solution response, direct current (DC) response, and alternating

current (AC) response). Analysis methods were used to determine significant and insignificant competing factors for use in future tribocorrosion formulations.

7.3. Materials and Methods

7.3.1. Taguchi DoE

The Taguchi method was invented by Genichi Taguchi for assessing how different factors and levels within the factors influence the overall mean and variance[178]. Taguchi methods are systematically designed into three components: orthogonal design, experimentation and analysis. The experimental design is set-up to collect data in order to determine which factors and levels have the greatest influence on the output while minimalizing experimentation. The correct array is assembled based on same-level factors or a mixed model. The statistical independence of these arrays allows for the separation of confounding variables in an accurate and reproducible manner. Arrays can be identified in the form $L_A(B^C)$ where A denotes the number of experiments, B represented the number of levels per any given factor, and C symbolizes the number or factors or columns within the array (array dimensions, A×C). For mixed level models (multiple factors with different levels), a secondary designator can be applied within the parentheses as such $L_A(B^C \times D^E)$.

There are several techniques within Taguchi array analysis that can be used to report statistical significance and differences within individual trials. Level average analysis determines the average effect of each factor within the array specific to the level chosen, with the overall goal of determining the independence or mixed-factor interaction effects. Level average (L_m) can be calculated as such

$$L_m = Average(T1 + T2 + \cdots Tn) \quad [15]$$

where T1 is the first trial result, T2 is the second trial result, etc., and n is the number of trials. For example, if there were four trials run (T1, T2, T3, T4) and factor A consisted of two levels (A1, A2), then the level average calculations would be

$$L_{A1} = \frac{T1+T2}{2} \quad [16]$$

$$L_{A2} = \frac{T3+T4}{2} \quad [17]$$

where L_{A1} is the average effect of factor A at level 1 and L_{A2} is the average effect of factor A at level 2. The impact of each factor or range (Δ) is the difference between the highest and lowest average response, or in this given example,

$$\Delta_A = |L_{A1} - L_{A2}| \quad [18]$$

All the factors within the array can be arranged and analyzed using this method in order to separate out the strongest and weakest factors within the design where the larger the range, the stronger the effect of that level.

7.3.2. *Taguchi DoE $L_{16}(4^2 \bullet 2^3)$*

Sixteen trials composed the Taguchi orthogonal array (Table 2) to investigate the effects of two four-level variables: HA:phospholipid (HA:PL) and albumin:globulin (A:G) ratio; and three two-level variables: $[Co^{2+}]$, $[Cr^{3+}]$ and $[H_2O_2]$ concentration. The four-level factors were set-up to mimic healthy, early osteoarthritic/inflamed (EOA), late osteoarthritic/inflamed (LOA) and severely inflamed/infected joint fluid material ratios found in supporting literature. Factor

levels were influenced by previous studies and reports regarding composition of retrieved and synthetic synovial fluid as well as cell and material effects due to inflammatory-species and metal ions.

Table 2: Taguchi experiments layout (levels), $L_{16}(4^2 \bullet 2^3)$

Trial	HA:PL	A:G	$[H_2O_2]$	$[Co^{2+}]$	$[Cr^{3+}]$
1	1	1	1	1	1
2	1	2	1	1	1
3	1	3	2	2	2
4	1	4	2	2	2
5	2	1	1	2	2
6	2	2	1	2	2
7	2	3	2	1	1
8	2	4	2	1	1
9	3	1	2	1	2
10	3	2	2	1	2
11	3	3	1	2	1
12	3	4	1	2	1
13	4	1	2	2	1
14	4	2	2	2	1
15	4	3	1	1	2
16	4	4	1	1	2

It has been reported that healthy synovial fluid contains 20 g/L proteins, an albumin to globulin ratio range of 1.6 to 1.8, 2-3 wt % HA and 300 nmol/mL phospholipids[163, 170]. Of the components listed, only protein concentration has a current ISO standard (20-40 g/L) for mimicking joint fluid properties in knee joint wear simulators[179]. Unhealthy joint fluid increases in protein and phospholipid content to around 60 g/L and 750 nmol/mL, respectively, with a decreasing albumin to globulin ratio of 1 and decreased HA wt % (0.3-1.8)[163, 170]. There have been several studies reporting metal ion concentrations (Co^{2+}, Cr^{3+}) of retrieved joint fluid from primary revisions (0.005 µM) to end of product life-cycle (25-30 µM, 54-113 µg/L)[164, 165, 175-177]. Previous work in our lab has tested the killing effects of hydrogen peroxide on cells cultured on

CoCrMo discs, where at 0.8 mM H_2O_2, 50% of U937 monocyte macrophage-like cells were viable with a complete lethal effect at 1 mM[180].

Using this collected information, four levels of HA:PL and A:G were created with 2 levels of [H_2O_2], [Co^{2+}] and [Cr^{3+}] (Table 3). For levels 1-4, HA and albumin content decreased with lecithin and globulin content increasing. HA wt% decreased with increasing level, with successive levels signifying decaying HA or increase inflammation. Total protein concentration (A+G) increased with increasing level, where level 1 was consistent with healthy joint fluid protein levels and level 4 was consistent with severely inflamed protein levels. The three inflammatory-species factors were tested at either a zero concentration (level 1) or 1 mM for H_2O_2 and 0.1 mM for [Co^{2+}] and [Cr^{3+}] (level 2). It should also be noted that we chose to apply dynamic ratios for HA:PL and A:G rather than separating the factors into 4 concentrations ([HA], [PL], [A], [G]). This was justified by several supporting reports detailing concentrations of these constituents in retrieved joint fluid, and our goal of developing the most comprehensive and repeatable model.

Table 3: Designed Taguchi factors and levels

Levels	HA (g/50 mL)	PL (g/50 mL)	HA:PL	A (g/50 mL)	G (g/50 mL)	A:G	A+G (g/50 mL)	[H_2O_2] /mM	[Co^{2+}] /mM	[Cr^{3+}] / mM
1	0.15	0.011	13.3	0.637	0.364	1.75	1	0	0	0
2	0.1	0.016	6.21	0.9	0.6	1.5	1.5	1	0.1	0.1
3	0.05	0.021	2.39	1.11	0.889	1.25	2	-	-	-
4	0.02	0.024	0.828	1.25	1.25	1	2.5	-	-	-

The desired effects (13 dependent variables) were measured in the presence of polished CoCrMo surfaces and separated into three categories: cell and solution response [cell survival rate (viability) of RAW 264.7 macrophages, induced macrophage reduced glutathione (GSH) production intensity (I/I_O) and solution pH], direct current (DC) response [OCP, corrosion potential (E_{CORR}) and current (i_{CORR}), passivating current (i_{PASS}), breakdown potential (E_{BREAK}), current at -800 mV (vs. Ref)] and alternating current (AC) response [solution resistance (R_S), polarization resistance (R_P), constant phase element (CPE) capacitance (Q) and CPE exponent (α)].

7.3.3. *Materials*

Phosphate buffered saline solution (PBS 1X), Dulbecco's Modified Eagle's Medium (DMEM 1X), fetal bovine serum (FBS), penicillin/streptomycin (PSG), hyaluronic acid (HA), lecithin (PL), bovine serum albumin (A), bovine gamma globulin G (G), cobalt(II) chloride hexahydrate ($CoCl_2 \cdot 6H_2O$), chromium(III) chloride hexahydrate ($CrCl_3 \cdot 6H_2O$), hydrogen peroxide (H_2O_2) and anhydrous ethyl alcohol (EtOH) were all used as received (Fisher Scientific). Cell viability (MTT) and glutathione detection (ThiolTracker Violet) assays were used as received and operated using recommended instructions (Fisher Scientific).

Solutions were synthesized by adding 1% (v/v) PSG to DMEM 1X, then adding factors (HA, PL, A, G, H_2O_2, Co^{2+}, Cr^{3+}) one at a time until fully dissolved and mixed. pH was measured (n=3) prior to all cell culture and electrochemical experiments.

7.3.4. Sample Preparation

High-carbon CoCrMo alloy discs (ASTM F-*1537*) were polished up to 600 μm grit, rinsed with deionized water, sonicated with 70% ethyl alcohol for 30 mins and dried using nitrogen before each polarization and impedance scan.

7.3.5. *Cell Culture*

The principle cell types found in the synovium (lining of the cartilage) and synovial fluid are macrophage-like cells responsible for phagocytic and inflammatory functions, and fibroblast-like cells (chondrocytes) responsible for structural support and molecule transport phenomena such as the rapid diffusion of glucose throughout the joint space or enhancing the lubrication by decreasing the surface friction[181, 182]. For the purposes of this work, macrophages were chosen to represent the overall cell response. RAW 264.7 macrophages (ATCC, Rockville, USA) were cultured in 75 cm^2 Falcon T-flasks in DMEM 1X medium with 10% (v/v) FBS and 1% (v/v) PSG at 37°C (5% CO_2) until confluent. Cells were seeded at a density of 1×10^5 cells/mL in 24 well tissue culture-treated plates, and all tests were conducted using cells of the same passage for consistency. Test solutions (1 mL) were added to wells and three control wells (1 mL DMEM + 10% FBS + 1% PSG) were incubated for 48 hours.

7.3.6. *MTT Assay*

Test solutions were removed and fresh growth media + 10 μL of 12 mM MTT (3-(4,5-dimethylthiazol-2-yl)-2,5-diphenyltetrazolium bromide) was added to each well following 48 hours incubation. The resulting mixture was then incubated for 4 hours at 37°C (5% CO_2). The blue crystals were then dissolved in 50 μL of DMSO, thoroughly mixed using the pipettor and

incubated for 10 minutes. Absorbance was measured at 540 nm. All measurements were repeated in triplicate and cell viability (%) was calculated as such:

$$Cell\ viability\ (\%) = \frac{Absorbance\ of\ cells\ exposed\ to\ simulated\ synovial\ fluid \times 100\%}{Absorbance\ of\ the\ control\ cells} \quad [19]$$

7.3.7. Glutathione Detection Assay

Test solutions were removed and 100 µL ThiolTracker Violet dye solution (dissolved in DMSO) in thiol free buffer (1 mL) was added to wells. Following incubation for 30 minutes, cell fluorescence (I_{GSH}) measured using the appropriate excitation and emission wavelengths (λ_{ex} = 404 nm, λ_{em} = 526 nm) against the control (I_O). Fluorescence was calculated as such:

$$\log\left[{I_{GSH}}/{I_O}\right] = \log\left[\frac{Fluorescence\ of\ cells\ exposed\ to\ simulated\ synovial\ fluid}{Fluorescence\ of\ the\ control\ cells}\right] \quad [20]$$

7.3.8. Electrochemical Experiments

CoCrMo discs with an exposed surface area of approximately 4 mm^2 were submersed into solution within an electrochemical chamber. Silver chloride-silver (Ag/AgCl) and platinum (Pt) wires served as the reference and counter electrodes, respectively. Samples were held at open circuit potential (OCP) for 60 mins, allowing for potential stabilization prior to EIS measurements (±0 V vs. OCP) across a frequency range of 20,000 to 0.01 Hz using a cyclic 10 mV sinusoidal wave. Interfacial polarization resistance (R_P), constant phase element (CPE) capacitance (Q), CPE exponent (α), and solution resistance (R_S) were fit to the Randles circuit model made up of basic resistors and capacitors using a non-linear least squares fitting program in ZView (Scribner, Southern Pines, NC). CoCrMo surfaces with complex responses were fit to one of two electrically equivalent coated models where two resistors and CPE capacitors are

used to model the impedance behavior. The larger reported resistance represents the thin plated oxide layer in the lower frequency range (interfacial oxide resistance, R_{OX}) whereas the smaller resistance is the thick material evident in the higher frequency range (corrosion resistance, R_{CORR}). Following impedance measurements, anodic polarizations were performed from -0.2 V_{OCP} to 1V_{REF} on samples at a scan rate of 0.5 mV/sec. Cathodic polarization scans were performed from +0.2 V_{OCP} to -1V_{REF} at a scan rate of 0.5 mV/sec. Corrosion potential (E_{CORR}) and current (i_{CORR}) were calculated using Tafel slopes about the OCP. The passive current density (i_{PASS}) was defined as the current density in the anodic region where increase in applied potential did not change the measured current density. The breakdown potential (E_{BREAK}) of the protective oxide was defined as the potential at which the current density increased abruptly beyond the passive current density. E_{BREAK} and i_{PASS} were calculated by extrapolating the passive region and transpassive anodic lines of the polarization scan and determining the intersection point. Current at -0.8 V_{REF} was used as a proxy for cathodic kinetics.

7.3.9. *Statistical Analysis*

Experimental techniques were repeated in triplicate (cell viability, GSH I/I_O, pH), duplicate (OCP, E_{CORR}, i_{CORR}, R_S, R_P, Q, alpha) or single measurement (i_{PASS}, E_{BREAK}, i @ -800 mV). Averages and standard deviations (SD) were reported and comparisons between solutions, factors and levels were made using Taguchi methods and Analysis of Variance (ANOVA). Signal-to-noise (S/N) ratios were reported where the larger the effect (maximized desired effect against low noise) was taken to be better. S/N ratios where the response is maximized was calculated using the following equation in the analysis software (Minitab)

$$S/_N = -10 \times \log_{10}\left(\frac{\sum \frac{1}{Y^2}}{n}\right) \quad [21]$$

where Y is the observed outcome for each of n trials. ANOVA was performed on all calculated means and S/N ratios. A 95% confidence interval ($p < 0.05$) was taken to be significantly different.

7.4. Results

The effects of five factors in synthetic joint fluid at different levels were assessed by cell and solution response, DC and AC electrochemical properties using a Taguchi orthogonal array. Taguchi analysis methods were compiled into various tables and charts (means and standard deviations, level average impact range table, and S/N ratio intensity and statistical significance tables) to determine the effect and significance of individual factors and levels. Tables 4-6 display the means and standard deviations for properties relating to cell and solution response (Table 4), the DC response (Table 5) and the AC response (Table 6) for polished CoCrMo alloy exposed to the solution.

Table 4: Taguchi results, cell and solution response

Trial	Cell viability (%)	St. Dev.	GSH (I/I_O)	St. Dev.	pH	St. Dev.
1	71.09	3.80	1.36	0.02	7.82	0.01
2	92.90	25.41	1.29	0.09	7.79	0.00
3	81.37	11.34	1.36	0.01	7.67	0.01
4	60.32	7.06	1.32	0.05	7.66	0.01
5	90.64	5.84	1.28	0.17	7.77	0.01
6	77.41	1.63	1.12	0.07	7.86	0.00
7	103.42	6.75	1.20	0.05	7.80	0.01
8	104.50	6.36	1.22	0.05	7.75	0.01
9	105.09	20.12	1.40	0.13	7.95	0.00
10	118.28	29.90	1.47	0.08	7.92	0.00
11	84.07	7.90	1.22	0.07	7.73	0.00
12	91.42	12.65	1.28	0.02	7.68	0.01
13	55.34	3.82	1.35	0.00	7.91	0.01
14	71.49	2.89	1.24	0.05	7.98	0.00
15	80.01	2.21	1.11	0.02	7.85	0.00
16	94.15	7.31	1.15	0.05	7.88	0.00
Average	**86.34**	**9.69**	**1.27**	**0.06**	**7.82**	**0.01**

The effect of solution chemistry on cell culture response was assessed by comparing variables shown in Table 4. The cell viability (%) ranged from 118 to 55. The viabilities measured over 100% are explained by test solution wells having more surviving cells (greater absorbance) than the control wells, not an increase in cell proliferation. The GSH fluorescent intensity ranged from 1.47 to 1.11, indicating that all solutions produced a reduced glutathione intensity response. All solution pH values were slightly basic with a measured range of 7.98 to 7.66.

The effect of solution chemistry on CoCrMo corrosion performance was assessed by comparing variables shown in Table 5 (for DC response) and Table 6 (for AC response). The DC responses can be seen in Figure 26, where schematic lines indicate where E_{BREAK} and i_{PASS} were measured for all solutions with a 1X PBS control comparison. The measured stable OCP ranged from -300 mV to -450 mV. The corrosion current density at E_{CORR} was measured to be between

27.5 and 50 nA/cm^2. The passive current density was between 1.50 and 2.50 µA/cm^2. The breakdown potential was measured between +250 mV and +325 mV. These results were lower than those recorded for 1X PBS (i_{PASS}: 3.70 µA/cm^2, E_{BREAK}: +500 mV).

Table 5: Taguchi results, DC response

Trial	OCP (mV)	St. Dev.	E_{CORR} (mV)	St. Dev.	i_{CORR} (A*10^{-8})	St. Dev.	i_{PASS} (A/cm^2)	E_{BREAK} (mV)	i @ -800 mV (A/cm^2)
1	-389.00	2.00	-394.50	30.50	4.56	0.44	2.50E-06	246.00	7.00E-06
2	-335.00	41.00	-318.50	31.50	4.33	0.64	2.20E-06	302.00	1.36E-05
3	-397.50	2.50	-389.00	11.00	2.80	0.66	2.00E-06	311.00	5.66E-06
4	-332.50	5.50	-296.00	35.00	2.83	0.83	1.80E-06	342.00	1.52E-05
5	-355.00	35.00	-304.00	74.00	6.83	3.18	1.50E-06	320.00	3.09E-05
6	-430.00	3.00	-412.50	1.50	3.54	0.08	1.50E-06	300.00	5.72E-06
7	-330.00	12.00	-313.00	15.00	4.26	0.40	1.80E-06	265.00	1.15E-05
8	-322.00	28.00	-296.00	27.00	4.80	0.50	1.80E-06	270.00	8.85E-06
9	-428.00	33.00	-399.50	27.50	4.98	3.75	2.00E-06	265.00	2.00E-06
10	-356.50	18.50	-344.50	12.50	3.88	1.04	1.50E-06	298.00	5.50E-07
11	-406.50	23.50	-394.50	44.50	4.92	4.80	1.63E-06	265.00	1.50E-07
12	-338.50	31.50	-325.00	25.00	4.17	0.47	1.70E-06	326.00	1.50E-05
13	-338.00	47.00	-321.50	38.50	3.34	0.07	1.80E-06	302.00	3.50E-05
14	-348.00	12.00	-319.00	15.00	3.90	1.49	2.00E-06	309.00	1.50E-05
15	-318.50	6.50	-304.00	11.00	3.64	0.27	1.50E-06	285.00	2.50E-05
16	-365.00	23.00	-347.50	17.50	3.66	0.22	1.50E-06	274.00	8.00E-06
Average	**-361.88**	**20.25**	**-342.44**	**26.06**	**4.15**	**1.18**	**1.80E-06**	**292.50**	**1.24E-05**

Table 6: Taguchi results, AC response

Trial	R_S ($\Omega \cdot cm^2$)	St. Dev.	R_P ($\Omega \cdot cm^2$)	St. Dev.	Q (sec^{α})/($\Omega \cdot cm^2$)	St. Dev.	Alpha	St. Dev.
1	6.25	0.00	3.14E+06	0.00E+00	3.47E-05	0.00E+00	0.88	0.00
2	3.93	0.32	6.18E+05	5.13E+04	3.22E-05	4.03E-06	0.93	0.02
3	6.07	0.16	1.07E+06	3.47E+05	3.26E-05	3.80E-06	0.93	0.00
4	6.69	1.03	6.84E+05	2.88E+04	2.76E-05	7.81E-07	0.92	0.02
5	5.37	0.00	6.91E+05	0.00E+00	2.51E-05	0.00E+00	0.94	0.00
6	4.21	0.27	7.14E+05	2.22E+04	3.26E-05	6.63E-06	0.93	0.00
7	4.40	0.37	5.21E+05	2.90E+04	2.64E-05	9.16E-07	0.94	0.00
8	4.15	0.14	5.63E+05	4.20E+04	2.56E-05	1.50E-06	0.94	0.00
9	5.92	1.44	7.07E+05	2.73E+05	2.58E-05	8.34E-07	0.91	0.01
10	5.94	1.10	6.70E+05	8.99E+04	2.17E-05	1.86E-06	0.93	0.01
11	5.78	0.29	4.25E+05	1.23E+05	2.79E-05	1.86E-07	0.92	0.02
12	5.13	0.18	5.69E+05	3.40E+02	2.49E-05	1.25E-06	0.94	0.00
13	5.36	0.48	7.42E+05	1.75E+05	2.15E-05	1.38E-07	0.94	0.01
14	5.33	0.25	3.83E+05	4.95E+04	2.30E-05	5.75E-07	0.93	0.00
15	4.84	0.59	5.59E+05	5.10E+03	2.03E-05	1.88E-06	0.94	0.00
16	5.54	0.46	7.52E+05	1.01E+05	2.21E-05	1.24E-06	0.94	0.00
Average	**5.31**	**0.44**	**8.00E+05**	**8.35E+04**	**2.65E-05**	**1.60E-06**	**0.93**	**0.01**

For EIS results, only constant phase element Q was affected by the solution chemistry. Q is a measure of interfacial capacitance and presence of albumin, phospholipids, etc. in solution is expected to change. The change in solution resistance R_S is expected due to the presence of metal ions (Co^{2+} and Cr^{3+}).

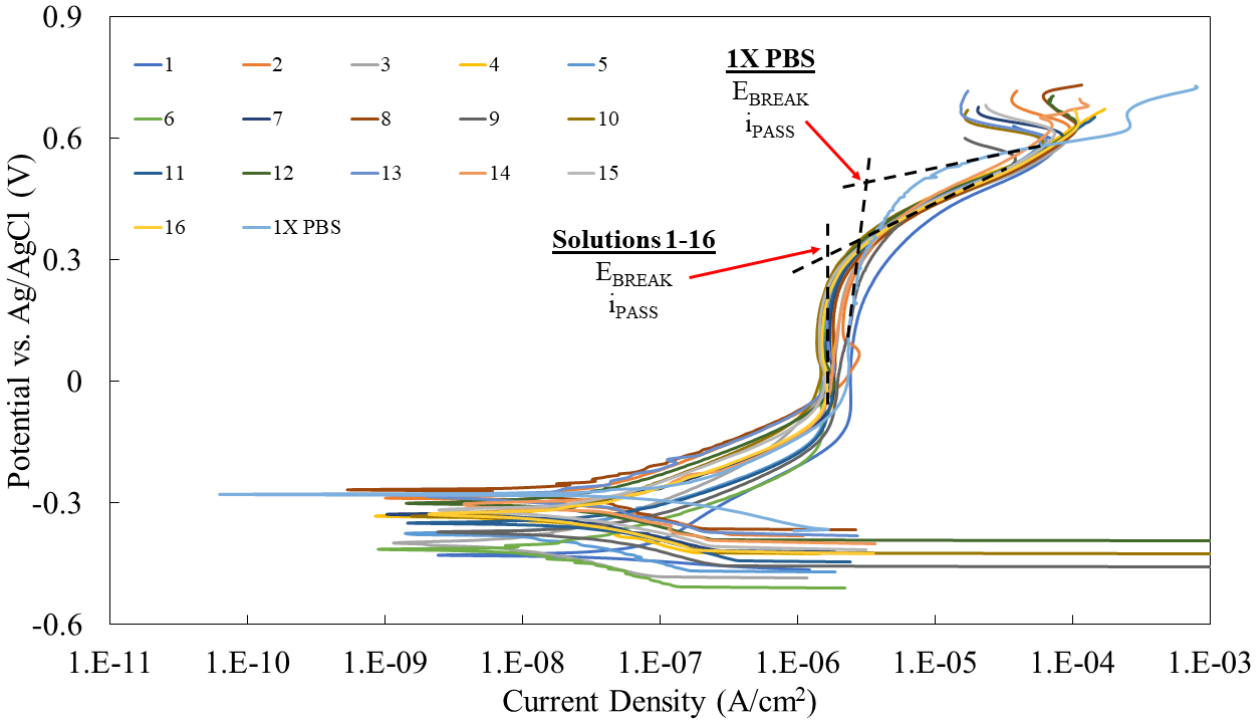

Figure 26: Passivation curves for all 16 test solutions and 1X PBS as a reference or control comparison. The synthetic solutions are not affected at the open circuit potential when compared to PBS, however during anodic polarization, the breakdown potentials and passivating currents decrease when compared to the control. It's possible the solution additives have no effect on the resting electrochemical properties, however once polarized, the species have interacting affects with the CoCrMo surface and structure of the oxide film.

Table 7 shows the ranked impact range (Δ) of the level average analysis of each factor (HA:PL, A:G, $[H_2O_2]$, $[Co^{2+}]$, $[Cr^{3+}]$) from 1-5, where 1 indicates the largest range for that individual response. The level average was calculated by averaging all the responses for that specific level, and the range signifies the difference between the highest and lowest average response for that factor. Overall impact range was also averaged per factor, where HA:PL had the greatest average impact (1.23) and H_2O_2 had the smallest averaged impact (4.23). Table 8 is a color-map with respect to the S/N ratio of all dependent variables where green indicates the highest S/N ratio and red indicates the lowest S/N ratio for each variable. Table 8 allows for the visualization of how each solution affected each response in terms of a measured signal. The maximized effects (largest numbers per response) are in in green with the lowest numbers in red. Because we

weren't trying to optimize any particular response, we chose to analyze all variables using the same S/N ratio calculation even though there are clear differences in meaning between high and low values when comparing variables (i.e. cell viability, pH, i_{CORR}, Q, etc.). Tables 9-10 display any statistically significant ($p < 0.05$) associations between the factors and response (boxed and highlighted in red) based on the means (Table 9) and S/N ratios (Table 10) calculated. Some responses are not present in the table due to limited sample size (n=1). HA:PL ratio had a statistically significant effect ($p < 0.05$) on the most response means (cell viability, GSH, pH, Q) and S/N ratios (GSH, pH, R_S, Q), while the presence of Cr^{3+} only had a significant effect on the R_S means. OCP, E_{CORR}, i_{CORR}, R_P and alpha means and S/N ratios were not significantly affected by any factor and Cr^{3+} did not significantly affect any S/N ratio. There exists a strong correlation between significantly affected means and S/N ratio.

Table 7: Taguchi results, ranked impact range (Δ)

Impact Rank	HA:PL	A:G	$[H_2O_2]$	$[Co^{2+}]$	$[Cr^{3+}]$
Cell Viability (%)	1	3	5	2	4
GSH (I/I_O)	1	2	3	5	4
pH	1	2	4	3	5
OCP (mV)	1	2	5	4	3
E_{CORR} (mV)	1	2	3	5	4
i_{CORR} ($A*10^{-8}$)	1	2	3	5	4
i_{PASS} (A/cm^2)	1	3	5	4	2
E_{BREAK} (mV)	4	2	5	1	3
i @ -800 mV (A/cm^2)	1	2	5	3	4
R_S ($\Omega \cdot cm^2$)	1	2	5	4	3
R_P ($\Omega \cdot cm^2$)	1	2	4	3	5
Q (sec^{α})/($\Omega \cdot cm^2$)	1	2	3	5	4
Alpha	1	2	5	3	4
Average Rank	**1.23**	**2.15**	**4.23**	**3.62**	**3.77**

7.5. Discussion

Using Taguchi methods, our design of experiment has allowed us to analyze individual effects from five different factors (2 or 4 levels) on 13 solution and material responses of CoCrMo alloy exposed to simulated joint fluid. By applying ANOVA to the means and signal-to-noise (S/N) ratio responses as well as ranking the level average analysis impact range, it was found that the ratio of HA:PL had the greatest effect on nearly every response, followed by the ratio of A:G and the inflammatory-species/metal ion presence. This agrees with previous studies on organic additives in addition to mechanical processes influencing both solution and material properties in synthetic joint fluid (Figure 27).

Table 8: Taguchi results, S/N ratio. The heatmap visualizes the S/N ratio per individual response ranging from red (lowest S/N ratio) to green (highest S/N ratio)

Trial	Cell Viability (%)	GSH (I/I_O)	pH	OCP (mV)	E_{CORR} (mV)	i_{CORR} ($A*10^{-8}$)	i_{PASS} (A/cm^2)	E_{BREAK} (mV)	i @ - 800 mV (A/cm^2)	R_S ($\Omega \cdot cm^2$)	R_P ($\Omega \cdot cm^2$)	Q ($sec^{\alpha}/(\Omega \cdot cm^2)$	α
1	37.00	2.70	17.87	51.78	51.84	13.06	-112.04	47.82	-103.10	18.92	132.95	-86.19	1.90
2	38.53	2.18	17.83	50.97	49.93	12.43	-113.15	49.60	-97.33	11.81	115.73	-90.06	-0.68
3	37.98	2.66	17.70	51.96	51.79	8.22	-113.98	49.86	-104.94	15.66	119.17	-89.91	-0.65
4	35.44	2.42	17.69	50.36	49.24	7.90	-114.89	50.68	-96.36	16.21	116.67	-91.18	-0.73
5	39.09	1.91	17.81	50.53	48.88	13.71	-116.48	50.10	-90.20	17.61	119.80	-89.00	2.43
6	37.77	0.93	17.91	52.70	52.31	10.97	-116.48	49.54	-104.85	12.44	117.06	-90.28	-0.60
7	40.24	1.53	17.84	50.21	49.88	12.47	-114.89	48.46	-98.79	12.78	114.30	-91.59	-0.55
8	40.34	1.69	17.79	50.50	49.32	13.48	-114.89	48.63	-101.06	12.35	114.93	-91.88	-0.56
9	39.90	2.78	18.00	52.94	51.97	4.72	-113.98	48.46	-113.98	14.68	114.98	-91.79	-0.85
10	40.56	3.31	17.98	51.26	50.73	10.83	-116.48	49.48	-125.19	15.04	116.28	-93.37	-0.68
11	38.39	1.71	17.77	52.42	51.75	-15.70	-115.76	48.46	-136.48	15.21	111.47	-91.10	-0.74
12	38.94	2.12	17.71	50.96	50.16	12.22	-115.39	50.26	-96.48	14.18	115.10	-92.12	-0.58
13	34.79	2.61	17.97	51.11	49.96	10.47	-114.89	49.60	-89.12	14.49	116.67	-93.33	-0.51
14	37.06	1.88	18.04	50.98	50.05	9.86	-113.98	49.80	-96.48	14.50	111.43	-92.77	-0.61
15	38.05	0.89	17.90	49.97	49.64	11.14	-116.48	49.10	-92.04	13.50	114.95	-93.97	-0.51
16	39.40	1.16	17.93	51.50	50.79	11.21	-116.48	48.76	-101.94	14.78	117.29	-93.17	-0.52

It has been reported that HA, bovine serum albumin (BSA) and a phospholipid (dipalmitoyphosphatidylcholine (DPPC)) increased third body wear and volume loss, and altered friction coefficients in ultra-high molecular weight polyethylene (UHMWPE) bearings against titanium alloys during pin-on-disc abrasion tests in Hank's balanced salt solution[183]. Other studies have found that when albumin adheres to the biometallic surface, there is a decrease in wear[184] and decrease in transfer of polymeric material into solution during tribocorrosion with increased lubrication properties[185]. Alternatively, other reports have confirmed that albumin increases the wear rate of CoCrMo surfaces during mechanical testing in 'biomimetic' solutions containing HA and alendronic acid sodium[186]. Park et al.[187] found that CoCr femoral head microfrictional response was dependent on HA and DPPC concentrations, with the optimal concentration for lubrication within the synovium (minimal wear loss) being 3-4 g/L HA (close to physiological levels) and 0.2 g/L DPPC, however there were no combinatory studies on the effects of both variables on lubrication. With respect to electrochemical properties, the current density of CoCrMo surfaces immersed in HA-rich solutions decreases while a thick layer of calcium phosphate precipitates on the surface as a result of local reactions at the surface with calcium ions cleaving hyaluronic chains[188]. Lewis et

Table 9: Taguchi results, Analysis of Variance on means ($p < 0.05$, red)

Means ANOVA (p)	*HA:PL*	*A:G*	*$[H_2O_2]$*	*$[Co^{2+}]$*	*$[Cr^{3+}]$*
Cell Viability (%)	0.042	0.663	0.692	0.011	0.477
GSH (I/I_O)	0.015	0.058	0.012	0.937	0.892
pH	0.004	0.003	0.14	0.014	0.536
OCP (mV)	0.732	0.564	0.923	0.956	0.355
E_{CORR} (mV)	0.661	0.708	0.573	0.837	0.595
i_{CORR} ($A*10^{-8}$)	0.213	0.328	0.214	0.63	0.567
R_S ($\Omega \cdot cm^2$)	0.055	0.352	0.035	0.086	0.041
R_P ($\Omega \cdot cm^2$)	0.595	0.758	0.973	0.736	0.151
Q (sec^{α})/($\Omega \cdot cm^2$)	0.022	0.427	0.108	0.175	0.875
Alpha	0.16	0.797	0.729	0.959	0.603

al. found that the surface protein-ligand film formed in the presence of synovial fluid triggers a release of Cr proportional to the oxide film thickness[172].

While there is a vast catalogue of synthetic synovial fluid-based studies in addition to the ones mentioned previously, most to date have focused singularly on the improvement of mechanical or wear properties of the solution, with a limited scope in the presence of cell culture material. Wimmer et al.[189] found that there exists a "mechanical mixing" process at the tribochemical reaction layers on the contact surfaces in MoM bearings, where organic composite material (nanocrystalline in structure initiated from the synovial fluid) hinders direct metal contact, which in turn limits wear and adhesion during sliding motion. Patterned microtexture designed to decrease the contact area has been shown to decrease wear loss of the polyethylene component and improve the longevity and anti-inflammatory properties[159], however this model hasn't tested the effects of elastic deformation or the *in vivo* elastohydrodynamic lubrication of the synovial fluid. Due to the complexity of all the different components present within synovial fluid that influence both mechanical and biological interactions, a Taguchi factorial design approach had to be adapted in order to determine which variables, concentrations and ratios have the greatest effect on the cell response and electrochemical properties of the synthetic synovial fluid.

Table 10: Taguchi results, Analysis of Variance on S/N ratios ($p < 0.05$, red)

S/N ANOVA (p)	*HA:PL*	*A:G*	*$[H_2O_2]$*	*$[Co^{2+}]$*	*$[Cr^{3+}]$*
Cell Viability (%)	0.054	0.647	0.859	0.019	0.547
GSH (I/I_O)	0.014	0.078	0.01	1	0.807
pH	0.004	0.003	0.146	0.013	0.539
OCP (mV)	0.606	0.772	0.744	0.687	0.624
E_{CORR} (mV)	0.688	0.785	0.692	0.995	0.683
i_{CORR} ($A*10^{-8}$)	0.334	0.485	0.767	0.313	0.729
R_S ($\Omega \cdot cm^2$)	0.048	0.213	0.033	0.041	0.055
R_P ($\Omega \cdot cm^2$)	0.54	0.773	0.747	0.967	0.154
Q (sec^{α})/($\Omega \cdot cm^2$)	0.031	0.652	0.206	0.233	0.784
Alpha	0.164	0.806	0.74	0.962	0.611

Similar to our study, the Taguchi method has been applied to determine the optimal variable levels and combinations for desired effects with an overall focus on decreasing the time and cost of the study compared to a full factorial design[190, 191]. Ghalme et al.[178] studied the effects of applied load and hexagonal boron nitride concentration (hBN) in silicon nitride (Si_3N_4) pins abraded against stainless steel (316L SS) discs. It was found that the interaction between the two factors resulted in the greatest effect on wear volume, followed by volume % of hBN and lastly the load. The optimal load + % hBN combination found in the orthogonal array analysis was

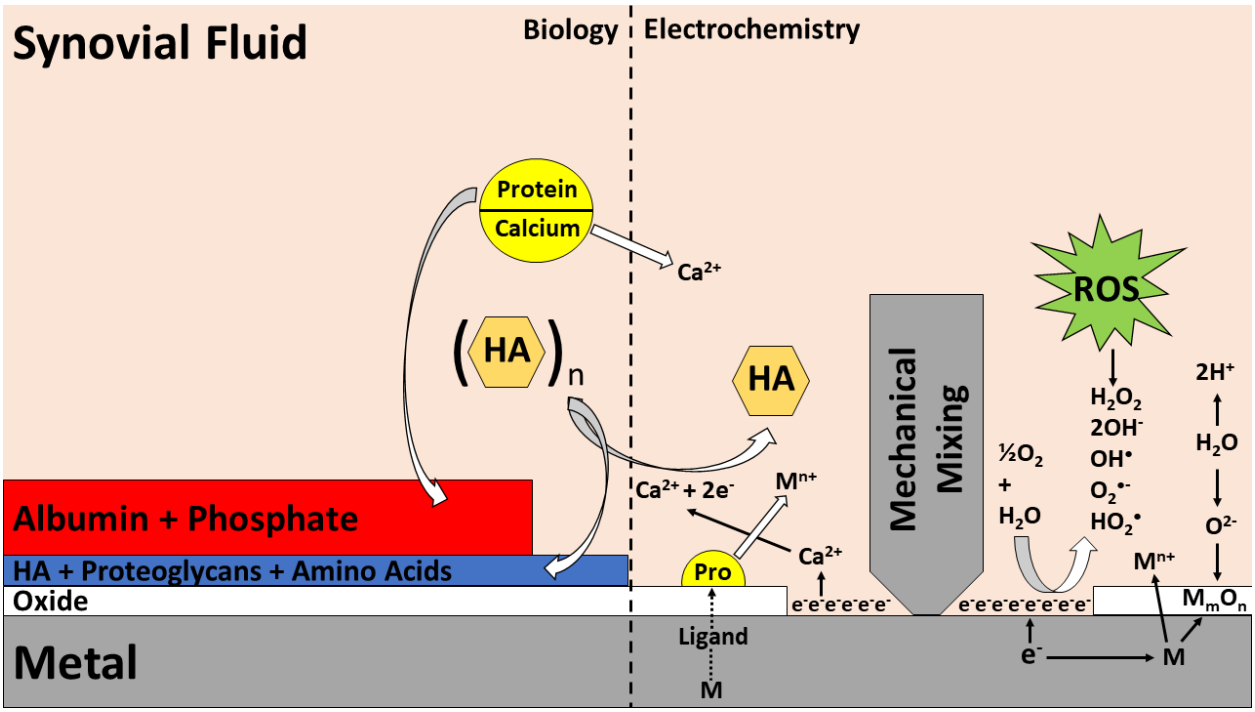

Figure 27: Schematic of how biology (left) and tribological-induced electrochemical processes (right) affect surface characteristics surrounding a biometallic implant. Components of synovial fluid like proteins will bind to calcium ions as well as create a thicker organometallic film on top of the thin oxide film. The remaining calcium ions then react with surface electrons to cleave hyaluronic acid chains, thus decreasing the overall current density[188] and decreasing the average HA molecular weight, as well as viscosity. There have been several reports detailing the outcomes of individual variables such as organic solution additives like albumin and hyaluronic acid (HA) or "mechanical mixing"[189] and disruption of the oxide film, however the combination of all factors likely influences the solution and material properties in unpredictable ways. Our model takes into account principal synovial fluid and electrochemical characteristics and is able to differentiate between significant and insignificant variables for a given response

used to further validate a simulated annealing (SA) technique. Others have studied the interactions between multiple variables on the cytotoxicity (cytokines, growth factors, hormones, etc.) in K562 cells[192] as well as the aging behavior (temperature, heating rate, humidity, gamma irradiation exposure, etc.) of UHMWPE[193] using a Taguchi orthogonal array. Kallel et al.[194] applied an $L_8(2^4)$ array to measure the effects of stirring speed, nature of serum, concentration of serum and nature of media on cell proliferation and monoclonal antibody (mAb) production from a spinner flask hybridoma culture.

Analyzing the data collected from our Taguchi approach for optimizing synthetic synovial fluid, we can accurately predict the cell, solution and material behavior given dynamic solution concentrations. Due to the complexity of all interacting and competing variables, it is difficult to make a recommendation for one given solution to represent healthy, mildly inflamed/corroding, or severely inflamed/infected/corroding. Alternatively though, we can report what factors significantly affect individual responses linked to clinical significance. In addition to this, factors that don't have a significant effect on the S/N ratio indicate that the strength of the signal is not impacted by the changing level of the factor, and thus a reduced model can be made. For example it was found that that HA:PL and $[Co^{2+}]$ significantly influenced cell viability while all other factors (A:G, H_2O_2, Cr^{3+}) did not. Therefore, only HA:PL and $[Co^{2+}]$ should be considered when testing solutions for cell viability. Additionally, HA:PL was the only variable with an effect on Q, indicating that there could be an adhered layer containing quantities of HA and/or PL that controls the CPE capacitance of the CoCrMo surface. These results agree with the previously mentioned reports on the effects of hyaluronic acid[188].

We hypothesize that we did not observe significant effects of the hydrogen peroxide or metal ions on many of the responses tested due to interacting effects with the organic molecules as well as differences in the RAW 264.7 macrophages compared to previously used cell types. It is possible that the metal ions are forming organometallic frameworks that are too large to be phagocytized by the macrophages, and thus only affected solution resistance. Our group has previously reported that 1 mM H_2O_2 in 1X PBS had a complete lethal effect on U937 cells cultured on CoCrMo discs[180], while the lowest viability achieved in these experiments when using 1 mM H_2O_2 was 55%. The GSH I/I_O results suggest that the RAW 264.7 cells were effectively metabolizing ROS using GSH, with several high viability readings corresponding with larger GSH intensities. This would imply that the larger cell viabilities are associated with high thiol concentrations and decreased intensities are associated with lower intracellular levels of non-oxidized GSH, however there were no definitive correlations between these two responses. It is also possible that the many solution ions and molecules reacted with the H_2O_2 molecules, cleaving the highly toxic ROS into the more reactive hydroxyl radicals as well as the less potent hydroxide ion (OH^-) and water molecules. This agrees with reports of enzymatically generated superoxide radicals from phagocytizing polymorphonuclear leukocytes reacting with hydrogen peroxide, forming hydroxyl radicals that then depolymerize hyaluronic acid in bovine synovial fluid[195, 196].

Analyzing the electrochemical properties with respect to the 1X PBS control comparison, it also remains unclear why the OCP was unaffected compared to the breakdown potentials and passivating current. Breakdown potential was the only response where HA:PL ratio did not have the largest impact range, but rather Co^{2+} ions did. Chromium ions also only had a significant effect on the solution resistance. We hypothesize that once the synovial solution components are

polarized, there are solution-material interactions involving the different metal ions and organic additives that directly impact the properties of the surface and oxide film. Others have similarly documented the effects of surface adsorption, where increased potentials increase the rate of adsorption and consequently, the breakdown of the passive film[197]. It remains unclear at this moment from a chemical and electrochemical interaction viewpoint why H_2O_2, Cr^{3+} and Co^{2+} didn't have a more significant effect on cell response and further studies should be conducted on these variable interactions. These effects will need to be characterized to better understand the kinetics and composition at the surface.

There exists several physical limitations when simulating inflamed joint fluid that cannot be accounted for *in vitro* such as tissue-induced systematic expression of matrix-degrading enzymes (metalloproteinases, aggrecanases), cytokines, chemokines and pro-/anti-inflammatory markers[60] and pressure gradient flow and exchange with circulating blood[198]. These factors, in addition to several others, make it nearly impossible to accurately predict local concentrations of synovial components within the joint space. It is likely that there are much higher concentrations of metal ions, ROS, and metabolites near and surrounding the local space around the articulating surfaces within the periprosthetic joint that dominate solution and surface properties, eventually diffusing into the greater solution volume. This presents a challenge that has yet to be extensively characterized in an *in vivo* setting.

The solution set tested is still elementary in terms of components present within a periprosthetic joint, however it is more advanced and comprehensive in terms of native constituents than pure FBS or saline-buffered solutions. There is no one solution tested that we can recommend that would simulate native joint fluid in a normal setting or an inflamed

environment. The purpose of this work was to categorize interacting effects between variables at different levels, and it was shown that HA:PL has the greatest overall effect on both material and biologics response. That being said, Solution 13 (HA: PL 4 (level), A:G 1, [H_2O_2] 2, [Co^{2+}] 2, [Cr^{3+}] 1) showed the greatest decrease in cell viability (55%) with complimentary large S/N values in pH, GSH I/I_O, and current at -800 mV (vs. Ref). This indicates that this solution set in addition to being the most cytotoxic, produces the best signal when capturing GSH activity and pH response as well as current at fretting-like cathodic voltages. Compiling all these responses, this solution most accurately represents the inflamed joint environment compared to all other solution tested in this study.

7.6. *Conclusion*

Retrieved synovial fluid surrounding a periprosthetic joint can describe the condition of both the joint and the implant, ranging from normal functioning to corroding and failing. The fluid can contain several markers such as metal ions, ROS and degraded organic material like hyaluronic acid chains, however it is not widely studied the effects of changing synovial fluid against biometallic alloys. Our work provides a preliminary study measuring the effects of organic solution additives and inflammatory-species on both solution and material properties. We believe that our solution set and analysis have provided key information as to what factors influence implant performance *in vitro*, however we expect that these properties would change *in vivo* due to the sheer complexity and dynamic nature of the native joint space.

8. Discussion

8.1. Summary

Orthopaedic biomaterials have been developed, refined and implemented for the intended purpose of restoring the quality of life of an individual suffering from pain, discomfort or any number of issues associated with failing joints. These biometallic materials provide excellent load-bearing properties in addition to their natural corrosion resistance by ways of a thin passive oxide film that forms on the surface. This film provides protection from the local tissue and synovial fluid, however it can be damaged through mechanical, biological, and electrochemical forces, leading to the cell-based attack and dissolution of the surface. One class of molecules that are present during this systematic physiological response are reactive oxygen species (ROS). The purpose of this dissertation was to characterize, define, and report clinically relevant levels of ROS produced and consumed in various aspects of the inflamed joint space. There are vast amounts of literature that define ROS in terms of mitochondrial and metabolic production, pro-/anti-inflammatory cell signaling and in response to stimuli, chemokines/chemotaxis and foreign particles. Yet, the shortcomings of our understanding of ROS are how these processes are intertwined within the chronically inflamed periprosthetic joint. The work presented here, in addition to previous work within the Gilbert Lab, supports the *feedback-loop hypothesis* where inflammation and corrosion drive each other in a physiological setting. The significance of the body of work presented in this dissertation is that if corrosion and inflammation are the vehicles that drive this feedback-loop to its final destination (failure of metallic biomaterials and devices), ROS are the fuel.

The key techniques and models developed in this work are fluorescently labeling individual ROS near a cathodically-polarized CoCrMo surface, establishing the 'electrochemical zone of viability', NEIS and the synthetic synovial fluid repository. The current technology (DCFDA) for ROS detection is widely accepted, yet it autofluoresces and cannot differentiate between individual ROS. These shortcomings magnify the significance of our results because we are combining established protocols into a new technique that can be applied to various experiments in our lab-group without affecting experimental set-ups or solution chemistry.

The 'electrochemical zone of viability' provides a basic understanding that in the low-end of the cathodic range that implants could be subjected to, macrophage-like cells are viable and pre-osteoblast-like cells are not. We believe this information is fundamental to our understanding of possible electrochemical-induced osteolysis surrounding an implant as well as the state of inflammatory cells during fretting corrosion-like cathodic excursions.

The refined nearfield electrochemical impedance spectroscopy (NEIS) method was developed in this dissertation to establish local surface heterogeneities with respect to electrochemical properties, and it successfully characterized different CoCrMo alloy surfaces subjected to a range of corrosion and damage conditions. This technique can be applied to any surface, curved or flat, with the ability to control working area and solution properties with an emphasis on real-time damaging effects of ROS, ROI, RCS and RNS. There have been recent developments with regards to impedance analysis, and once a shorter timescale is achieved, the limits of this method won't end in the lab. The instantaneous non-subjective (i.e., quantitative) assessment of retrievals will significantly reduce the time required and will limit the risk and bias when determining if an implant needs a revision or full replacement. Finally, the design of

simulated synovial fluid improves upon current technology and standards with respect to our understanding of material and solution interactions. Introducing more elements into experimental models like the synthetic synovial fluid study will introduce more room for interpretation, however it will also lead to more complex data analysis, reports, and new findings. The synthetic synovial fluid set tested is rudimentary in its concept and can include many more components, yet from our preliminary findings alone we have established the significant effects of HA, phospholipids and ROS on cell behavior and material properties using Taguchi methods.

Combining all the methods studied and established in this dissertation, we now have the ability to experimentally measure ROS concentrations during specific potentials within the 'electrochemical zone of viability' (while incorporating synthetic synovial fluid) and correlate cell death with individual ROS concentrations and solution parameters. Furthermore, we can analyze the surface following these tests using NEIS and see if the cell covered areas respond differently to NEIS AC signals than the surface not exposed to cells. We also have the ability to add ROS directly within the NEIS tip and further explore localized ROS contributions to corrosion behavior. This will provide further insight and build a more comprehensive benchtop model of ROS within a simulated periprosthetic joint environment.

Scientifically, the presence of ROS can be separated into three stages with respect to its presence and life-cycle in the joint space: 1) production, 2) consumption, and 3) reaction. In the collected research presented in this dissertation, we have defined the mechanisms and factors that contribute to ROS production (Chapters 4-5). We have measured by what means ROS are consumed (Chapters 4, 5, 7). And finally, we have investigated the lasting effects of ROS exposure on metallic surfaces (Chapters 6-7).

8.2. *ROS Production*

ROS production ($OH^{\cdot}$, H_2O_2) was measured using fluorophores through cathodic polarization of CoCrMo surfaces at varying potentials and time-scales. It was found that $OH^{\cdot}$ is formed in detectable quantities using terephthalic acid as a dosimeter in the presence of solution hydrogen peroxide and surface electrons, confirming basic electrochemistry principles where hydroxyl radicals are one byproduct of hydrogen peroxide reduction[47]. Furthermore, hydrogen peroxide is produced in measurable quantities from the surface and detected using pentafluorosulfonylbenzene-fluorescein, where the fluorescein group is cleaved by hydrogen peroxide molecules at the targeted sulfonyl linkage[75]. This is also in agreement with electrochemistry techniques where solution water and oxygen are reduced using one of two electrons to form hydrogen peroxide and superoxide anion ($O_2^{\cdot -}$)[79], although superoxide anion has not yet been detected using our protocol (See Future Work). Our results also indicate that H_2O_2 is produced in detectable limits at and below -600 mV (vs. Ag/AgCl) after 2 hours of polarization. While cells were not a part of this study (Chapter 4), it is likely that these results had a direct impact and are linked with those obtained from the cell electrochemical zone of viability study (Chapter 5), where we hypothesize that U937 cells mitigated electrochemically produced H_2O_2 using reduced glutathione (GSH) while MC3T3-E1 cells went into programmed cell death at voltages below -600 mV. This is in direct agreement with our electrochemical zones of viability established for the two cell lines, where MC3T3-E1 were not able to survive below -450 mV (vs. Ag/AgCl).

Monocyte macrophage-like cells (U937) were exposed to a range of cathodic voltages in direct comparison to previous studies[45], where it was found that cell phenotype directly influences the electrochemical zone of viability. U937 cells were able to survive (~25% viable)

from -1000 mV (vs. Ag/AgCl) to +250 mV (~93% viable) after 24 hours of polarization on CoCrMo surfaces, with a '90% zone of viability' between -500 and +250 mV. These results suggest that the U937 cells are more resistant to the killing effects of ROS, metal ion elution, and deaerated solutions than pre-osteoblast-like cells (MC3T3-E1) that had a much narrower 'electrochemical zone of viability' under the same test conditions (-400 < mV < +500)[87]. ROS were hypothesized to be the main killing agent behind the decreases in viability and that different cells contain different ROS-based defense mechanisms such as GSH.

Analyzing the broad spectrum of potentials that CoCrMo could be subjected to *in vivo* (-900 mV vs. Ag/AgCl during abrasion[96] < -250 mV at OCP < +600 mV during simulated inflammation using hydrogen peroxide[50]), there are several interacting mechanisms that are being influenced by ROS concurrently, with our results at the center of the discussion and in agreement with those previously reported.

To better visualize what is happening (theoretically and from our data), we will briefly describe the events happening in the lower and upper potential ranges that metallic biomaterials may experience during normal activities. In the lower range of the potential spectrum (< -500 mV): hydrogen peroxide and other ROS/ROI are produced continuously through reduction reactions, local oxygen concentrations are near-zero[40], metal ions are released from the surface (mechanically)[21] as well as through hydrogen peroxide interactions with the passive oxide film which decreases the polarization resistance of the surface. At the upper range of the potentials (> +500 mV), the passive barrier (oxide film) thickens, loses compactness and thus coefficient of friction is altered[50], charge transfer kinetics increase and metal ions are actively electrochemically eluted from the surface[8], and Cr^{3+} is oxidized to chromium(VI)[128] when the potential is above the transpassive potential (ca. 500 mV vs Ag/AgCl).

ROS plays an integral part in redox kinetics (altering the oxide and raising the oxidizing potential of the solution) in addition to triggering the onset of several systematic reactions (described above). While it is important to consider how ROS are produced and interact with the oxide film, it is equally important to understand how they are consumed within the solution-cell-metal composite interface and may affect the biological processes of the cells.

8.3. *ROS Consumption*

Using similar fluorescent probing techniques developed to measure ROS production, we were also able to measure ROS consumption. Terephthalic acid (TA) binds to OH· preferentially compared to other ROS, however it was found in our trials that it binds to free sodium and iron(II) ions over TA. Therefore, H_2O_2 in deionized water (DI) was introduced as the source of ROS with the polarized surface free to cleave solution H_2O_2. It was from these trials that we were able to capture hydroxyl radicals through the degradation of hydrogen peroxide, a phenomena that is known to occur at the surface and can be confirmed from our data. Hydrogen peroxide and TA were tested in the absence of polarized surfaces and there was no net increase in fluorescence, indicating that the charged surface was necessary in the conversion of H_2O_2 molecules into OH·. While it is crucial to understand how molecules like H_2O_2 are consumed by electrochemical reactions, the biological consumption of ROS is the concern of our research, hypotheses, and ultimate goals.

As previously stated, we hypothesized that the monocyte macrophage-like cells cultured on CoCrMo during cathodic polarization were subject to an influx of ROS produced from the surface, as well as intracellular ROS due to the oxidative stress-induced state of the cell. Reduced glutathione (GSH) activity within the cell can be correlated to the oxidative stress activity present with decreased glutathione activity indicating that GSH molecules are being

oxidized to their dimer (GSSG). Of the synthetic synovial fluid compositions tested (Chapter 7), the two solutions (Solution 9-10) with the highest measured cell viability (105% and 118%, respectively) also had the two highest GSH measured fluorescent intensities (1.40 and 1.47, respectively). Compared to Solutions 9-10, all other solutions had decreased cell viability and GSH intensity, although there was not a strong correlation (regression not reported) between the two responses. It should be noted though that H_2O_2 had a significant effect on the GSH I/I_O means as well as the signal-to-noise (S/N) ratio, confirming that ROS play a significant role in synovial fluid-linked oxidative stress. It is very possible that there exist interacting factors within the orthogonal array leading to compounding and varying effects on the data, which is why future work (See Chapter 10) will include reduced models to determine the correlation between cell viability and GSH activity.

8.4. *ROS Reaction*

ROS production and consumption have long been studied in the context of a periprosthetic joint, but the aftermath of ROS-induced damage is still a relatively new and incomplete topic of research. As stated previously, the consensus is that mechanical wear and the associated immune response are the primary causes of orthopaedic alloy surface damage. Our data has shown that ROS not only have measurable effects on cell behavior and viability, but on material performance as well.

Using our nearfield electrochemical impedance spectroscopy (NEIS) set-up, we were able to measure the localized corrosion and damage from common surgical techniques (electrocautery) as well as defined heterogeneities on non-articulating retrieval surfaces. CoCrMo discs exposed to H_2O_2 (1-10 mM) displayed changes in electrochemical properties, most notably at 5 and 10 mM with significant ($p < 0.05$) increases in OCP and Q and decreases

in alpha and |Z|. This agrees with previous statements reporting the effects on surfaces exposed to hydrogen peroxide.

The retrieved severely corroded CoCrMo neck tested using the NEIS approach experienced fretting motion and crevice corrosion conditions (i.e., was subjected to MACC) Therefore, it is reasonable to assume that this micro-motion induced a spike in currents, a decrease in potential and the production of detectable quantities of ROS at the interfaces *in vivo*. ROS generation may have occurred within the crevice region and outside of it as well, with greater amounts generated closer to the crevice/taper junction due to solution resistance effects. ROS production then, in theory, may be a stimulating factor driving the attraction of inflammatory cells and triggered the onset of chronic inflammation. That is, this work implies that ALTR effects may not be driven by metal debris only, and that ROS generation by the implant may be another important factor to consider both in terms of the biological effects as well as the changes to the corrosion resistance of the alloys.

ROS and metal ions were key components in our Taguchi orthogonal array to determine solution and material effects of simulated synovial fluid components. H_2O_2 had a significant ($p < 0.05$) effect on the GSH I/I_O and R_S means and S/N ratios. Co^{2+} ions significantly affected cell viability and pH means and S/N ratios, as well as R_S S/N ratios. Cr^{3+} ions also significantly affected R_S means. We also know from our trials that Co^{2+} and Cr^{3+} ions in the presence of H_2O_2 do not partake in Fenton-like reactions without applied potential. Looking at this information holistically, the presence of ROS and metal ions alter solution properties and as a result, cell behavior. Linking this information with the electrochemical properties obtained from retrieval surfaces and CoCrMo discs exposed to H_2O_2, it is clear the relationship ROS plays in cell death,

signaling of inflammation through GSH activity, and damage to the resistive properties of the material.

8.5. ROS ↔ Inflammatory Cells

The main functions of ROS produced by inflammatory cells (neutrophils, macrophages) have been well defined in the scope of cell signaling and killing through respiratory bursts. The respiratory burst by neutrophil mediated phagocytosis results in superoxide formation through the transfer of electrons across the vacuole wall via the nicotinamide adenine dinucleotide phosphate (NADPH) oxidase (NOX) protein complex[39]. While one-electron reactions predominate NADPH regulated generation of ROS, two-electron reactions where molecular oxygen is directly reduced to hydrogen peroxide exist within the mitochondria[37]. The rapid burst superoxide formation in the presence of nitric oxide in macrophages leads to the production of peroxinitrite radicals, which perform physiologically similar to hydroxyl radicals where they contribute to defense-related targeted apoptosis of foreign cells, tumors and pathogens[199]. NADPH is also required for the regeneration of GSH from GSSG through the activation of glutathione reductase[35]. In addition to killing, macrophage NOX enzymes activate kinases, transcription factors, gene expression and regulate programmed cell death and proliferation[38]. In signaling, ROS specifically activate the inflammasome to mark 'danger' with the subsequent release of pro-inflammatory cytokines such as interleukin (IL)-1β or the apoptosome is triggered to mark impending cell death[200]. The activation of the non-cell death key signaling complexes "turn-off" and "turn-on" complimentary mechanisms that result in the reversible oxidation of critical thiols (GSH→GSSG), which eventually return to their prestimulation steady-state levels[34].

ROS are linked with several signaling processes and are secreted from so many cellular sources/interactions that the study of their involvement in inflammation is partial to date, which contributed as the main influence on this body of research.

8.6. ROS ↔ Inflammation

This dissertation provides direct evidence of *in vitro* ROS-mediated inflammatory mechanisms and electrochemical ROS activity, however there is still a lot to be discovered with respect to ROS. To understand the role of ROS in inflammation, we must understand the life-cycle of ROS (ideally the molar balance in response to certain stimuli) and how it affects every step of the ***feedback-loop hypothesis***. As previously mentioned, ROS are produced in measurable quantities during mechanical abrasion of the oxide film, inherently leading to cathodic voltages[8, 43, 44]. Cathodic polarization of a metallic surface will lead to the production of hydrogen peroxide (H_2O_2) through the reduction of water and oxygen molecules, effectively killing strains of bacteria that can lead to infection on an implant surface[78]. There is also reason to believe that bacteria are not the only species attacked by the ROS influx. During cathodic excursions between -100 and -500 mV (vs. Ref), the volume-space 2 μm surrounding the implant surface becomes hypoxic with oxygen concentrations decreasing up to 25% (~100% O_2 reduction below -600 mV)[40]. In addition to voltage drop, mechanical abrasion will often lead to metal ion and particle release from the bearing surfaces with the resulting particles/ions phagocytized by local inflammatory cells[12]. After phagocytosis, ROS are generated intracellularly after the metal content is oxidized in association with Fenton-like reactions[27] and in combination with dysregulation of the mitochondrial membrane[32]. The cells then extrude reduced glutathione (GSH), a ROS scavenger, which catabolizes ROS into oxidized GSH (GSSG) as well as other metabolites[62]. These metabolites then permeate the cell membrane, signaling to the local tissue

the onset of inflammation, where upon the host will recruit more neutrophils, mast cells and macrophages leading to the formation of foreign body giant cells (FBGCs) and fibrous tissue capsulation surrounding an implant[12]. This is a simplified version of ROS involvement in wear-induced inflammation.

Alternatively, beginning with the foreign body inflammatory response, proteins adhere to the biomaterial surface and the development of a blood-based transient provisional matrix (preliminary blood clot/thrombus at the material-tissue interface) forms around the biomaterial[12]. Monocytes and neutrophils are then recruited as a part of the acute inflammatory process and eventually mature into macrophages[11]. Macrophages on the surface will produce nitric oxide (NO) to protect the host from infections with the surrounding tissue experiencing either an increase in protectiveness (picomolar concentrations) or damaging effects (nanomolar concentrations)[201]. In response to the secreted growth factors, proinflammatory cytokines and NO[31], FBGCs will form from macrophages and grow in number, releasing more ROS as signaling molecules in addition to enzymes[19] that trigger the differentiation of osteoclasts, promoting bone resorption and osteolysis[18]. The protective film becomes oxidized, porous and thickens, leading to metal ion release and dissolution of the surface during activation/repassivation cycles[20]. This results in microrough surfaces that are more conducive to macrophage activation and NO release[19]. This cycle is hypothesized to lead to further metal ion release and ROS production/consumption, which at last will accelerate metal ion release and the metal material-induced inflammatory reaction.

Using the background information presented as well as the original reports in this dissertation, we have identified and described several specific roles of ROS in the inflammatory and corrosion response of metal-biology contacts. In small quantities, ROS can prove beneficial

to local tissue in the form of cell communications and disease/bacteria/infection prevention, but just like any molecule in excess, ROS can have adverse effects on both biological response and material behavior.

8.7. Clinical Significance

It's been estimated that 90% of the population over 40 suffers from some kind of bone degenerative disease brought about by excessive loading or the absence of normal biological healing processes, with musculoskeletal disorders costing around 254 billion dollars to society[202]. Increases in life expectancy and ageing populations are hypothesized to contribute to rising numbers of osteoarthritic patients, which currently affects 9.6% of men and 18% of women over the age of sixty[4]. Between 2002 and 2004, hip replacements in Sweden rose 6.0% in patients under 50 years old, and by 11% in Canada for patients under 45 years of age[30]. The demand for longer-lasting implants is on the rise with an estimated increase (from 2005) in THAs and TKAs by 2030 to be around 174% (572,000 procedures) and 673% (3.48 million procedures), respectively[203].

Given the staggering numbers of anticipated THAs and TKAs that will be implemented in the next 10 years (not including revisions and replacements), it is clear that material-biological interactions in the periprosthetic joint space will be of great importance. While the work in this dissertation does not provide direct *in vivo* solutions to ROS-induced damage, therapies or smarter biomaterials, it sheds new light on how ROS contribute to the inflammatory response and corrosion of metallic surfaces *in vitro* using more advanced predictive models in terms of ROS produced both from the surface as well as inflammatory cells response. These models can be further advanced and applied towards our ultimate goal (See Future Work) of simulating a physiologically relevant *in vitro* inflamed joint environment.

There are two clinically relevant findings within the work presented here that need to be further discussed. First, electrocautery damage has a significant impact and should be continued to be explored. Early reports of inflammatory cell induced (ICI) corrosion[14, 15] are now believed to be more closely associated with electrocautery induced damage. The surface asperities' appearances are similar with pitting and trailing features, and it was found that even single electrosurgical burns can reduce both the global[137] and local resistive properties. Surgeons use this technique in excess while cauterizing blood vessels during both primary and revision surgeries[72], therefore it is reasonable to assume that the corrosion resistance is dramatically reduced compared to what was reported in this work. This information alone is of great importance because it supports a new type of damage that isn't widely studied or accepted at this point, and there is a range of properties from the aftermath of electrocautery that has yet to be defined such as surface deposits and debris from the electrosurgical pen, ROS generation and how it affects cell behavior (both locally and globally).

The other clinically relevant finding is the NEIS technique. As previously mentioned, implant viability is often subjective and up to the discretion of the operating surgeon during revision and replacement surgeries. The development of a location-based diagnostic method like NEIS will allow for quantitative confirmation of the surgeon's visual assessment. There do currently exist limitations with the NEIS technique such as the time required to capture the low frequency data in addition to multiple damage modes with similar impedance spectra. However, the significance of this work is its preliminary findings and feasibility. It has confirmed the electrochemical differences in damage modes and locations on a single surface using a simple pipette tip and wire electrodes. It's reasonable to assume that this method could eventually advance in its engineered design to that of a marketed medical device. That, in combination with

a new fast-acquisition data method, would make this method very clinically relevant. There are still several corrosion-based damage modes and effects that need to be explored using NEIS (See Future Work) that will expand on the results presented here.

9. Conclusion

The inflamed joint space is one that is dynamic, complex, and very difficult to model and predict. There are many contributing factors to the state of the periprosthetic joint, all of which can be traced back to material-biological interactions. These interactions can trigger a prolonged immune response based on the body's natural defense to a foreign body, or by ways of particulate release and accumulation from persistent attack and wear of the surface. This dissertation characterized reactive oxygen species, specifically hydroxyl radicals ($OH\cdot$) and hydrogen peroxide (H_2O_2), and their effect on cellular and material behavior. CoCrMo surfaces were extensively characterized during the production and consumption of ROS, as well as how the electrochemical properties were altered.

CoCrMo surfaces were cathodically stimulated to simulate corrosion-like potentials achieved during abrasion of the oxide film. H_2O_2 was produced in measurable quantities at -1000 mV (vs. Ag/AgCl) up to 16 hrs and at voltages -600 mV (vs. Ag/AgCl) and below after 2 hours of polarization. Hydroxyl radicals were found to be produced through electrochemical interactions with surface electrons and solution hydrogen peroxide at -1000 mV (vs. Ag/AgCl) up to 16 hrs. Based on current monitoring, the recorded amount of H_2O_2 was significantly below the calculated amount, indicating that there is a constant production and consumption of ROS in the experimental set-up. The experimental set-up also discovered that surface electrons are vital in the breakdown of H_2O_2, with solution metal ions not conducive to hydroxyl radical production in the absence of the charged surface.

Polarized CoCrMo surfaces with different cell lines cultured exhibited a direct influence of phenotype on survival, referred to as an 'electrochemical zone of viability'. It was found that

monocyte macrophage-like cells survived a wider range of potentials ($-1000 \leq mV < +500$) than pre-osteoblast-like cells ($-400 < mV < +500$), indicating that the inflammatory cells are surviving in larger cathodic biases due to an internal cell-specific defense mechanism absent in the pre-osteoblast-like cells.

Implant surfaces (CoCrMo) subjected to electrocautery- and ROS-induced damage, as well as a severely corroded neck retrieval were assessed electrochemically using nearfield electrochemical impedance spectroscopy (NEIS), and it was confirmed that single surfaces can have dramatically different resistive properties. Resistive properties including OCP, CPE Q, alpha and |Z| were all affected by varying damage conditions and severity on the same surface. Surfaces displayed dramatically reduced corrosion resistance characteristics, with dry electrocautery burns, 10 mM H_2O_2, and a relative Goldberg score of 4 producing the greatest decrease in all populations tested (with all test groups except for 1 mM H_2O_2 exposure resulting in a significant drop in impedance magnitude and increase in CPE Q). This work confirmed that the global surface of the implant behaves like the most damaged region and discovered that even single asperities can have significant effects.

A repository of simulated synovial fluid compositions was tested using a reduced factorial approach (Taguchi method) where individual factors could be separated out in analysis and determined if they had a significant effect on response means and signal-to-noise (S/N) ratio. Cell behavior, solution characteristics and electrochemical response (DC and AC) were monitored in the presence of polished CoCrMo. It was found that certain components native to synovial fluid like hyaluronic acid (HA) and phospholipids (PL) dominated material and solution response, while others like Cr^{3+} and Co^{2+} ions did not. Solutions likely experienced

compounding molecular interactions that are unknown to our experimental results and the field of simulated joint fluid at this time. Moreover, ROS like H_2O_2 was found to significantly impact GSH activity, indicating a direct interaction between thiol regulation and exterior ROS concentrations. Using the information collected, we now have a comprehensive and predictable set of solutions that better simulate the periprosthetic joint setting.

This dissertation highlights the capabilities that exist within ROS detection and response, and this research provides methodology that can be implemented in ways not yet investigated or discussed. ROS are not thought of as the main instigator in the failure of biometallic devices or the inflammatory response, which is why the information presented here is critical for developing future considerations about the inflamed joint environment.

10. Future Work

The ubiquity of studying the inflamed joint space is that there will always be future work involving the characterization of molecules and material interactions. This dissertation has gone into detail reporting ROS production produced from cathodic excursions, the effects of ROS on cell and solution properties, and the electrochemical effects of ROS exposure. The future work stemming from this collected research could include fluorescently defining other individual ROS known to form during reduction reactions, continuation of the NEIS protocol and synthetic synovial fluid study, and integration of cell culture and tribological experiments.

10.1. Fluorescent Detection of Singlet Oxygen and Superoxide Anion

There are many ROS produced during the reduction of water and oxygen molecules. Our work explored the fluorescent detection of two of the most common ROS, hydroxyl radicals and hydrogen peroxide, yet there are several other ROS to consider including singlet oxygen ($^1O_2$) and superoxide anion ($O_2^{-\bullet}$). Singlet oxygen can be fluorescently detected in one of two ways, endoperoxide formation or chemiluminescence[73]. Recent groups have developed fluorescent probes for singlet oxygen traps using fluorescein fused with 9,10-diphenylanthracence, rather than singular 9,10-diphenylanthracence which relies on conventional absorbance measurements[83]. The former molecule has proven to be selective over other ROS including superoxide anion, hydrogen peroxide and nitric acid, and our group already has experience with fluorescein fluorescent intensity measurements and analysis. This approach is favorable compared to the reported chemiluminescent probes that are unsuitable in biosample fluorometric detection of singlet oxygen[204]. Recent reports of superoxide anion fluorescent detection have relied on similar methods that we utilized in H_2O_2 detection, where the ROS deprotects the

fluorophore, in this proposed case bis(2,4-dinitrobenzenesulfonyl)fluorescein, at a target linkage, leaving a highly fluorescent fluorescein endproduct[73]. The group that developed this probe stimulated neutrophils with phorbol myristate acetate (PMA) and measured cell produced superoxide anion[75]. The main issue that could arise from this method is that superoxide anion is highly reactive like hydroxyl radicals, and therefore not stable. This would require a similar approach to TA detection of hydroxyl radicals, where the probe is in solution during the electrochemical processes. The main issue that arose from TA detection was the electrochemical consumption of the fluorescent probe. One possible experimental protocol could be culturing cells in media with the fluorophore over a period of time, and then stimulating the cells with electrochemically tested media or shorter timescale trials directly in the electrochemical chamber (< 1 min). If the probe was to permeate the cell membrane, then perhaps it would be shielded to the electrochemical effects that consumed the HTA probe. Intracellular fluorescent detection methods should be explored with the possibility of simultaneously detecting multiple individual ROS using the dosimeters described or previously used (Chapter 4).

After developing probes for singlet oxygen and superoxide anion, we can then be able to plot and predict individual ROS concentrations as a function of voltage, time of applied potential, material tested, fretting, etc. With respect to cell culture work, it would also be helpful to determine which fluorescent molecules trigger the greatest drop in GSH activity. This would provide direct insight as to which molecule is directly impairing cell viability with the possibility of developing selectively scavenging ROS molecules to preserve normal cell functions.

10.2. *Continuation of NEIS*

The NEIS method has provided preliminary information about the damaging effects of electrocautery burns, ROS exposed CoCrMo discs, and a severely corroded CoCrMo neck taper. There are many more experiments where NEIS should be applied to add to our knowledge of surface heterogeneities. First, cells should be cultured in a concentrated area with NEIS performed over the covered area. This will help us understand how small-area cell populations influence resistive properties. This experiment should be performed across a range of potentials within the cell's 'electrochemical zone of viability'. This will address if the cells are actively and electrochemically affecting the oxide film/surface. The solution used in the NEIS should also vary between 1X PBS, FBS, and the synthetic joint fluid compositions. We hypothesize that the cells will respond differently to the synthetic joint fluid when plated on CoCrMo as opposed to the tissue culture plastic in addition to added presence of an applied potential.

NEIS should also be performed on alloys subjected to varying concentrations of other ROS, similar to the hydrogen peroxide submersion trials. Two potential physiologically relevant reactive species to include are hypochlorous acid (HClO)[137] and nitric oxide (NO). Kubacki detailed HClO produced from neutrophils in simulated inflammatory environments with an emphasis on corrosion and tribocorrosion behavior of CoCrMo alloys. From the background literature cited, we know of reports that detail the effects of NO on oxide film composition on CoCrMo alloys where it has been shown to increase the thickness through oxidation and nitration reactions[16].

10.3. *Continuation of Simulated Joint Fluid*

The Taguchi orthogonal array proved to be helpful in determining interacting effects within simulated joint fluid consisting of some of the most relevant species present like hyaluronic acid and albumin. The analysis helped determine which factors had a significant impact on cell and solution responses as well as direct current (DC) and alternating current (AC) responses. Equally important, the analysis also reported which factors did not have a significant effect on responses. Therefore, it would be useful for future work involving these solution sets to utilize reduced models for targeted responses. For example, only HA:PL and [Co^{2+}] significantly affected the cell viability measures. One possible experiment would be to create a range of solutions containing varying levels of only these two factors and/or testing cell viability across multiple cell types or co-cultures of cells. This would prove useful in determining which type of cells are more resistant to the main killing agents in synthetic synovial fluid, which cells lose viability first, if cells release specific cytokines/chemokines/chemotaxis in response to HA, PL and Co^{2+}, etc. It would also provide insight as to what specific concentrations (thresholds) of HA, PL, and Co^{2+} lead to abnormal cell behavior. This strategy could be applied to every response that triggered a significant effect on the means or S/N. Reduced models will be able to provide a more precise understanding of the effects of that specific factor that the comprehensive Taguchi model couldn't.

It is also suggested that perhaps the Taguchi model be re-evaluated for components used. We hypothesized that we would see more a response on cell behavior from the incorporation of ROS and metal ions, however it is likely that these molecules were interacting with the organic materials, effectively neutralizing the desired effects like cytotoxicity or GSH fluorescent

intensity. A similar Taguchi orthogonal array is recommended using either non-periprosthetic synovial fluid species (i.e. HA, PL, A, G) or different metal ions and/or ROS. This would be helpful in understanding which of these components has the greatest influence on cell behavior without competing solution interactions. It is known that metal ions with large *d*-orbitals and organic materials will form metal organic frameworks (MOFs)[33, 93], HA chains can be cleaved by many factors including ROS[167, 186, 188] and that protein-ligand bonds will release Cr proportional to the oxide film thickness over time[172]. It is likely that our Taguchi set-up experienced interacting variables of this nature during culturing of cells as well as during polarization scans, leading to decreased and insignificant effects.

Furthermore, a solution set of synthetic joint fluid should be tailored to represent multiple facets of clinically relevant joint fluid. Retrieved synovial joint fluid is classified under five categories: normal, noninflammatory, inflammatory, septic and hemorrhagic[61]. Each type is accompanied by unique classifying molecules like cytokines or specific organic molecule concentrations (See Chapter 7). Similar responses should be measured to test the validity of the solutions such as GSH activity, pH, HA molecular weight, pro-/anti-inflammatory cytokine assays, etc. Completion of this solution set would be invaluable to the advancement of *in vitro* testing a simulated inflamed joint.

10.4. Electrocautery-Cell Interactions

The results presented here in combination with those obtained in previous studies[137] highlight a form of surface damage that has yet to be extensively characterized or has had its importance conveyed to the biomedical and orthopaedic communities. This dissertation has simply reported the basic electrochemical affects immediately after a single electrocautery burn

in four different physiologically relevant conditions. It is theorized that the surgeons burn the surface multiple times during both primary and revision surgeries, with several incidents on retrievals located away from the articulating and bearing surfaces[72].

There are several experiments that can be performed that will help better visualize the damaging and early on-set corrosive conditions that are caused by electrosurgical techniques. First, it would be advantageous to record surface characteristics (oxide film composition) before and after electrocautery burns with the added measure of collecting debris is various conditions (dry, wet, etc.). This will further compliment that electrochemical data reported in this dissertation. Next, cell cultures (osteoblasts/macrophages) should be cultured on burns directly after plasma-arc exposure and in locations surrounding the burn. This will give a comparison as to the cell behavior and activity as a result of electrocautery damage. Parameters like cell viability, GSH intensity and pro-/anti-inflammatory cytokines should be monitored in accordance with distance, type of burn (coagulation, cutting, bipolar), length (time) of contact, etc. Cells should also be cultured on the surface during burns and various chemotaxis should be reported in an effort to better understand the cell signaling and transduction of electrocautery-induced inflammation.

We have merely reported the electrochemical properties following electrocautery techniques when in reality, the cell interactions are equally important to our understanding. It is not an exaggeration to state that we have just begun discovering the destructive effects of electrocautery, and we have reason to believe that the remnants and surface evidence from this technique will become more apparent in retrievals in studies to follow.

10.5. Cell-Tribology Interactions

The long coveted *in vitro* experiment in our field has been replicating the inflamed joint space using physiologically relevant concentrations of materials under normal cyclic loading conditions. There a lot of variables (not including cell or solution constituents) that could contribute to the material-solution interactions including CO_2 and O_2 content, temperature (solution and of the device from cyclic testing), ionic strength, osmolality, circulating blood and serum, load fluctuations/delays/amplitude from interrupted movement (walking/sitting/jumping), etc. All of these could contribute significantly to excessive or diminished ROS production and resulting cell behavior.

Many lab groups have developed tribology systems using pin-on-disc, rotating electrodes, and multi-ball fretting chambers. All have advantages and disadvantages depending on the intended response, however there is a serious gap in advancements towards incorporating cell culture and synthetic synovial fluid into these systems. There are several challenges that are presented with advancing these systems, however our lab possesses the capabilities to address these challenges systematically. For instance, our in-house custom tribology set-up can be placed within an incubator, which would address thermal and gas content-related issues (to an extent). Once a synthetic synovial fluid mimicking various types of inflammatory processes is developed, that can be incorporated within the pin-on-disc system. Cells can be cultured on the discs with real-time electrochemical properties controlled and measured. This stand-alone experiment would be much closer to *in situ* corrosive conditions than have been previously been studied within the lab. Additionally, the detection of ROS in the proposed experimental design would be more physiologically and clinically relevant than prior *in vitro* tribological experiments.

10.6. Summary

This dissertation has provided our lab and field with a variety of new techniques (fluorescent detection of ROS in the presence of an electrochemical bias, nearfield electrochemical impedance spectroscopy) as well as new approaches to existing gaps in knowledge (synovial fluid component interactions, electrochemical zone of viability). The protocols described in the various methods/appendices will provide the background needed to help achieve the proposed future work and will hopefully guide ROS characterization towards a more clinical setting.

References

1. Chen Q, Thouas GA. Metallic implant biomaterials. *Mater Sci Eng R Rep*. 2015; 87:1-57.

2. Mischler S, Debaud S, Landolt D. Wear-accelerated corrosion of passive metals in tribocorrosion systems. *J Electrochem Soc*. 1998; 145(3):750-8.

3. Granchi D, Savarino LM, Ciapetti G, Baldini N. Biological effects of metal degradation in hip arthroplasties. *Crit Rev Toxicol*. 2018; 48(2):170-93.

4. Woolf AD, Pfleger B. Burden of major musculoskeletal conditions. *Bull WHO*. 2003; 81(9):646-56.

5. Hallab NJ, Jacobs JJ. Biologic effects of implant debris. *Bull NYU Hosp Jt Dis*. 2009; 67(2):182-8.

6. Garvin KL, Konigsberg BS. Infection following total knee arthroplasty: prevention and management. *Instr Course Lect*. 2012; 61:411-9.

7. Sharkey PF, Lichstein PM, Shen C, Tokarski AT, Parvizi J. Why are total knee arthroplasties failing today-has anything changed after 10 years? *J Arthroplasty*. 2013; 29(9):1774-8.

8. Jacobs JJ, Gilbert JL, Urban RM. Corrosion of metal orthopaedic implants. *J Bone Jt Surg Ser A*. 1998; 80(2):268-82.

9. Coussens LM, Werb Z. Inflammation and cancer. *Nature*. 2002; 420(6917):860-7.

10. Singer AJ, Clark RAF. Cutaneous wound healing. *New Engl J Med*. 1999; 341(10):738-46.

11. Murray PJ, Wynn TA. Protective and pathogenic functions of macrophage subsets. *Nat Rev Immunol*. 2011; 11(11):723-37.

12. Anderson JM, Rodriguez A, Chang DT. Foreign body reaction to biomaterials. *Semin Immunol*. 2008; 20(2):86-100.

13. Kinov P, Leithner A, Radl R, et al. Role of free radicals in aseptic loosening of hip arthroplasty. *J Orthop Res*. 2006; 24(1):55-62.

14. Gilbert JL, Sivan S, Liu Y, Kocagöz SB, Arnholt CM, Kurtz SM. Direct in vivo inflammatory cell-induced corrosion of CoCrMo alloy orthopedic implant surfaces. *J Biomed Mater Res Part A*. 2015; 103(1):211-23.

15. Di Laura A, Hothi HS, Meswania JM, et al. Clinical relevance of corrosion patterns attributed to inflammatory cell-induced corrosion: A retrieval study. *J Biomed Mater Res Part B Appl Biomater*. 2017; 105(1):155-64.

16. Lin H-, Bumgardner JD. In vitro biocorrosion of Co-Cr-Mo implant alloy by macrophage cells. *J Orthop Res*. 2004; 22(6):1231-6.

17. Peng K-, Hsu W-, Shih H-, et al. The role of reactive oxygen species scavenging enzymes in the development of septic loosening after total hip replacement. *J Bone Jt Surg Ser B*. 2011; 93 B(9):1201-9.

18. Cadosch D, Chan E, Gautschi OP, Simmen H-, Filgueira L. Bio-corrosion of stainless steel by osteoclasts-in vitro evidence. *J Orthop Res*. 2009; 27(7):841-6.

19. Anderson JA, Lamichhane S, Mani G. Macrophage responses to 316L stainless steel and cobalt chromium alloys with different surface topographies. *J Biomed Mater Res Part A*. 2016; 104(11):2658-72.

20. Hodgson AWE, Kurz S, Virtanen S, Fervel V, Olsson C-A, Mischler S. Passive and transpassive behaviour of CoCrMo in simulated biological solutions. *Electrochim Acta*. 2004; 49(13):2167-78.

21. Papageorgiou I, Brown C, Schins R, et al. The effect of nano- and micron-sized particles of cobalt-chromium alloy on human fibroblasts in vitro. *Biomaterials*. 2007; 28(19):2946-58.

22. Altaf H, Revell PA. Evidence for active antigen presentation by monocyte/macrophages in response to stimulation with particles: The expression of NFκB transcription factors and costimulatory molecules. *Inflammopharmacology*. 2013; 21(4):279-90.

23. Steinbeck MJ, Jablonowski LJ, Parvizi J, Freeman TA. The Role of Oxidative Stress in Aseptic Loosening of Total Hip Arthroplasties. *J Arthroplasty*. 2014; 29(4):843-9.

24. Mostardi RA, Pentello A, Kovacik MW, Askew MJ. Prosthetic metals have a variable necrotic threshold in human fibroblasts: An in vitro study. *J Biomed Mater Res*. 2002; 59(4):605-10.

25. Figgitt M, Newson R, Leslie IJ, Fisher J, Ingham E, Case CP. The genotoxicity of physiological concentrations of chromium (Cr(III) and Cr(VI)) and cobalt (Co(II)): An in vitro study. *Mutat Res Fundam Mol Mech Mutagen*. 2010; 688(1-2):53-61.

26. Scharf B, Clement CC, Zolla V, et al. Molecular analysis of chromium and cobalt-related toxicity. *Sci Rep*. 2014; 4.

27. Stohs SJ, Bagchi D. Oxidative mechanisms in the toxicity of metal ions. *Free Radic Biol Med*. 1995; 18(2):321-36.

28. Tkaczyk C, Huk OL, Mwale F, et al. Effect of chromium and cobalt ions on the expression of antioxidant enzymes in human U937 macrophage-like cells. *J Biomed Mater Res Part A*. 2010; 94(2):419-25.

29. Petit A, Mwale F, Tkaczyk C, Antoniou J, Zukor DJ, Huk OL. Induction of protein oxidation by cobalt and chromium ions in human U937 macrophages. *Biomaterials*. 2005; 26(21):4416-22.

30. G M Keegan, I D Learmonth, C P Case. Orthopaedic metals and their potential toxicity in the arthroplasty patient: A review of current knowledge and future strategies. *The Journal of bone and joint surgery. British volume*. 2007; 89(5): p. 567-73.

31. Kzhyshkowska J, Gudima A, Riabov V, Dollinger C, Lavalle P, Vrana NE. Macrophage responses to implants: Prospects for personalized medicine. *J Leukocyte Biol*. 2015; 98(6):953-62.

32. Dickinson BC, Chang CJ. Chemistry and biology of reactive oxygen species in signaling or stress responses. *Nat Chem Biol*. 2011; 7(8):504-11.

33. Barreto JC, Smith GS, Strobel NHP, McQuillin PA, Miller TA. Terephthalic acid: A dosimeter for the detection of hydroxyl radicals in vitro. *Life Sci*. 1994; 56(4):PL8-PL96.

34. Forman HJ, Torres M. Reactive oxygen species and cell signaling: Respiratory burst in macrophage signaling. *Am J Respir Crit Care Med*. 2002; 166(12 II):S-S8.

35. Ying W. NAD+/NADH and NADP+/NADPH in cellular functions and cell death: Regulation and biological consequences. *Antioxid Redox Signal*. 2008; 10(2):179-206.

36. Mittal M, Siddiqui MR, Tran K, Reddy SP, Malik AB. Reactive oxygen species in inflammation and tissue injury. *Antioxid Redox Signal*. 2014; 20(7):1126-67.

37. Finkel T. Signal transduction by reactive oxygen species. *J Cell Biol*. 2011; 194(1):7-15.

38. Bedard K, Krause K-. The NOX family of ROS-generating NADPH oxidases: Physiology and pathophysiology. *Physiol Rev*. 2007; 87(1):245-313.

39. Segal AW. The function of the NADPH oxidase of phagocytes and its relationship to other NOXs in plants, invertebrates, and mammals. *Int J Biochem Cell Biol*. 2008; 40(4):604-18.

40. Gilbert JL, Zarka L, Chang E, Thomas CH. The reduction half cell in biomaterials corrosion: Oxygen diffusion profiles near and cell response to polarized titanium surfaces. *J Biomed Mater Res*. 1998; 42(2):321-30.

41. Ozmen I, Naziroglu M, Okutan R. Comparative study of antioxidant enzymes in tissues surrounding implant in rabbits. *Cell Biochem Funct*. 2006; 24(3):275-81.

42. Ehrensberger MT, Gilbert JL. A time-based potential step analysis of electrochemical impedance incorporating a constant phase element: A study of commercially pure titanium in phosphate buffered saline. *J Biomed Mater Res Part A*. 2010; 93(2):576-84.

43. Contu F, Elsener B, Böhni H. A study of the potentials achieved during mechanical abrasion and the repassivation rate of titanium and Ti6Al4V in inorganic buffer solutions and bovine serum. *Electrochim Acta*. 2004; 50(1):33-41.

44. Sivan S, Kaul S, Gilbert JL. The effect of cathodic electrochemical potential of Ti-6Al-4V on cell viability: Voltage threshold and time dependence. *J Biomed Mater Res Part B Appl Biomater*. 2013; 101(8):1489-97.

45. Haeri M, Wöllert T, Langford GM, Gilbert JL. Electrochemical control of cell death by reduction-induced intrinsic apoptosis and oxidation-induced necrosis on CoCrMo alloy in vitro. *Biomaterials*. 2012; 33(27):6295-304.

46. Haeri M, Gilbert JL. Study of cellular dynamics on polarized CoCrMo alloy using time-lapse live-cell imaging. *Acta Biomater*. 2013; 9(11):9220-8.

47. Kalbacova M, Roessler S, Hempel U, et al. The effect of electrochemically simulated titanium cathodic corrosion products on ROS production and metabolic activity of osteoblasts and monocytes/macrophages. *Biomaterials*. 2007; 28(22):3263-72.

48. Bearinger JP, Orme CA, Gilbert JL. Effect of hydrogen peroxide on titanium surfaces: In situ imaging and step-polarization impedance spectroscopy of commercially pure titanium and titanium, 6-aluminum, 4-vanadium. *J Biomed Mater Res Part A*. 2003; 67(3):702-12.

49. Brooks EK, Brooks RP, Ehrensberger MT. Effects of simulated inflammation on the corrosion of 316L stainless steel. *Mater Sci Eng C*. 2017; 71:200-5.

50. Liu Y, Gilbert JL. The effect of simulated inflammatory conditions and pH on fretting corrosion of CoCrMo alloy surfaces. *Wear*. 2017; 390-391:302-11.

51. Montague A, Merritt K, Brown S, Payer J. Effects of Ca and H2O2 added to RPMI on the fretting corrosion of Ti6Al4V. *J Biomed Mater Res*. 1996; 32(4):519-26.

52. Lin H-, Bumgardner JD. Changes in surface composition of the Ti-6Al-4V implant alloy by cultured macrophage cells. *Appl Surf Sci*. 2004; 225(1-4):21-8.

53. Lin H-, Bumgardner JD. Changes in the surface oxide composition of Co-Cr-Mo implant alloy by macrophage cells and their released reactive chemical species. *Biomaterials*. 2004; 25(7-8):1233-8.

54. Lord MS, Jung M, Teoh WY, et al. Cellular uptake and reactive oxygen species modulation of cerium oxide nanoparticles in human monocyte cell line U937. *Biomaterials*. 2012; 33(31):7915-24.

55. Martin P, Leibovich SJ. Inflammatory cells during wound repair: The good, the bad and the ugly. *Trends Cell Biol*. 2005; 15(11):599-607.

56. Kawamura T, Kondoh Y, Muroi M, Kawatani M, Osada H. A small molecule that induces reactive oxygen species via cellular glutathione depletion. *Biochem J*. 2014; 463(1):53-63.

57. Tuncay OC, Ho D, Barker MK. Oxygen tension regulates osteoblast function. *Am J Orthod Dentofacial Orthop*. 1994; 105(5):457-63.

58. Pilas B, Sarna T, Kalyanaraman B, Swartz HM. The effect of melanin on iron associated decomposition of hydrogen peroxide. *Free Radic Biol Med*. 1988; 4(5):285-93.

59. Qu X, Kirschenbaum LJ, Borish ET. Hydroxyterephthalate as a fluorescent probe for hydroxyl radicals: Application to hair melanin. *Photochem Photobiol*. 2000; 71(3):307-13.

60. Goldring MB, Otero M. Inflammation in osteoarthritis. *Curr Opin Rheumatol*. 2011; 23(5):471-8.

61. Jacques D, Cauzinille L, Bouvy B, Dupre G. A retrospective study of 40 dogs with polyarthritis. *Vet Surg*. 2002; 31(5):428-34.

62. Circu ML, Aw TY. Glutathione and modulation of cell apoptosis. *Biochim Biophys Acta Mol Cell Res*. 2012; 1823(10):1767-77.

63. Troyano A, Sancho P, Fernández C, de Blas E, Bernardi P, Aller P. The selection between apoptosis and necrosis is differentially regulated in hyrdrogen peroxide-treated and glutathione-depleted human promonocytic cells. *Cell Death Differ*. 2003; 10(8):889-98.

64. D'Alessio M, C Cerella, M De Nicola, et al. Apoptotic GSH Extrusion Is Associated with Free Radical Generation. *Ann New York Acad Sci*. 2003; 1010.

65. Kiefer KM, O'Brien TD, Pluhar EG, Conzemius M. Canine adipose-derived stromal cell viability following exposure to synovial fluid from osteoarthritic joints. *Veterinary Record Open*. 2015; 2(1).

66. Lalaouni A, Henderson C, Kupper C, Grant MH. The interaction of chromium (VI) with macrophages: Depletion of glutathione and inhibition of glutathione reductase. *Toxicology*. 2007; 236(1-2):76-81.

67. Li Y, Meunier A, Fulcrand R, et al. Multi-chambers Microsystem for Simultaneous and Direct Electrochemical Detection of Reactive Oxygen and Nitrogen Species Released by Cell Populations. *Electroanalysis*. 2016; 28(8):1865-72.

68. Forman HJ, Fukuto JM, Torres M. Redox signaling: Thiol chemistry defines which reactive oxygen and nitrogen species can act as second messengers. *Am J Physiol Cell Physiol*. 2004; 287(2 56-2):C24-C256.

69. Wardman P. Fluorescent and luminescent probes for measurement of oxidative and nitrosative species in cells and tissues: Progress, pitfalls, and prospects. *Free Radic Biol Med*. 2007; 43(7):995-1022.

70. Revell PA. The combined role of wear particles, macrophages and lymphocytes in the loosening of total joint prostheses. *J R Soc Interface*. 2008; 5(28):1263-78.

71. Arnholt CM, MacDonald DW, Malkani AL, et al. Corrosion Damage and Wear Mechanisms in Long-Term Retrieved CoCr Femoral Components for Total Knee Arthroplasty. *J Arthroplasty*. 2016; 31(12):2900-6.

72. Kubacki GW, Sivan S, Gilbert JL. Electrosurgery Induced Damage to Ti-6Al-4V and CoCrMo Alloy Surfaces in Orthopedic Implants In Vivo and In Vitro. *J Arthroplasty*. 2017; 32(11):3533-8.

73. Soh N. Recent advances in fluorescent probes for the detection of reactive oxygen species. *Anal Bioanal Chem*. 2006; 386(3):532-43.

74. Wang LP, Yu L, Srinivasan M, Xu ZJ, Wang X. Recent developments in electrode materials for sodium-ion batteries. *J Mater Chem A*. 2015; 3(18):9353-78.

75. Maeda H, Fukuyasu Y, Yoshida S, et al. Fluorescent probes for hydrogen peroxide based on a non-oxidative mechanism. *Angew Chem Int Ed*. 2004; 43(18):2389-91.

76. Swaminathan V, Gilbert JL. Fretting corrosion of CoCrMo and Ti6Al4V interfaces. *Biomaterials*. 2012; 33(22):5487-503.

77. Ehrensberger MT, Sivan S, Gilbert JL. Titanium is not "the most biocompatible metal" under cathodic potential: The relationship between voltage and MC3T3 preosteoblast behavior on electrically polarized cpTi surfaces. *J Biomed Mater Res Part A*. 2010; 93(4):1500-9.

78. Dhar HP, JO Bockris, DH Lewis. Cathodic electrochemical process for preventing or retarding microbial and calcerous fouling
. 1984; 328,853(4,440,611): p. 1-10.

79. Murphy MP. How mitochondria produce reactive oxygen species. *Biochem J*. 2009; 417(1):1-13.

80. Quillet-Mary A, Jaffrézou J-, Mansat V, Bordier C, Naval J, Laurent G. Implication of mitochondrial hydrogen peroxide generation in ceramide- induced apoptosis. *J Biol Chem*. 1997; 272(34):21388-95.

81. Wang ML, Hauschka PV, Tuan RS, Steinbeck MJ. Exposure to particles stimulates superoxide production by human THP-1 macrophages and A vian HD-11EM osteoclasts activated by tumor necrosis factor-a and PMA. *J Arthroplasty*. 2002; 17(3):335-46.

82. Hassanzadeh J, Amjadi M. Sensitive and selective determination of fluvoxamine maleate using a sensitive chemiluminescence system based on the alkaline permanganate-Rhodamine B-gold nanoparticles reaction. *Lumin*. 2015; 30(4):439-43.

83. Umezawa N, Tanaka K, Urano Y, Kikuchi K, Higuchi T, Nagano T. Novel fluorescent probes for singlet oxygen. *Angew Chem Int Ed*. 1999; 38(19):2899-901.

84. Maeda H, Yamamoto K, Nomura Y, et al. A design of fluorescent probes for superoxide based on a nonredox mechanism. *J Am Chem Soc*. 2005; 127(1):68-9.

85. Brenner S, Gülden M, Maser E, Seibert H. Lasting effect of preceding culture conditions on the susceptibility of C6 cells to peroxide-induced oxidative stress. *Toxicol Vitro*. 2010; 24(8):2090-6.

86. Schraufstatter IU, Hyslop PA, Hinshaw DB, Spragg RG, Sklar LA, Cochrane CG. Hydrogen peroxide-induced injury of cells and its prevention by inhibitors of poly(ADP-ribose) polymerase. *Proc Natl Acad Sci U S A*. 1986; 83(13):4908-12.

87. Wiegand MJ, Kubacki GW, Gilbert JL. Electrochemical potential zone of viability on CoCrMo surfaces is affected by cell type: Macrophages under cathodic bias are more resistant to killing. *J Biomed Mater Res Part A*. 2019; 107(3):526-34.

88. Armstrong WA, Grant DW. A highly sensitive chemical dosimeter for ionizing radiation. *Nature*. 1958; 182(4637):747.

89. Fang X, Mark G, Von Sonntag C. OH radical formation by ultrasound in aqueous solutions: Part I: The chemistry underlying the terephthalate dosimeter. *Ultrason Sonochem*. 1996; 3(1):57-63.

90. Sahni M, Locke BR. Quantification of hydroxyl radicals produced in aqueous phase pulsed electrical discharge reactors. *Ind Eng Chem Res*. 2006; 45(17):5819-25.

91. Tang B, Zhang L, Geng Y. Determination of the antioxidant capacity of different food natural products with a new developed flow injection spectrofluorimetry detecting hydroxyl radicals. *Talanta*. 2005; 65(3):769-75.

92. Hassanzadeh J, Khataee A, Eskandari H. Encapsulated cholesterol oxidase in metal-organic framework and biomimetic Ag nanocluster decorated MoS2 nanosheets for sensitive detection of cholesterol. *Sens Actuators, B Chem*. 2018; 259:402-10.

93. Liu Y, Gao P, Huang C, Li Y. Shape- and size-dependent catalysis activities of iron-terephthalic acid metal-organic frameworks. *Sci China Chem*. 2015; 58(10):1553-60.

94. Zhao L, Zhao J, Hu Y-, et al. Disodium terephthalate (NA2C8H4O4) as high performance anode material for low-cost room-temperature sodium-ion battery. *Adv Energy Mater*. 2012; 2(8):962-5.

95. Schröck K, Lutz J, Mändl S, Hacker MC, Kamprad M, Schulz-Siegmund M. Co(II)-mediated effects of plain and plasma immersion ion implanted cobalt-chromium alloys on the osteogenic differentiation of human mesenchymal stem cells. *J Orthop Res*. 2015; 33(3):325-33.

96. Swaminathan V, Gilbert JL. Potential and frequency effects on fretting corrosion of Ti6Al4V and CoCrMo surfaces. *J Biomed Mater Res Part A*. 2013; 101 A(9):2602-12.

97. Schoenenberger AD, Schipanski A, Malheiro V, et al. Macrophage Polarization by Titanium Dioxide (TiO2) Particles: Size Matters. *ACS Biomater Sci Eng*. 2016; 2(6):908-19.

98. Posada OM, Tate RJ, Grant MH. Effects of CoCr metal wear debris generated from metal-on-metal hip implants and Co ions on human monocyte-like U937 cells. *Toxicol Vitro*. 2015; 29(2):271-80.

99. Queally JM, Devitt BM, Butler JS, et al. Cobalt ions induce chemokine secretion in primary human osteoblasts. *J Orthop Res*. 2009; 27(7):855-64.

100. Miki M, Morita M. Evaluation of the biocompatibility of a Ti-Ta-Sn alloy using cell cultures. *Mater Trans*. 2015; 56(7):1087-91.

101. Granchi D, Ciapetti G, Stea S, et al. Cytokine release in mononuclear cells of patients with Co-Cr hip prosthesis. *Biomaterials*. 1999; 20(12):1079-86.

102. Nygaard M, Elling F, Bastholm L, Søballe K, Borgwardt A. No difference in early cellular response of the pseudo-synovial membrane after total hip arthroplasty: Comparison of 3 combinations of bearing materials. *Acta Orthop*. 2006; 77(3):402-12.

103. Tan HC, Poh CK, Cai Y, Soe MT, Wang W. Covalently grafted BMP-7 peptide to reduce macrophage/monocyte activity: An in vitro study on cobalt chromium alloy. *Biotechnol Bioeng*. 2013; 110(3):969-79.

104. Jäger M, Zilkens C, Zanger K, Krauspe R. Significance of nano- and microtopography for cell-surface interactions in orthopaedic implants. *J Biomed Biotechnol*. 2007; 2007.

105. Pirmohamed T, Dowding JM, Singh S, et al. Nanoceria exhibit redox state-dependent catalase mimetic activity. *Chem Commun*. 2010; 46(16):2736-8.

106. Dröge W. Free radicals in the physiological control of cell function. *Physiol Rev*. 2002; 82(1):47-95.

107. Bockris JO. The Electrocatalysis of Oxygen Evolution on Perovskites. *J Electrochem Soc*. 1984; 131(2):290-302.

108. Hall DJ, Pourzal R, Lundberg HJ, Mathew MT, Jacobs JJ, Urban RM. Mechanical, chemical and biological damage modes within head-neck tapers of CoCrMo and Ti6Al4V contemporary hip replacements. *J Biomed Mater Res Part B Appl Biomater*. 2017.

109. Christenson EM, Anderson JM, Hiltner A. Biodegradation mechanisms of polyurethane elastomers? *Corros Eng Sci Technol*. 2007; 42(4):312-23.

110. Wiggins MJ, Wilkoff B, Anderson JM, Hiltner A. Biodegradation of polyether polyurethane inner insulation in bipolar pacemaker leads. *J Biomed Mater Res*. 2001; 58(3):302-7.

111. Moungjaroen J, Nimmannit U, Callery PS, et al. Reactive oxygen species mediate caspase activation and apoptosis induced by lipoic acid in human lung epithelial cancer cells through Bcl-2 down-regulation. *J Pharmacol Exp Ther*. 2006; 319(3):1062-9.

112. Gilbert JL, Mali SA, Liu Y. Area-dependent impedance-based voltage shifts during tribocorrosion of Ti-6Al-4V biomaterials: Theory and experiment. *Surf Topogr Metrol Prop*. 2016; 4(3).

113. Tsaryk R, Peters K, Barth S, Unger RE, Scharnweber D, Kirkpatrick CJ. The role of oxidative stress in pro-inflammatory activation of human endothelial cells on Ti6Al4V alloy. *Biomaterials*. 2013; 34(33):8075-85.

114. Seok HH, Jeong J, Shim S, et al. Effect of electric currents on bacterial detachment and inactivation. *Biotechnol Bioeng*. 2008; 100(2):379-86.

115. Cohen MD, Kargacin B, Klein CB, Costa M. Mechanisms of chromium carcinogenicity and toxicity. *Crit Rev Toxicol*. 1993; 23(3):255-81.

116. Zang L, He H, Xu Q, et al. Reactive oxygen species H2O2 and OH, but not O 2- promote oridonin-induced phagocytosis of apoptotic cells by human histocytic lymphoma U937 cells. *Int Immunopharmacol*. 2013; 15(2):414-23.

117. Martindale JL, Holbrook NJ. Cellular response to oxidative stress: Signaling for suicide and survival. *J Cell Physiol*. 2002; 192(1):1-15.

118. Rosen GM, Pou S, Ramos CL, Cohen MS, Britigan BE. Free radicals and phagocytic cells. *FASEB J*. 1995; 9(2):200-9.

119. De Nicola M, Ghibelli L. Glutathione depletion in survival and apoptotic pathways. *Front Pharmacol*. 2014; 5(NOV).

120. Shan X, Aw TY, Shapira R, Jones DP. Oxygen dependence of glutathione synthesis in hepatocytes. *Toxicol Appl Pharmacol*. 1989; 101(2):261-70.

121. Kharroubi W, Nury T, Ahmed SH, et al. Induction by arsenate of cell-type-specific cytotoxic effects in nerve and hepatoma cells. *Hum Exp Toxicol*. 2017; 36(12):1256-69.

122. Caputo F, Mameli M, Sienkiewicz A, et al. A novel synthetic approach of cerium oxide nanoparticles with improved biomedical activity. *Sci Rep*. 2017; 7(1).

123. Bao X, Cui J, Wu Y, et al. The roles of endogenous reactive oxygen species and nitric oxide in triptolide-induced apoptotic cell death in macrophages. *J Mol Med*. 2007; 85(1):85-98.

124. Nury T, Zarrouk A, Ragot K, et al. 7-Ketocholesterol is increased in the plasma of X-ALD patients and induces peroxisomal modifications in microglial cells: Potential roles of 7-ketocholesterol in the pathophysiology of X-ALD. *J Steroid Biochem Mol Biol*. 2017; 169:123-36.

125. Park JE, Yang J-, Yoon SJ, Lee J-, Yang ES, Park J-. Lipid peroxidation-mediated cytotoxicity and DNA damage in U937 cells. *Biochimie*. 2002; 84(12):1199-205.

126. Kane DJ, Sarafian TA, Anton R, et al. Bcl-2 inhibition of neural death: Decreased generation of reactive oxygen species. *Science*. 1993; 262(5137):1274-7.

127. Parker SH, Lin H-, Zardiackas LD, Bumgardner JD. Influence of macrophage cells on 316L stainless steel corrosion. In: *ASTM Special Technical Publication*; 2002, p. 137-53.

128. Jennette KW. Chromate metabolism in liver microsomes. *Biol Trace Elem Res*. 1979; 1(1):55-62.

129. Goldberg JR, Gilbert JL. The electrochemical and mechanical behavior of passivated and TiN/AlN-coated CoCrMo and Ti6Al4V alloys. *Biomaterials*. 2004; 25(5):851-64.

130. Bearinger JP, Orme CA, Gilbert JL. In situ imaging and impedance measurements of titanium surfaces using AFM and SPIS. *Biomaterials*. 2003; 24(11):1837-52.

131. Fischer A, Janssen D, Wimmer MA. The Influence of Molybdenum on the Fretting Corrosion Behavior of CoCr/TiAlV Couples. *Biotribology*. 2017; 11:8-19.

132. Antunes RA, de Oliveira, Mara Cristina Lopes. Corrosion fatigue of biomedical metallic alloys: Mechanisms and mitigation. *Acta Biomaterialia*. 2012; 8(3):937-62.

133. Arenas MA, Conde A, Damborenea Jd. The role of mechanically activated area on tribocorrosion of CoCrMo.

134. Haeri M, Goldberg S, Gilbert JL. The voltage-dependent electrochemical impedance spectroscopy of CoCrMo medical alloy using time-domain techniques: Generalized Cauchy-Lorentz, and KWW-Randles functions describing non-ideal interfacial behaviour. *Corros Sci*. 2011; 53(2):582-8.

135. Wiegand MJ, Benton TZ, Gilbert JL. A fluorescent approach for detecting and measuring reduction reaction byproducts

near cathodically-biased metallic surfaces: Reactive oxygen species production and quantification *Bioelectrochemistry*. In-press.

136. Yuan N, Park S-, Luck JV, Jr., Campbell PA. Revisiting the concept of inflammatory cell-induced corrosion. *J Biomed Mater Res Part B Appl Biomater*. 2018; 106(3):1148-55.

137. Kubacki GW. Simulated Inflammation by Hypochlorous Acid and the Corrosion and Tribocorrosion of Orthopedic Alloys: Feedback between Corrosion and Inflammation: ProQuest Dissertations Publishing; 2018.

138. Mierisch AM. Probing Coating Degradation on AA2024-T3 Using Local Electrochemical and Chemical Techniques. *Journal of The Electrochemical Society*. 1999; 146(12):4449.

139. Darowicki K, Szociński M, Zieliński A. Assessment of organic coating degradation via local impedance imaging. *Electrochimica Acta*. 2010; 55(11):3741-8.

140. Dunne CF, Levy GK, Hakimi O, Aghion E, Twomey B, Stanton KT. Corrosion behaviour of biodegradable magnesium alloys with hydroxyapatite coatings. *Surface & Coatings Technology*. 2016; 289:37-44.

141. Sinebryukhov SL, Gnedenkov AS, Mashtalyar DV, Gnedenkov SV. PEO-coating/substrate interface investigation by localised electrochemical impedance spectroscopy. *Surf Coat Technol*. 2010; 205(6):1697-701.

142. Igual Muñoz A, Casabán Julián L. Influence of electrochemical potential on the tribocorrosion behaviour of high carbon CoCrMo biomedical alloy in simulated body fluids by electrochemical impedance spectroscopy. *Electrochim Acta*. 2010; 55(19):5428-39.

143. Li W, Chen X, Chen B. Effect of aging on the corrosion behavior of 6005 Al alloys in 3.5 wt% NaCl aqueous solution. *J Mater Res*. 2018; 33(12):1830-8.

144. Goldberg JR, Gilbert JL, Jacobs JJ, Bauer TW, Paprosky W, Leurgans S. A multicenter retrieval study of the taper interfaces of modular hip prostheses. *Clin Orthop Relat Res*. 2002(401):149-61.

145. Hu S. Development of a localized electrochemical properties test method: A study of CoCrMo and Ti alloy localized electrochemical behavior: Syracuse University; 2017.

146. Frateur I, Huang VM, Orazem ME, Pébère N, Tribollet B, Vivier V. Local electrochemical impedance spectroscopy: Considerations about the cell geometry. *Electrochimica Acta*. 2008; 53(25):7386-95.

147. Diem CB, Newman B. The Influence of Small Machining Errors on the Primary Current Distribution at a Recessed Electrode. *J Electrochem Soc*. 1988; 135(10):2524-30.

148. Su Y, Shih C, Chen L, Shih C, Lin S. Heterogeneous surface properties on wallstents. *Surface and Interface Analysis*. 2009:n/a.

149. Indira K, Nishimura T. In Situ Study of Effect of Chromium Content and Epoxy Coating on Localized Corrosion Behavior of Low-Alloy Steel Using Localized Electrochemical Impedance Spectroscopy. *J Bio Tribo Corros*. 2017; 3(3):1-13.

150. Balusamy T, Nishimura T. In-Situ Monitoring of Local Corrosion Process of Scratched Epoxy Coated Carbon Steel in Simulated Pore Solution Containing Varying percentage of Chloride ions by Localized Electrochemical Impedance Spectroscopy. *Electrochimica Acta*. 2016; 199:305-13.

151. Zou F, D Thierry. Localized electrochemical impedance spectroscopy for studying the degradation of organic coatings. *Electrochimica Acta*. 1997; 42(20): p. 3293-301.

152. Bayet E, Huet F, Keddam M, Ogle K, Takenouti H. A novel way of measuring local electrochemical impedance using a single vibrating probe. *J Electrochem Soc*. 1997; 144(4):L8-L90.

153. Wittmann MW, Leggat RB, Taylor SR. Detection and mapping of defects in organic coatings using local electrochemical impedance methods. *J Electrochem Soc*. 1999; 146(11):4071-5.

154. Zhong C, Tang X, Cheng YF. Corrosion of steel under the defected coating studied by localized electrochemical impedance spectroscopy. *Electrochimica Acta*. 2008; 53(14):4740-7.

155. Annergren I, Thierry D, Zou F. Localized electrochemical impedance spectroscopy for studying pitting corrosion on stainless steels. *J Electrochem Soc*. 1997; 144(4):1208-15.

156. Baril G, Blanc C, Keddam M, Pébère N. Local Electrochemical Impedance Spectroscopy Applied to the Corrosion Behavior of an AZ91 Magnesium Alloy. *J Electrochem Soc*. 2003; 150(10):B48-B493.

157. Estey MP, Diamandis EP, Van Straeten CD, Tower SS, Hart AJ, Moyer TP. Cobalt and chromium measurement in patients with metal hip prostheses. *Clin Chem*. 2013; 59(6):880-6.

158. Sansone V, Pagani D, Melato M. The effects on bone cells of metal ions released from orthopaedic implants. A review. *Clin Cases Miner Bone Metab*. 2013; 10(1):34-40.

159. Chyr A, Qiu M, Speltz JW, Jacobsen RL, Sanders AP, Raeymaekers B. A patterned microtexture to reduce friction and increase longevity of prosthetic hip joints. *Wear*. 2014; 315(1-2):51-7.

160. Cook RB, Bolland, B. J. R. F., Wharton JA, Tilley S, Latham JM, Wood RJK. Pseudotumour formation due to tribocorrosion at the taper interface of large diameter metal on polymer modular total hip replacements. *J Arthroplasty*. 2013; 28(8):1430-6.

161. Jay GD, Waller KA. The biology of Lubricin: Near frictionless joint motion. *Matrix Biology*. 2014; 39:17-24.

162. Tamer Mahmoud Tamer. Hyaluronan and synovial joint: function, distribution and healing. *Interdisciplinary Toxicology*. 2013; 6(3):111-25.

163. Jung S, Petelska A, Beldowski P, et al. Hyaluronic acid and phospholipid interactions useful for repaired articular cartilage surfaces—a mini review toward tribological surgical adjuvants. *Colloid Polym Sci*. 2017; 295(3):403-12.

164. Lass R, Grübl A, Kolb A, et al. Comparison of synovial fluid, urine, and serum ion levels in metal-on-metal total hip arthroplasty at a minimum follow-up of 18 years. *Journal of Orthopaedic Research*. 2014; 32(9):1234-40.

165. De Smet K, De Haan R, Calistri A, et al. Metal Ion Measurement as a Diagnostic Tool to Identify Problems with Metal-on-Metal Hip Resurfacing. *The Journal of bone and joint surgery. American volume*. 2008; 90 Suppl 4(Suppl 4):202-8.

166. Castor CW, Prince RK, Hazelton MJ. Hyaluronic acid in human synovial effusions; A sensitive indicator of altered connective tissue cell function during inflammation. *Arthritis Rheum*. 1966; 9(6):783-94.

167. Balazs EA, Watson D, Duff IF, Roseman S. Hyaluronic acid in synovial fluid. I. Molecular parameters of hyaluronic acid in normal and arthritic human fluids. *Arthritis Rheum*. 1967; 10(4):357-76.

168. Bowman S, Awad M, Hamrick M, Hunter M, Fulzele S. Recent advances in hyaluronic acid based therapy for osteoarthritis. *Clin Trans Med*. 2018; 7(1):1-11.

169. Musumeci G. The role of lubricin in normal and pathological joint tissue: A contemporary review. *OA Anatomy*. 2013; 1(1).

170. Harsha AP, Joyce TJ. Challenges associated with using bovine serum in wear testing orthopaedic biopolymers. *Proceedings of the Institution of Mechanical Engineers, Part H: Journal of Engineering in Medicine*. 2011; 225(10):948-58.

171. Igual Munoz A, Schwiesau J, Jolles BM, Mischler S. In vivo electrochemical corrosion study of a CoCrMo biomedical alloy in human synovial fluids. *Acta Biomater*. 2015; 21:228-36.

172. Lewis AC, Kilburn MR, Papageorgiou I, Allen GC, Case CP. Effect of synovial fluid, phosphate-buffered saline solution, and water on the dissolution and corrosion properties of

CoCrMo alloys as used in orthopedic implants. *Journal of Biomedical Materials Research Part A*. 2005; 73A(4):456-67.

173. Muñoz AI, Mischler S. Interactive Effects of Albumin and Phosphate Ions on the Corrosion of CoCrMo Implant Alloy. *Journal of The Electrochemical Society*. 2007; 154(10):C562.

174. Yan Y, Neville A, Dowson D. Tribo-corrosion properties of cobalt-based medical implant alloys in simulated biological environments. *Wear*. 2007; 263(7):1105-11.

175. Andrews, Rebecca E.|Shah, Karan M.|Wilkinson, J. Mark|Gartland, Alison. Effects of cobalt and chromium ions at clinically equivalent concentrations after metal-on-metal hip replacement on human osteoblasts and osteoclasts: Implications for skeletal health. *Bone*. 2011; 49(4):717-23.

176. Davda K, Lali FV, Sampson B, Skinner JA, Hart AJ. An analysis of metal ion levels in the joint fluid of symptomatic patients with metal-on-metal hip replacements. *The Journal of bone and joint surgery. British volume*. 2011; 93(6):738-45.

177. Reito A, Parkkinen J, Puolakka T, Pajamäki J, Eskelinen A. Diagnostic utility of joint fluid metal ion measurement for histopathological findings in metal-on-metal hip replacements. *BMC musculoskeletal disorders*. 2015; 16(1):393.

178. Ghalme S, Mankar A, Bhalerao Y. Integrated Taguchi-simulated annealing (SA) approach for analyzing wear behaviour of silicon nitride. *Journal of Applied Research and Technology*. 2017; 15(6):624-32.

179. ISO 14243-1 2009. Implants for surgery -- Wear of total knee-joint prostheses -- Part 1: Loading and displacement parameters for wear-testing machines with load control and corresponding environmental conditions for test. 2009.

180. Shi H. Interactions between Inflammatory Cells and CoCrMo Alloy Surfaces under Simulated Inflammatory Conditions: ProQuest Dissertations Publishing; 2016.

181. Fini M, Pagani S, Giavaresi G, et al. Functional Tissue Engineering in Articular Cartilage Repair: Is There a Role for Electromagnetic Biophysical Stimulation? *Tissue Engineering Part B: Reviews*. 2013; 19(4):353-67.

182. Lee Y, Choi J, Hwang NS. Regulation of lubricin for functional cartilage tissue regeneration: a review. *Biomaterials research*. 2018; 22(1):9-10.

183. More NS, Diomidis N, Paul SN, Roy M, Mischler S. Tribocorrosion behavior of β titanium alloys in physiological solutions containing synovial components. *Materials Science & Engineering C*. 2011; 31(2):400-8.

184. Riaz M, Caputo M, Ferraro M, Ryu J. Influence of Process-Induced Anisotropy and Synovial Environment on Wear of EBM Built Ti6Al4V Joint Implants. *J of Materi Eng and Perform*. 2018; 27(7):3460-71.

185. Serro AP, Gispert MP, Martins MCL, Brogueira P, Colaço R, Saramago B. Adsorption of albumin on prosthetic materials: Implication for tribological behavior. *Journal of Biomedical Materials Research Part A*. 2006; 78A(3):581-9.

186. Hua Z, Gu P, Zhang J. Tribological and electrochemical studies on biomimetic synovial fluids
. *Science China Technological Studies*. 2010; 53(11):2996-3001.

187. Park J, Duong C, Chang H, et al. Role of hyaluronic acid and phospholipid in the lubrication of a cobalt–chromium head for total hip arthroplasty. *Biointerphases*. 2014; 9(3):031007.

188. Milošev I, Hmeljak J, Cör A. Hyaluronic acid stimulates the formation of calcium phosphate on CoCrMo alloy in simulated physiological solution. *J Mater Sci: Mater Med*. 2013; 24(3):555-71.

189. Markus A Wimmer, Alfons Fischer, Robin Büscher, et al. Wear mechanisms in metal-on-metal bearings: The importance of tribochemical reaction layers. *Journal of orthopaedic research : official publication of the Orthopaedic Research Society*. 2010; 28(4):436-43.

190. Ng Chin Fei, Nik Mizamzul Mehat, Shahrul Kamaruddin. Practical Applications of Taguchi Method for Optimization of Processing Parameters for Plastic Injection Moulding: A Retrospective Review. *ISRN Industrial Engineering*. 2013; 2013:1-11.

191. Tekade RK, Chougule MB. Formulation development and evaluation of hybrid nanocarrier for cancer therapy: Taguchi orthogonal array based design. *BioMed Res Int*. 2013; 2013.

192. Morsi H, Yong KL, Jewell AP. Evaluation of the Taguchi methods for the simultaneous assessment of the effects of multiple variables in the tumour microenvironment. *International seminars in surgical oncology : ISSO*. 2004; 1(1):7.

193. Lu S, Buchanan FJ, Orr JF. Analysis of variables influencing the accelerated ageing behaviour of ultra-high molecular weight polyethylene (UHMWPE). *Polymer Testing*. 2002; 21(6):623-31.

194. Kallel H, Zaïri H, Rourou S, et al. Use of Taguchi's methods as a basis to optimize hybridoma cell line growth and antibody production in a spinner flask. *Cytotechnology*. 2002; 39(1):9-14.

195. McCord JM. Free radicals and inflammation: Protection of synovial fluid by superoxide dismutase. *Science*. 1974; 185(4150):529-31.

196. Grootveld M, Henderson EB, Farrell A, Blake DR, Parkes HG, Haycock P. Oxidative damage to hyaluronate and glucose in synovial fluid during exercise of the inflamed rheumatoid joint. Detection of abnormal low-molecular-mass metabolites by proton-n.m.r. spectroscopy. *Biochem J*. 1991; 273(2):459-67.

197. Frankel GS. Pitting corrosion of metals: A review of the critical factors. *J Electrochem Soc*. 1998; 145(6):2186-98.

198. Schmalzried TP, Jasty M, Harris WH. Periprosthetic bone loss in total hip arthroplasty. Polyethylene wear debris and the concept of the effective joint space. *J BONE JT SURG SER A*. 1992; 74(6):849-63.

199. Liou G-, Storz P. Reactive oxygen species in cancer. *Free Radic Res*. 2010; 44(5):479-96.

200. Zhou R, Yazdi AS, Menu P, Tschopp J. A role for mitochondria in NLRP3 inflammasome activation. *Nature*. 2011; 469(7329):221-6.

201. Clancy RM, Amin AR, Abramson SB. The role of nitric oxide in inflammation and immunity. *Arthritis Rheum*. 1998; 41(7):1141-51.

202. Geetha M, Singh AK, Asokamani R, Gogia AK. Ti based biomaterials, the ultimate choice for orthopaedic implants - A review. *Prog Mater Sci*. 2009; 54(3):397-425.

203. Kurtz S, Ong K, Lau E, Mowat F, Halpern M. Projections of primary and revision hip and knee arthroplasty in the United States from 2005 to 2030. *J Bone Jt Surg Ser A*. 2007; 89(4):780-5.

204. Li X, Zhang G, Ma H, Zhang D, Li J, Zhu D. 4,5-Dimethylthio-4'-[2-(9-anthryloxy)ethylthio]tetrathiafulvalene, a highly selective and sensitive chemiluminescence probe for singlet oxygen. *J Am Chem Soc*. 2004; 126(37):11543-8.

205. Gilbert, Jeremy L. Life on the Metal's Edge: The interactions between metallic biomaterials and the living system. *Stevenson Biomaterials Lecture Series at Syracuse University*. March 4, 2016.

Appendix A: Presentation figure adaptation

A.1.

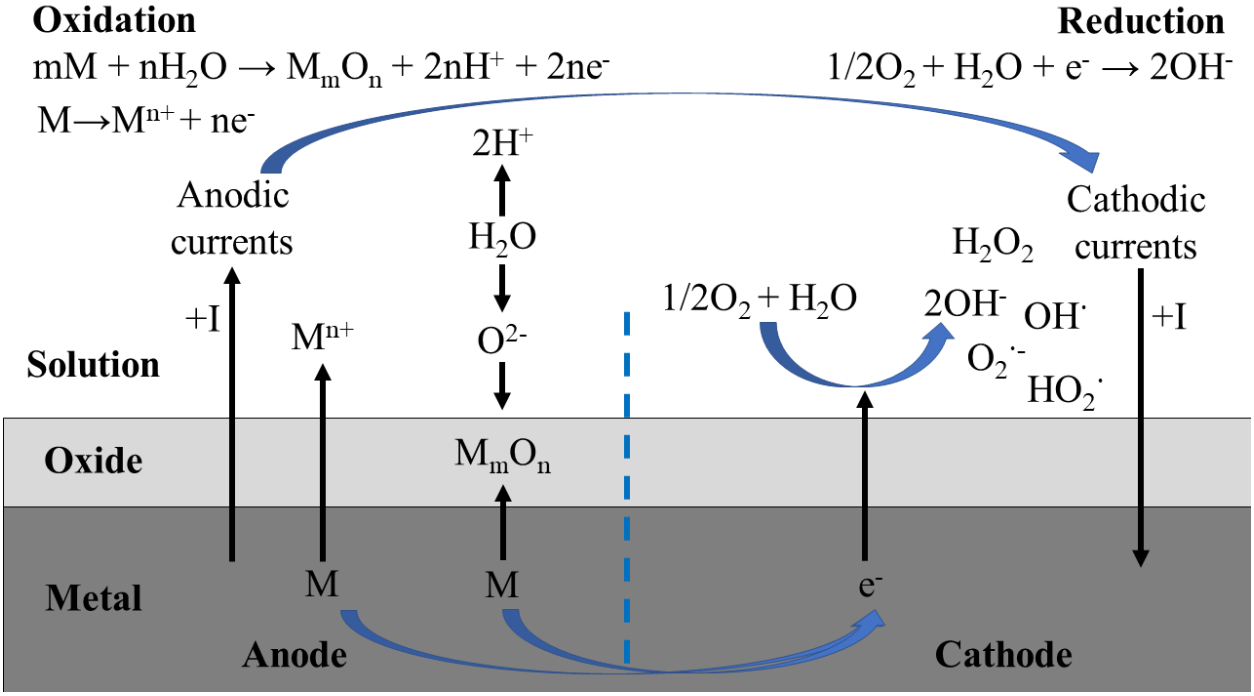

Reduction reactions leading to ROS production via dissolution of the oxide film and interactions involving surface electrons and local water and oxygen molecules [Adapted from Gilbert, 2016][205]

Appendix B: Fluorescent probe techniques

B.1. Pentafluorobenzenesulfonyl fluorescein synthesis

[Adapted from Maeda et al. 2004, *Angew. Chem. Int. Ed.*, doi: 10.1002/anie.200452381]

1. Mix fluorescein (acid free) (1.0 g, 3.0 mmol) and pentafluorobenzenesulfonyl chloride (1.1 eq) in 5 mL 2, 6-lutidine, 20 mL dichloromethane overnight at room temperature
2. Dilute with dichloromethane to 200 mL
3. Wash twice with 1M HCl (200 mL)
4. Wash once with brine (200 mL)
5. Dry yellow-amber solid over $MgSO_4$ to remove solvent via evaporation
6. Purify with silica gel chromatography eluted with dichloromethane-acetone (20:1)
7. Confirm with mass spectroscopy, $C_{26}H_{12}F_5O_7S$ M_W (g/mol): 563.0224
8. Store in dry location

B.2. Standard curve serial dilution and calibration

1. Dissolve final product (HTA, fluorescein) in appropriate solvent (DI, 0.9% NaCl, 1X PBS, EtOH + 1X PBS, etc.) at a known concentration
2. Serially dilute mixture by adding equal parts volume of the original concentration to new pure solvent
3. Dilute down using Step 2 until lower concentration limit of expected product obtained
4. Measure fluorescent intensity of each concentration (n = 3) using black 96-well plates with clear bottoms to remove incidental fluorescence at the appropriate excitation and emission wavelengths [HTA (λ_{ex} = 315 nm, λ_{em} = 425 nm), fluorescein (λ_{ex} = 485 nm, λ_{em} = 530 nm)]

5. Plot fluorescent intensity ratio (I/I_O) against known concentrations and obtain regression line with Excel
6. Use regression equation to calculate unknown concentrations during electrochemical experiments

Appendix C: Nearfield electrochemical impedance spectroscopy (NEIS) protocol

C.1. Experimental set-up

1. Puncture a 1 mL (1.5 mL capacity) pipette tip using a syringe needle about half-way up through both sides
2. Prepare chlorided silver-chloride wire by applying flame to the wire to burn off any residue, submerge in bleach for at least 1 hour

   For flat surfaces:
3. Feed the platinum wire counter electrode and chlorided silver-chloride wire reference electrode through opposite puncture holes (wires cannot touch)
4. Fill pipette with ionic solution of choice
5. Cover top with Parafilm to create partial vacuum seal
6. Hold pipette in place using a ring-stand clamp, lower to surface and apply a press-fit and remove any residual solvent from the surface using a Kimwipe
7. Attach potentiostat leads to working, counter and reference electrodes

   For curved surfaces:
8. Fill bottom of pipette tip with PBS soaked agar gel (Note: this will create an ionic bridge between the surface and solution without any leakage due to the curved nature of the surface)
9. Repeat Steps 3-7